Department of Physics
University of Strathclyde

Characterisation of a Point-Source Integrating Cavity Absorption Meter for applications in optical oceanography

Katharina Lefering

2016

A thesis submitted in accordance with the requirements for the degree

Doctor of Philosophy

Declaration of Authenticity and Author's Rights

This thesis is the result of the author's original research. It has been composed by the author and has not been previously submitted for examination which has led to the award of a degree.

Signed:

Date:

Abstract

Many biogeochemical and physical processes in the aquatic environment are driven by the spectral light absorption properties of the water body and the constituents dissolved and suspended within. Improving our knowledge on absorption processes in marine waters is of great interest to optical oceanographers as absorption influences the structure of underwater light fields. The determination of high quality absorption data are important for accurate modelling of underwater radiative transfer processes and the interpretation and derivation of ocean colour remote sensing products. Accurate measurements of spectral absorption coefficients, however, are challenging because instruments and methods are affected by scattering by marine particles and can suffer from significant systematic errors. Röttgers and co-workers (2005) introduced a point-source integrating cavity absorption meter (PSICAM) in which sample absorption is measured inside an integrating sphere using a totally diffuse light field. This set-up has been shown to be insensitive to scattering errors and therefore ideally suited for absorption determinations of marine waters.

Initial characterisation and a sensitivity analysis confirmed the superior performance of the PSICAM compared to other spectrophotometric techniques but also highlighted remaining limitations in accuracy at UV/blue wavelengths. PSICAM data were subsequently used to develop and validate corrections for established absorption measurements, in particular the determination of particulate absorption coefficients with the filter pad technique and the determination of *in situ* absorption measurements with submersible AC-9 instruments. The latter can be used to populate radiative transfer models and simulate underwater light fields. An optical closure study demonstrated consistency between *in situ* measurements of radiometry and inherent optical properties coupled into radiative transfer model outputs, confirming high accuracy of input absorption data and output model parameters. The ability to model underwater and water-leaving light fields correctly is important for ecosystem modelling application and the validation of satellite remote sensing data.

A preliminary analysis of the potential to simultaneously measure spectral fluorescence and absorption was carried out. This demonstrated both the magnitude of inelastic scattering effects on current PSICAM performance and potential towards further development of the system that could benefit primary production studies.

Acknowledgements

I would firstly like to express my gratitude to my supervisor, David McKee, for his infinite support, honest advice (regarding our work and life in general). Thank you for your humour and enthusiasm and always being able to motivate me and for your patient guidance in the countless conversations we had over the past years.

I would like to say thank you to Professor Alex Cunningham, for his opinions and, of course, for Friday cake. Thank you also to Rüdiger Röttgers who never got tired of sharing his experience with me, always reminding me that there is still a lot more to learn. This project has benefited greatly from our discussions.

I must say a very special thank you to my dear friend and colleague, Catherine Mitchell, who made me feel very welcome in Glasgow, even long after she had left the group/country.
I'd like to thank my fellow PhD student Jacopo, for his support and friendship throughout all stages of my PhD. I would like to acknowledge the work of everyone contributing to data collection and the success of this project: Rebecca Weeks, Fethi Bengil and Anna Gribbon.

Also, thanks to the Marine Alliance for Science and Technology in Scotland (MASTS), not only for funding my studies but also for the great support I've experienced through the MASTS community and for all the encouraging discussions I had on the annual Grad School retreat.

I would like to thank my friends back in Germany for bearing with me and my friends in Glasgow for the many cheerful hours helping me to switch off from work on evenings and weekends. Thanks also to my flatmates, Cinta and Joana, for giving me a home and a platform for countless complaints about work and the weather in Glasgow. A special thanks to Jochen, for introducing me to the great outdoors and for being there from the start to the very end. And thank you, Theo, for filling the last months with so much more than sunshine and coffee.

Finally, I would like to thank my parents for giving me the opportunity to do a PhD and have all these wonderful experiences. I am deeply grateful for your love and couldn't have done it without your support from the distance.

Table of content

Publications

LEFERING, I., BENGIL, F., TREES, C., RÖTTGERS, R., BOWERS, D., NIMMO-SMITH, A., SCHWARZ, J. & MCKEE, D. 2016. Optical closure in marine waters from *in situ* inherent optical property measurements. *Optics Express,* 24(13)**,** 14036 - 14052.

LEFERING, I., RÖTTGERS, R., WEEKS, R., CONNOR, D., UTSCHIG, C., HEYMANN, K. & MCKEE, D. 2016. Improved determination of particulate absorption from combined filter pad and PSICAM measurements. *Optics Express,* 24(22), 24805-24823.

1. Introduction

1.1. Marine Optics background

The sun provides energy to the oceans through visible and infrared radiation. Water is nearly opaque, i.e. absorbs strongly, in the infrared spectral region and therefore plays a key role in global solar heating. Visible radiation is also an important source of energy for the marine environment, driving photosynthesis and primary production, the basis for the marine food web. Sunlight which has passed through the atmosphere is either reflected at the sea surface or penetrates the water where it is either absorbed or scattered by its constituents.

Absorption and scattering are properties of water and the constituents dissolved and suspended within. They are independent from the angular structure of the incident light field. These so-called inherent optical properties, IOPs, (Preisendorfer, 1961) can provide information about organic and inorganic constituents in the water (e.g. Chang and Dickey, 1999). Constituent concentration and composition determine how light travels through a water body. This process is described by radiative transfer (RT) theory which links the optical properties of the water body to the angular structure and spectral distribution of underwater and water-leaving light fields. Accurate knowledge of IOPs is therefore required for the parameterisation of RT simulations to model these light fields (Mobley, 1994).

Understanding RT processes occurring in the ocean is of great interest to optical oceanographers, not only to provide accurate models of the light available underwater but also for solving the inverse problem: retrieving information on absorption and backscattering and thereby of constituent composition and concentrations from satellite remote sensing signals. Satellite remote sensing allows monitoring and mapping of the marine environment on large temporal and spatial scales. IOPs directly influence satellite remote sensing signals (Eq. 1.1) and accurate measurements of IOPs are required for the interpretation of ocean colour satellite data (Lee *et al.*, 2002, Wozniak and Stramski, 2004). For example, Morel and Prieur (1977) identified a simplified relationship between the spectral backscattering coefficient, $b_b(\lambda)$, the spectral absorption coefficient, $a(\lambda)$, and the reflectance, $R(\lambda,z)$, that can be sensed from a satellite

$$R(\lambda,0^-) \propto \frac{b_b(\lambda)}{a(\lambda)} \qquad [-] \quad [1.1]$$

where λ [nm], is the wavelength and z=0 denotes the depth just below the sea surface.

IOPs and absorption in particular, are also important for our understanding of many biological, geochemical and physical processes in the marine environment. For example, absorption has an impact on primary production because it determines (1) how much light is available for harvesting by algae and (2) how much light can be provided to the photosynthetic process, i.e. is absorbed by the algae themselves. Many bio-optical and coupled food web models therefore require absorption coefficients as input parameter (e.g. Prieur and Sathyendranath, 1981, Gordon, 1992). Other processes which can be linked to the absorption properties of marine waters and are relevant to the global climate include solar heating (Lewis *et al.*, 1990) and the amount of carbon dissolved in water (Coble, 2007). It is clear, therefore, that accurate determination of spectral absorption data are essential for correct interpretation and advanced understanding of the optical properties of the marine ecosystem and thus will ultimately influence our ability to monitor and predict long-term changes in Earth's climate. Although routinely used, many absorption measurement techniques suffer from systematic errors (Section 1.5) typically originating from scattering processes adversely affecting measurements. It is therefore necessary to identify and reduce uncertainties associated with different absorption measurements which find application in marine studies.

1.2. Optical theory

This section will introduce fundamental optical processes occurring in the aquatic environment and give a description of basic absorption measurement techniques, their benefits and disadvantages.

1.2.1. Inherent optical properties - IOPs

Here a short summary on different inherent optical properties and their relationships is provided. A more detailed review on different IOPs and their derivation can be found in Mobley (1994).

When a beam of light passes through a volume of a turbid medium with a thickness, Δr, some of its energy will be absorbed, some will be scattered out of its path and some will be transmitted through the volume. The spectral absorption coefficient, $a(\lambda)$, at any given wavelength, λ, is defined as the fraction of incident radiant power, $I_0(\lambda)$, that is absorbed, $I_A(\lambda)$, per unit distance.

$$a(\lambda) = \lim_{\Delta r \to 0} \frac{I_A(\lambda)/I_0(\lambda)}{\Delta r} \qquad [m^{-1}] \qquad [1.2]$$

The spectral scattering coefficient, $b(\lambda)$, is similarly defined as the fraction of incident power scattered, $I_B(\lambda)$, (without regard to its angular distribution) per unit distance.

$$b(\lambda) = \lim_{\Delta r \to 0} \frac{I_B(\lambda)/I_0(\lambda)}{\Delta r} \qquad [m^{-1}] \qquad [1.3]$$

The total scattering coefficient can be separated into light scattered in forward directions (Ψ = 0° - 90°), $b_f(\lambda)$, and light scattered in backward directions (Ψ = 90° - 180°), $b_b(\lambda)$.

$$b(\lambda) = b_f(\lambda) + b_b(\lambda) \qquad [m^{-1}] \qquad [1.4]$$

The angular distribution of the incident power scattered is described by the spectral volume scattering function (VSF), $\beta(\Psi,\lambda)$, which is the fraction of incident light scattered at an angle, ψ, per unit solid angle, $\Delta\Omega$.

$$\beta(\psi,\lambda) = \lim_{\Delta r \to 0} \lim_{\Delta\Omega \to 0} \frac{I_B(\psi,\lambda)/I_0(\lambda)}{\Delta r \Delta\Omega} \qquad [m^{-1}\ sr^{-1}] \qquad [1.5]$$

Integrating the VSF over all directions (solid angles), returns the total power of scattered light per unit incident irradiance per unit volume, i.e. the scattering coefficient, b. Similarly, integrating the VSF over all angles in the backward direction returns the spectral backscattering coefficient, $b_b(\lambda)$.

$$b_b(\lambda) = 2\pi \int_{\psi=\pi/2}^{\pi} \beta(\psi,\lambda)\ \sin\psi\ d\psi \qquad [m^{-1}] \qquad [1.6]$$

Finally, the spectral beam attenuation coefficient, $c(\lambda)$, is the sum of the absorption coefficient and scattering coefficients.

$$c(\lambda) = a(\lambda) + b(\lambda) \qquad [m^{-1}] \qquad [1.7]$$

1.2.2. Radiometry

RT theory describes how the composition of a medium determines the structure of the light field within this medium. The fundamental quantity to describe underwater light fields is the spectral radiance, $L(\lambda)$, defined as the amount of radiant energy, Q [W], per unit area, A [m^2], per unit solid angle, Ω [sr].

$$L(\lambda, z, \theta, \phi) = \frac{dQ}{dA d\Omega d\lambda} \qquad [W\,m^{-2}\,sr^{-1}\,nm^{-1}] \qquad [1.8]$$

for a depth, z [m], a zenith angle, θ [rad], and the azimuthal angle, Φ [rad], of the incoming light. All other radiometric quantities can be derived from $L(\lambda)$.

The spectral irradiance, $E(\lambda)$, however, is more routinely used because complete angularly resolved measurements of $L(\lambda)$ are more difficult to conduct and not necessarily required for the majority of applications. Typically, two types of $E(\lambda)$ are of interest: the downwelling planar irradiance, $E_d(\lambda)$ (Eq. 1.9), and the upwelling planar irradiance, $E_u(\lambda)$ (Eq. 1.10), distinguishing between all light traveling in the general downwards direction (θ = 0 - $\pi/2$) and general upwards direction (θ = $\pi/2$ - π) respectively, per unit area.

$$E_d(\lambda, z) = \int_{\phi=0}^{2\pi} \int_{\theta=0}^{\pi/2} L(\lambda, z, \theta, \phi) \cos\theta \sin\theta \, d\theta d\phi \qquad [W\,m^{-2}\,nm^{-1}] \qquad [1.9]$$

$$E_u(\lambda, z) = \int_{\phi=0}^{2\pi} \int_{\theta=\pi/2}^{\pi} L(\lambda, z, \theta, \phi) \cos\theta \sin\theta \, d\theta d\phi \qquad [W\,m^{-2}\,nm^{-1}] \qquad [1.10]$$

1.3. The absorption process

Absorption of light is the physical process during which the energy of an incoming photon is transferred to a molecule and the photon is annihilated. Every molecule has a series of discrete energy levels, each corresponding to a certain rotational, vibrational and electronic state. When a photon is absorbed, its energy is stored within the molecule by elevation of one of the molecule's electrons from (typically) the ground state to an excited state (Fig. 1.1). This energy transition corresponds to the energy, and thus the wavelength, of the absorbed photon. Photons absorbed in the visible spectrum will result in energy transitions on the electronic level. Photons with a longer wavelength (> 20μm) will result in intermediate to small energy changes and transitions in vibrational or rotational energy states, respectively.

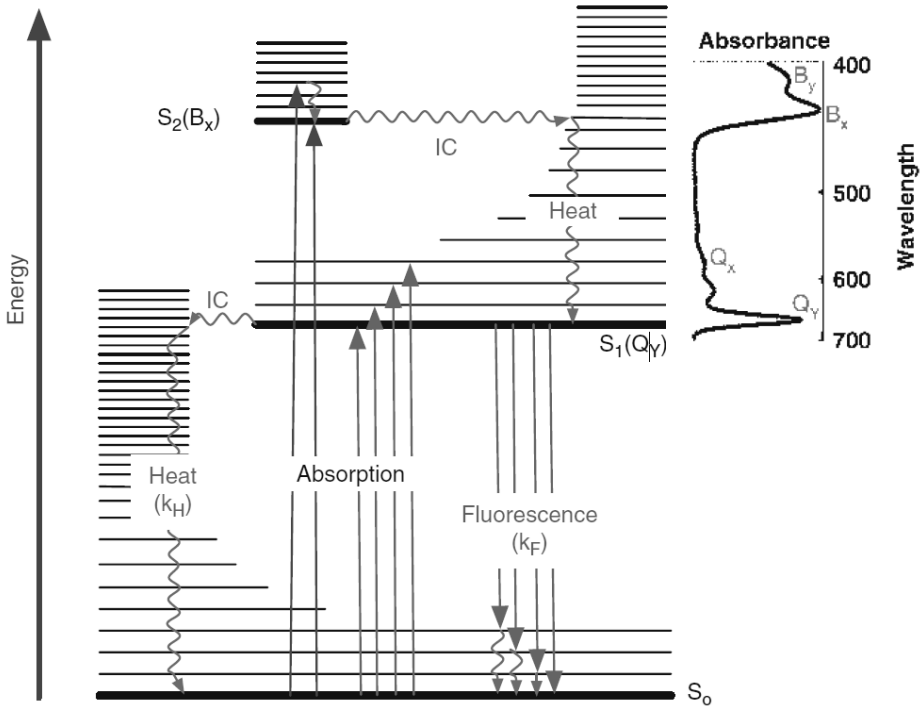

Fig. 1.1 Energy level diagram of a molecule showing the absorption of photons and subsequent electron transition to different energy levels. Electrons which are excited to the second excited state ($S_2(B_x)$) undergo a series of radiationless (heat) downward transitions until they reach the excited singlet state ($S_1(Q_y)$). From this excited singlet state the electron drops back to the ground state by emitting a photon. An alternative pathway to release excess energy is through non-radiative decay as illustrated on the left. The absorbance spectrum on the right shows the absorption peaks corresponding to the two electronic levels (Huot and Babin, 2010).

The vibrational/rotational levels are sub-levels of the electronic energy levels. In complex molecules, such as chlorophylls and other photosynthetic pigments, two separate electronic levels can overlap because their vibrational/rotational levels contain the same amount of energy. For example, the lowest vibrational/rotational level of the higher electronic state can have the same amount of energy as the highest vibrational/rotational level of the lower electronic state. In these pigments more than one electronic transition can occur, exciting the electron from one of the many rotational/vibrational levels of the ground state to any of the rotational/vibrational levels in the electronic energy level 2. Chlorophyll, for example, has two main absorption bands, one in the blue corresponding to a transition to a higher electronic state and one in the red leading to a smaller energy transition to a lower electronic level. When chlorophyll absorbs a blue photon a series of rapid downward transitions through the vibrational/rotational levels occurs until the lower electronic state, the excited singlet state, is reached. It is the energy contained in this excited singlet state that is used for photosynthesis. Hence, all visible photons absorbed by the molecule trigger the same amount of photosynthetic activity because they all provide an equivalent amount of energy to the photosynthetic process. Molecules that absorb light but are not involved in the photosynthetic process can dissipate the up-taken energy via either non-radiative decay (heat) or in form on re-emission of radiation (fluorescence, see Chapter 6). The efficiency of this radiative process is described by the fluorescence quantum yield, i.e. the number of photons emitted as fluorescence per number of photons absorbed.

1.4. Light-absorbing components in the marine environment

The total absorption spectrum of a natural water sample is defined as the sum of the spectral absorption coefficients of all light-absorbing components, i.e. water itself plus all organic and inorganic constituents dissolved or suspended within

$$a_{total}(\lambda) = a_{seawater}(\lambda) + a_{CDOM}(\lambda) + a_{phytoplankton}(\lambda) + a_{NAP}(\lambda) \qquad [m^{-1}] \qquad [1.11]$$

where a_{total} is the total absorption coefficient, $a_{seawater}$ is the absorption coefficient of water at a given temperature and salinity and a_{CDOM} , $a_{phytoplankton}$ and a_{NAP} are the absorption coefficients of coloured dissolved organic matter (CDOM), phytoplankton (extractable algal pigments) and non-algal particles (NAP; residual particulate absorption after extraction of algal pigments), respectively. The following sections will introduce the absorption

properties, typical ranges and spectral shapes of these different components which determine the IOPs of natural water and hence affect the propagation of light underwater.

1.4.1. Absorption by seawater

Pure water is a blue liquid, absorbing very weakly in the blue and green region of the visible spectrum and strongly in the red and NIR (Fig. 1.2). The absorption spectrum shows visible shoulders corresponding to harmonics associated with state transitions in the O-H bonds. Accurate knowledge of spectral seawater absorption coefficients is extremely important, particularly in very clear oceanic waters. Smith and Baker (1981) derived spectral absorption coefficients for the 'clearest' natural waters (e.g. Sargasso Sea) based on measurements of the diffuse attenuation coefficients and laboratory-based measurements. Their estimates at wavelengths > 500 nm were later found to compare well with the first measurements of purified water absorption coefficients determined by Buiteveld *et al.* (1994) who used a submersible absorption meter (Hakvoort *et al.*, 1994). Observed increased variability in UV/blue pure water absorption coefficients is caused by a combination of different factors: limited sensitivity of photodiode detectors and low lamp output at these wavelengths and high sensitivity to contamination. The increased absorption at UV/blue wavelengths observed by Smith and Baker (1981) is presumably due to absorption by salt ions present in sea water compared to later studies performed on purified water. More reliable and highly accurate measurements have been made using an integrating cavity absorption meter (ICAM) by Pope and Fry (1997) who determined absorption coefficients for pure water from 380-700 nm. Recent measurements of pure water absorption used an improved ICAM set-up for a more accurate determination of absorption coefficients in the UV/short VIS spectral region, down to 250 nm (Lu, 2006, Wang, 2008). The final absorption coefficients for pure water used for this work were composed from empirical determinations by Wang (2008) from 350 – 400 nm, Pope and Fry (1997) from 400-700 nm and Smith and Baker (1981) from 700 – 800 nm (following suggestions in Wozniak and Dera (2007) and the review conducted in the framework of the ESA-STSE *WaterRadiance* project (Röttgers *et al.*, 2009)).

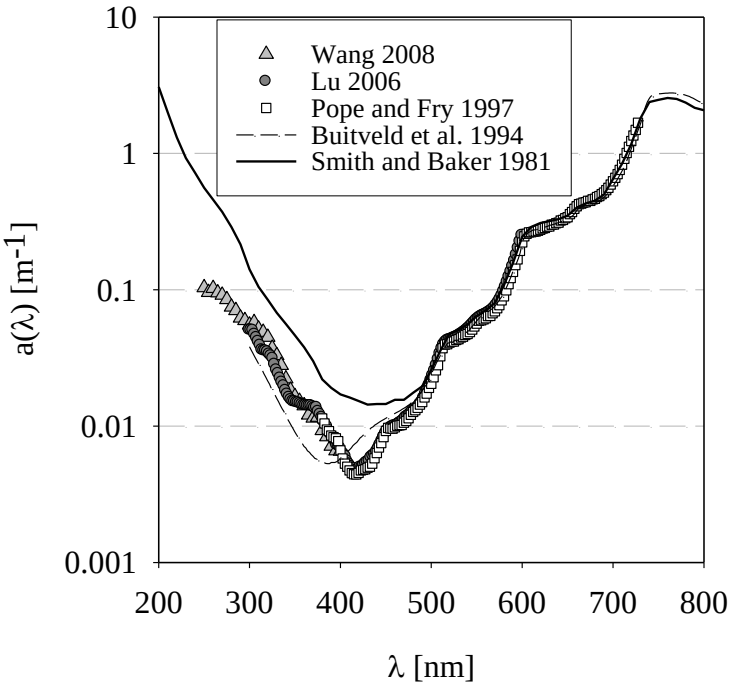

Fig. 1.2 Selection of published pure water absorption coefficients from UV to NIR wavelengths. Absorption coefficients are plotted on a log-scale.

1.4.2. Temperature and salinity dependence of water absorption

The absorption of seawater is known to be temperature and salinity dependent. Light absorption by water in the VIS/IR is dependent on the vibrational/rotational energy states of the O-H bonds in the water molecule. The water temperature determines the wavelength and intensity of the three main vibrational/rotational maxima. An increase in temperature (relative to a 20°C reference temperature) results in positive temperature coefficients at wavelength shorter than the maximum and negative temperature coefficients for wavelengths longer than the maximum (Collins, 1925). The presence of salt ions also affects the frequency of intermolecular vibrations and thus leads to changes in the absorption spectrum.

As a result, temperature and salinity differences have to be taken into account and corrected for when pure water is used as a reference, even if the absolute water absorption coefficient does not have to be known exactly in these cases. A range of studies have investigated the spectral temperature (Fig. 1.3) and salinity (Fig. 1.4) dependence of seawater absorption and determined required correction coefficients (Collins, 1925, Pegau and Zaneveld, 1993,

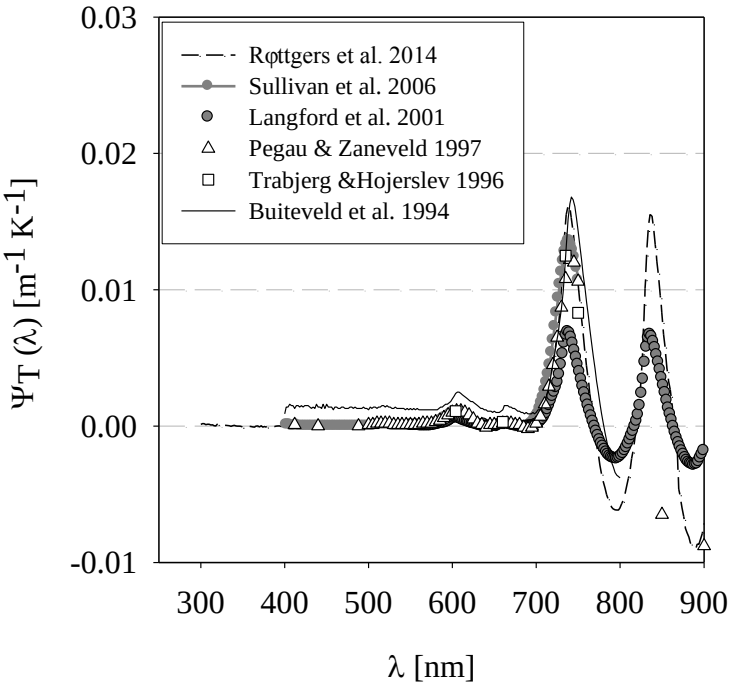

Fig. 1.3 Published temperature correction coefficients, Ψ_T, for the absorption by pure water.

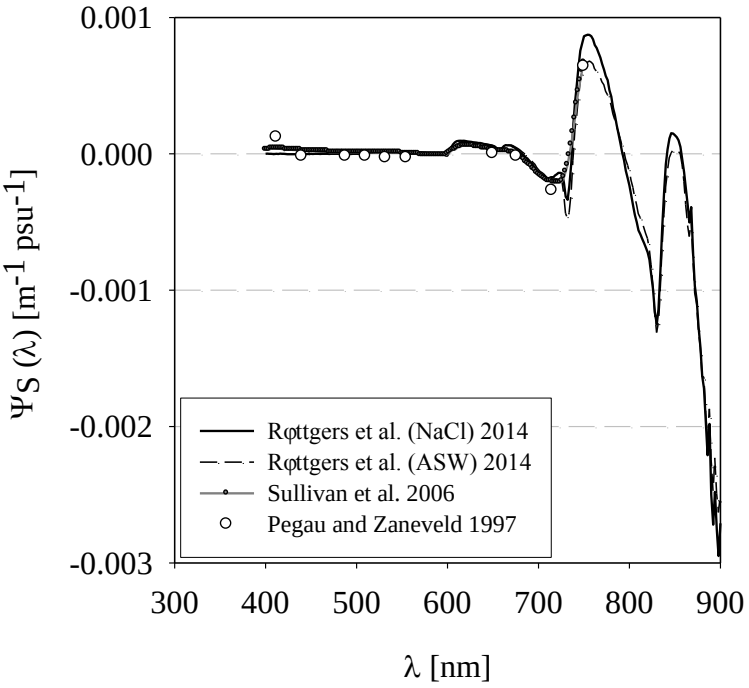

Fig. 1.4 Published salinity correction coefficients, Ψ_S, for the absorption by pure water.

Trabjerg and Hojerslev, 1996, Langford *et al.*, 2001). More recently, correction coefficients have been measured and established for specific instrumentation at VIS and NIR wavelengths, e.g. submersible sensors (Pegau *et al.*, 1997, Sullivan *et al.*, 2006) and integrating cavity approaches (Röttgers and Doerffer, 2007, Röttgers *et al.*, 2014b). Changes in the spectral absorption with temperature have been shown to be linear between 6 and 80 °C (Trabjerg and Hojerslev, 1996, Langford *et al.*, 2001, Segtnan *et al.*, 2001, Sullivan *et al.*, 2006). However, deviations from this linearity might occur at temperatures below 5 °C (Raichlin *et al.*, 2004). The salinity dependence of light absorption by seawater was found to be independent from temperature (Pegau *et al.*, 1997, Sullivan *et al.*, 2006). The scattering properties of seawater also change with salt concentration and temperature as described by Zhang and co-workers (Zhang and Hu, 2009, Zhang *et al.*, 2009a, Zhang *et al.*, 2009b, Zhang and Hu, 2010), which potentially affects the spectrophotometric determination of salinity correction coefficients.

The spectral absorption of a water sample can be corrected for temperature and salinity effects using

$$a_{corrected}(\lambda,T,S) = a(\lambda,T,S) + (T - T_0)\,\Psi_T(\lambda) + (S - S_0)\,\Psi_S(\lambda) \qquad [m^{-1}] \qquad [1.12]$$

where $a_{corrected}$ is the corrected absorption coefficient at a wavelength λ [nm], a temperature T [°C] and a salinity S [psu]. a is the uncorrected absorption coefficient, T_0 and S_0 are the temperature and salinity of the reference – either at which literature values have been determined or of the reference (in case of spectrophotometric measurements), and Ψ_T [m^{-1} K^{-1}] and Ψ_S [m^{-1} psu^{-1}] are the temperature and salinity correction coefficients. For this work, instrument-specific coefficients were derived for the PSICAM and liquid waveguide capillary cell (LWCC) systems. Correction coefficients by Pope and Fry (1997) were used for AC-9 measurements and RT applications.

1.4.3. Absorption by dissolved matter

Coloured dissolved organic matter (CDOM) exhibits a yellow/brown colour and is generated when plant or other organic components decompose. It is a mixture of various large organic molecules, mainly humic and fulvic acids, which are defined operationally as all material that passes through a 0.2 µm pore size filter. It should be noted that this includes truly dissolved, colloidal and very small particulate matter. However, the contribution of scattering by very small particles (< 0.2 µm) has only recently been investigated (Dall'Olmo

et al., 2009, Zhang and Gray, 2015) and scattering by CDOM is still widely considered insignificant. Hence, its spectral absorption is predominantly of interest in optical studies of marine waters (e.g. Green and Blough, 1994, Siegel and Michaels, 1996). The concentration of CDOM is highly variable (Miller *et al.*, 2002, Röttgers and Doerffer, 2007) and typically highest in fresh water systems and rivers and decreasing with distance from shore (D'Sa and Miller, 2003).

CDOM absorption increases exponentially from a low, but not necessarily negligible (Röttgers and Doerffer, 2007), absorption in the red to high absorption in the blue/UV regions and can be described by Eq. 1.13 (Bricaud *et al.*, 1981).

$$a_{CDOM}(\lambda) = a_{CDOM}(\lambda_0) \cdot e^{-S_{CDOM}(\lambda-\lambda_0)} \qquad [m^{-1}] \qquad [1.13]$$

where a_{CDOM} is the absorption by CDOM at wavelength λ and S_{CDOM} is the exponential slope for CDOM with typical values between 0.01 and 0.02. λ_0 is the reference wavelength, typically 440 nm. a_{CDOM}(440 nm) is commonly used to quantify CDOM concentrations and was chosen because 440 nm corresponds roughly to the maximum of the blue phytoplankton absorption peak facilitating easy comparison. The spectral slope, $S_{CDOM,}$ can provide information on the composition of organic matter where CDOM from terrestrial sources has steeper slopes than CDOM of marine origin (Carder et al., 1989).

a_{CDOM} is measured spectrophotometrically against purified water as a reference, using varying pathlengths from 1-10 cm cuvettes in a dual-beam spectrophotometer up to several meters in liquid waveguide systems (e.g. D'Sa *et al.*, 1999). The presence of CDOM influences primary production as it limits the amount of light available for harvesting by marine algae (Carder *et al.*, 1989). Additionally, knowledge of the CDOM absorption of a water body is also relevant for the interpretation of ocean colour remote sensing signals (Carder *et al.*, 1991, Nelson and Siegel, 2013) and biogeochemical studies (e.g. Nelson *et al.*, 2010).

1.4.4. Absorption by phytoplankton

Absorption by phytoplankton depends on pigment composition and the physiological state of the organism and extends across the visible spectrum. The pigment composition and, hence, the spectral shape of absorption coefficients can vary strongly between species and depends on the environmental exposure, such as the light climate they have adapted to. A summary of

spectral absorption characteristics of photosynthetic and accessory pigments can be found in Kirk (1983).

The main group of light-harvesting pigments are chlorophylls with absorption peaks in the blue and the red which can be found in all aquatic algae. Extracted chlorophyll absorption peaks are at approx. 430 nm and 665 nm. *In vivo*, when chlorophyll is bound to proteins, the absorption peaks shift towards longer wavelengths, around 435 nm and 675 nm, respectively. In diatoms and green algae chlorophyll dominates the species specific absorption spectrum which only varies slightly depending on the auxiliary pigments, e.g. Fucoxanthin in diatoms (Stauber and Jeffrey, 1988) and Violaxanthin (Jeffrey, 1968) in green algae. Cyanobacteria, on the other hand, rely more heavily on auxiliary pigments such as the phycobiliproteins, phycoerythrin and phycocyanin, and have therefore very characteristic absorption (and fluorescence) spectra. Auxiliary pigments not only contribute to the light-harvesting process by extending the range of the chlorophyll absorption peaks further into the green, but can also help to protect the photosynthetic apparatus by increasing heat dissipation. The absorption by phytoplankton is further affected by their physiological state because this determines how pigments are distributed within a cell (Bricaud *et al.*, 1995). For example, pigments can be packaged under high light conditions to reduce the absorbing area and thereby the amount of energy taken up in order to minimise cell damage.

1.4.5. Absorption by non-algal particulate material

Non-algal particulate absorption is the absorption by all particulate material that cannot be extracted by either organic solvents or oxidising agents and includes non-photosynthetic bacteria, detrital material and suspended inorganic material. Non-algal particulate absorption is dependent on the solvent, e.g. methanol (Kishino *et al.*, 1985) or acetone, used to extract pigments and organic material. Alternatively, algal and non-algal particulate absorption can be separated using an oxidizing agent to bleach the pigments (Tassan and Ferrari, 1995). Non-algal absorption decreases exponentially with increasing wavelength and is typically most significant near rivers and in benthic boundary layers.

1.5. Absorption measurement concepts

All absorption measurements are based on the same principle, which is comparing the radiant power of light transmitted through a sample, I_S, with the radiant power transmitted

through a reference, I_R. If there were no scattering, the amount of light lost would be solely due to absorption by the sample. The output of spectrophotometric measurements is called optical density, $OD(\lambda)$, which is defined as

$$OD(\lambda) = \log_{10}\left(\frac{I_R}{I_S}\right) \qquad [-] \qquad [1.14]$$

According to the Lambert-Beer Law, the absorption coefficient can be calculated from measurements of the optical density when the pathlength, d [m], of the light beam through the sample, i.e. length of the cuvette or capillary cell, is known using

$$a(\lambda) = \frac{2.303\ OD(\lambda)}{d} \qquad [m^{-1}] \qquad [1.15]$$

In seawater, however, some scattering is always present and spectrophotometric measurements potentially overestimate absorption coefficients because of unaccounted light loss due to scattering. As a result, several methods have been developed and tested to overcome scattering issues and improve the accuracy of absorption determination of natural water samples.

1.5.1. Determination of CDOM absorption

The determination of CDOM absorption in a spectrophotometer equipped with glass cuvettes (Bricaud *et al.*, 1981) is typically less problematic because the amount of scattering has been reduced to a minimal level by filtration of the sample. Some scattering materials, such as small particulate matter and (micro-) bubbles, however, potentially remain in the sample after filtration, which results in measurement uncertainties of unknown magnitude (Zhang and Gray, 2015). Standard bench-top spectrophotometers, such as single-beam or dual-beam spectrophotometers (Fig. 1.5), have a low sensitivity due to a short pathlength (typically a 10 cm cuvette).

CDOM absorption determinations in long-pathlength systems have been shown to be as accurate and more sensitive compared to measurements with standard spectrophotometers (D'Sa *et al.*, 1999, Miller *et al.*, 2002). Total internal reflection at the walls of the liquid waveguide capillary cell (LWCC) returns a portion of the light scattered and thereby reduces, but does not completely eliminate, scattering errors in the absorption determination.

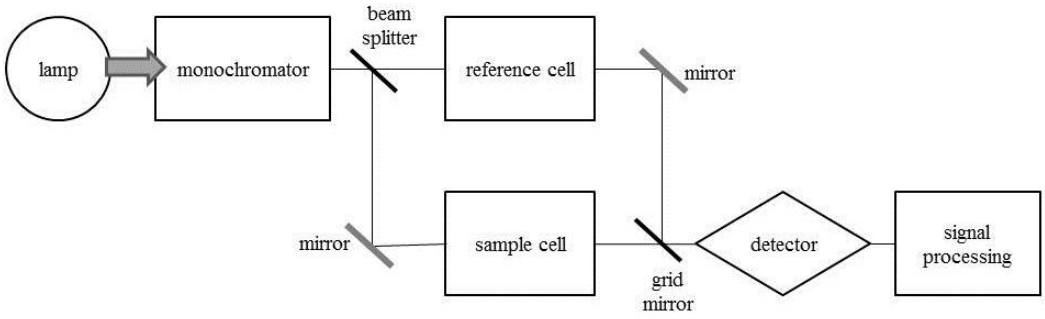

Fig. 1.5 Diagram of a dual-beam spectrophotometer. The amount of light passing through the sample compared to the reference cell provides information on the attenuation by sample constituents. Scanning monochromatic illumination is used to build up a full spectrum.

LWCC systems (Fig. 1.6) have a higher sensitivity due to longer pathlengths (between 50 cm and 5 m) and require only a small sample volume (a few millilitres). LWCC measurements are advantageous over cuvette measurements as they are less sensitive to ship movement than cuvette measurements. The small sample volume, however, can change temperature very quickly which can cause degassing of cold natural samples.

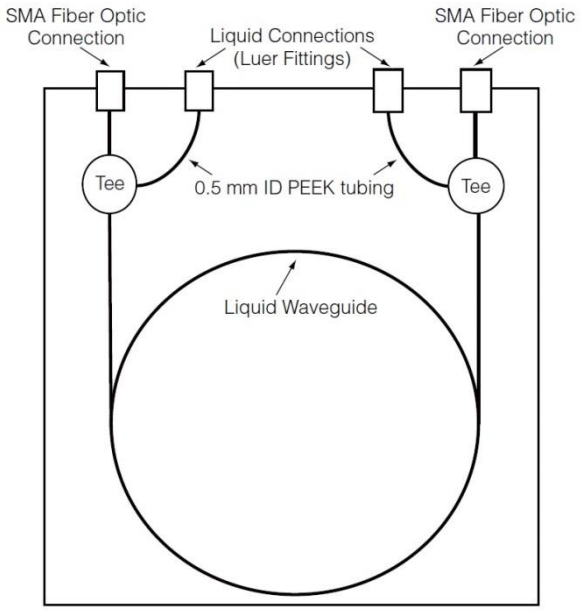

Fig. 1.6 Diagram of a liquid waveguide capillary cell (LWCC). Reference and sample are injected into the cell alternatingly using plastic syringes. Light is passing through the liquids by total internal reflection on the cell walls. The difference between the amount of light passing through a sample compared to a reference can be used to calculate the absorption by sample constituents (World Precision Instruments Inc., 2004).

The presence of (micro-) bubbles in the sample can be a major challenge as bubbles affect the transmission of light through the sample and can lead to an overestimation in optical density (OD). Additionally, air has a higher compressibility relative to water and measurements become more sensitive to pressure changes during sample injection when bubbles are present in the cell. Other sources of uncertainty can originate from unstable fibre connections or contamination of the cell (all very rare; Röttgers, pers. comm.).

1.5.2. Particulate absorption coefficients

Absorption by particulate matter, such as minerals or phytoplankton, has traditionally been measured in bench-top spectrophotometers (Fig. 1.5) by collecting material onto a glass-fibre filter (Yentsch, 1957, Yentsch, 1962). This so-called filter pad technique or quantitative filter technique (QFT; Mitchell, 1990) benefits from having a controllable sensitivity because signal strength can be modified by the amount of material concentrated on the filter paper. The filter pad technique, additionally, allows the partitioning of particulate absorption into absorption by phytoplankton and non-algal particulate matter, removing light absorbing pigments from the filter paper with either an oxidising agent (Ferrari and Tassan, 1999) or an organic solvent (Kishino *et al.*, 1985). Alternatively, particulate spectral absorption coefficients can be partitioned through numerical decomposition (Bricaud and Stramski, 1990, Zheng and Stramski, 2013).

Particulate absorption coefficients can also be determined from measurements of particles in suspension which is challenging due to considerable overestimation of absorption coefficients even for optically thin suspensions due to backscattering and side-scattering losses. Scattering problems can be overcome by using a PSICAM but there are limitations which include difficulties to separate algal and non-algal particulate absorption and lower sensitivity compared to the filter pad technique. Filter pad absorption measurements are therefore expected to be widely used for the determination of particulate absorption coefficients in the foreseeable future (Röttgers and Gehnke, 2012, Stramski *et al.*, 2015). Filter pad measurements, however, need to be corrected for pathlength amplification and scattering offsets of unknown extent (e.g. Bricaud and Stramski, 1990, Roesler, 1998). Over the years, a large number of studies have investigated uncertainties in filter pad measurement and, to date, no consensus has been achieved (detailed review in Chapter 4).

1.5.3. Absorption determination using an integrating cavity

Many RT modelling and remote sensing applications require information on the total absorption by constituents in a water body, i.e. the sum of absorption by all dissolved and suspended matter. Total absorption spectra of an unfiltered sample can be measured with a high accuracy inside an integrating sphere. As a result of multiple reflections at the cavity walls, long pathlengths and high sensitivity are achieved. Scattering effects can be neglected if a homogeneous, diffuse light field is created inside the sphere. Pope and co-workers developed an integrating cavity absorption meter (ICAM) and used it for the determination of pure water absorption coefficients (Pope and Fry, 1997) and natural water sample (Pope *et al.*, 2000). Commercial instruments based on the integrating cavity approach are available (e.g. Trios OSCAR, the HOBI labs a-Sphere and the Turner Designs flow through ICAM). All these instruments were designed as flow through systems, but only a very small number of studies using one of these instruments have been published to date (Peperzak *et al.*, 2015, Peperzak *et al.*, 2011).

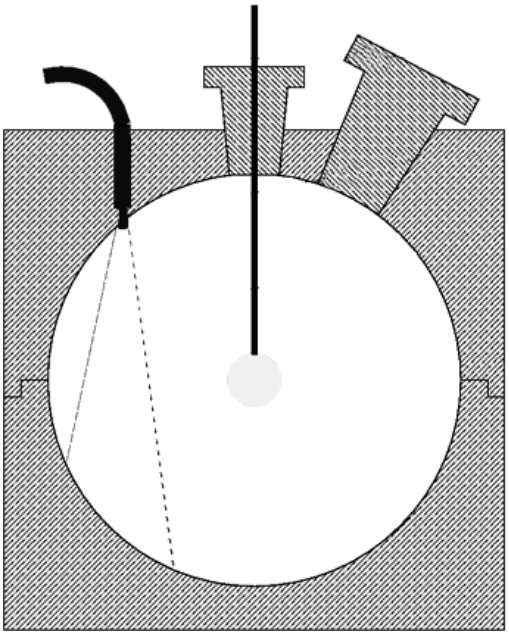

Fig. 1.7 Diagram of the PSICAM set-up: the light source is placed in the centre of the integrating sphere and a fibre optic collects light with a field of view not including the bulb.

Kirk (1997) proposed and theoretically described a point-source integrating-cavity meter (PSICAM; Fig. 1.7) which consists of a spherical cavity illuminated with an isotropic light source placed at the centre of the sphere. This set-up was later implemented and further

investigated by Leathers *et al.* (2000), Lerebourg *et al.* (2002) and Röttgers *et al.* (2005). The accuracy of PSICAM absorption coefficients is determined by the quality of its calibration which requires that the absorption coefficients of the calibration solution are obtained with a different instrument. ICAM configurations typically use broadband, white light illumination and hyperspectral detectors, allowing for very short acquisition times at the expense of potential detector sensitivity issues and internal straylight.

1.5.4. In situ measurements with reflective tube absorption meters

Another approach to measure the total absorption of a water body is to determine absorption coefficients *in situ* using submersible reflective tube absorption meters. The most commonly used instruments for these *in situ* IOP measurements are the WETLabs Inc. AC-9 (9 wavebands; Fig. 1.8) or AC-s (hyperspectral) which allow the simultaneous determination of absorption and attenuation spectra. Over the past two decades, these instruments have become the commercial standard in the field (NASA Protocols - Volume IV; Pegau *et al.*, 2003) and have been widely used in studies investigating the propagation of light underwater (e.g. Chang *et al.*, 2007, Tzortziou *et al.*, 2006) and in ocean colour remote sensing validation activities (e.g. Mitchell *et al.*, 2014).

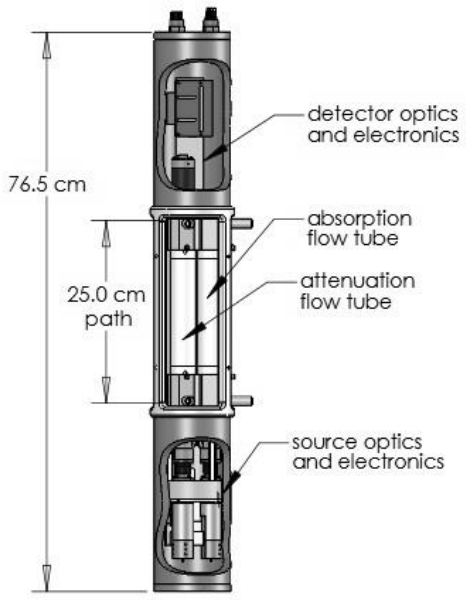

Fig. 1.8 Diagram of an AC-9 submersible attenuation and absorption meter (WETLabs Inc., 2013).

AC-9 absorption measurements use total internal reflection at the external air-glass interface of the cuvette wall to redirects light onto a large area detector and thereby reduce scattering losses (Fig. 1.9). This set-up, however, does not collect all light scattered and measurements still have to be corrected for scattering errors (Zaneveld *et al.*, 1994). Recent efforts to improve AC-9 scattering corrections (Röttgers *et al.*, 2013, McKee *et al.*, 2013) have been developed using PSICAM data for validation.

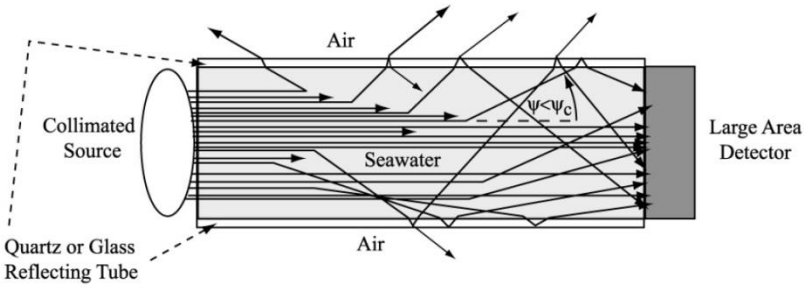

Fig. 1.9 Schematic illustration of light interactions and transmission in a reflective tube absorption meter. Ray paths ending in the water represent absorption, and those extending directly from the source to detector represent beam transmittance. Three scattering interactions are indicated: 1) backward scattered paths do not reach the detector, 2) paths with forward scattering at an angle less than the critical angle experience total internal reflection by the tube and reach the detector over an elongated optical path, and 3) forward scattered ray paths at certain angles experience partial losses (Pegau *et al.*, 2003).

1.6. Aim of Thesis

As discussed above, scattering errors affect different types of absorption methods by varying degrees. Results from PSICAM measurements have been very encouraging with regards to potentially significant improvements in quality of absorption data from natural waters (Röttgers *et al.*, 2007, Röttgers and Doerffer, 2007). The availability of quantitative absorption data from PSICAM measurements allows re-assessment of the performance of commonly used absorption techniques (e.g. McKee *et al.*, 2014, Röttgers *et al.*, 2013). It enables the identification of sources of measurement uncertainties and provides the opportunity to develop empirical corrections for existing methods. Improving the quality of measured absorption data will strengthen our confidence in products derived from satellite remote sensing data and modelling applications populated with absorption coefficients.

This thesis aims to quantify measurement uncertainties in different absorption measurement techniques commonly used in oceanographic sciences. Therefore, the performance of

PSICAM measurements and associated uncertainties, such as sensitivity to calibration procedure and inelastic scattering effects, must first be assessed. Other absorption techniques will then be compared against PSICAM data and sources and magnitude of measurement errors will be analysed. Similarly, the impact of uncertainties in absorption data on RT modelling will be investigated to highlight the importance of accurate determination of absorption coefficients for marine waters.

In particular, the following questions will be addressed:

- How does the PSICAM perform in comparison to other laboratory-based methods? Which parameters are PSICAM absorption determinations most sensitive to? Can any limitations be observed?

- What effect do different corrections for filter pad absorption measurements have on the quality of particulate absorption coefficients? Is there a significant benefit of some geometric configurations over others?

- How accurately can we currently measure and model underwater light fields? How much closer do we get to optical closure using most recent (PSICAM validated) corrections for *in situ* absorption measurements?

- What effect do inelastic scattering effects have on absorption determinations with a PSICAM? What additional information can be gained from developing a scanning, monochromatic PSICAM, e.g. combined spectral absorption and fluorescence data?

2. Methods and Datasets

This chapter will give detailed descriptions of all measurement and sample handling protocols (Section 2.1) used for this work, including measurements with laboratory-based and submersible sensors (Section 2.2 – 2.5). It will further outline the composition of different datasets, consisting of either algal culture (Section 2.7) or field samples (Section 2.8). Field data include absorption as well as accompanying IOP and radiometry data and were acquired on 3 different research cruises between 2009 and 2015 (Section 2.8).

2.1. Sample preparation and handling

The determination of accurate absorption coefficients for natural waters is known to be challenging. In contrast, measurements of coloured solutions are expected to be reasonably straight forward. However, when comparing absorption coefficients measured with a spectrophotometer or LWCC system with PSICAM data, it became apparent that the former two methods suffer from errors due to the presence of scattering even for coloured solutions. These observations do not only raise concerns about the quality of absorption data from natural samples obtained with these techniques but also about absorption coefficients required for the calibration of the PSICAM and as a result, directly influence the accuracy of PSICAM absorption data.

Sample handling, such as preparation of the solutions, filtration and storage, was found to have a large effect on the formation and durability of (micro-)bubbles in the sample which scatter light efficiently. Minimising bubbles and hence scattering for ‘true’ solutions is therefore key in order to obtain accurate absorption coefficients. The methods described in this chapter were found to minimise the formation of bubbles, reduce scattering in samples and solutions, and therefore return the highest quality absorption coefficients for the different measurement techniques.

2.1.1. *Preparation of coloured solutions*

A total of three different coloured solutions were used for the characterisation of the PSICAM. A black dye, called Nigrosine (Aldrich Chemistry, US), which absorbs broadly across the UV/VIS spectrum was used to calibrate the PSICAM. Humic acid (technical grade, Aldrich Chemistry) was used as a proxy for natural CDOM, exhibiting the same spectral absorption characteristics (exponentially increasing absorption with decreasing wavelength), and for validation of PSICAM performance in the blue/green. Lastly, a blue $CuSO_4$ (99+% analysis grade, Acros Organics, Belgium) solution was used to validate the performance of the PSICAM in the red/NIR range. All samples were made from strongly concentrated stock solutions which were filtered into 1L of freshly prepared purified water (Milli-Q; water purification system: Simplicity UV, Millipore) in a clean glass bottle. The stock was filtered through a 25 mm Spartan filter with a 0.2 μm pore size using a clean glass syringe. Filter and syringe were first rinsed 3 times with 20 mL purified water and later with a small volume (as filter blocks easily) of the stock solution before a few drops were diluted in the larger volume. Final concentrations used for calibration and validation were generally kept low so that the final solution did not exhibit any visible colour.

2.1.2. *Storage of natural water samples*

Three different absorption parameters were measured during field work campaigns: (1) total absorption of the untreated sample, (2) CDOM absorption of the sample after filtration through a 0.2 μm membrane filter and (3) filter pad absorption of the particulate material collected on a glass-fibre filter. Water samples were collected in Niskin bottles, mainly at depths close to the surface (< 10m) but datasets also include a few samples from greater depths. Two clean 1L glass bottles were filled with sample – one for the determination of total absorption coefficients and a second for CDOM absorption. The total absorption spectrum was measured as quickly as possible to avoid large temperature changes and alteration of the sample. The CDOM sample was kept in a water bath after filtration (Section 2.1.4) and measured as quickly as possible and always within a few hours of collection. Filter pad absorption measurements were conducted directly after the preparation of the sample filter, to minimise artefacts due to sample storage.

2.1.3. CDOM filtration

Filtration under high vacuum is likely to create microbubbles in the filtrate which scatter light and can cause large errors in absorption determinations. Pressure filtration was found to generate fewer bubbles than vacuum filtration. Hence, pressure filtration, with a syringe, was used whenever small volumes (< 40 mL) were needed, i.e. for spectrophotometer and LWCC measurements. Absorption measurements in the PSICAM, however, require approx. 400 - 500 mL of sample volume and syringe filtration was not feasible. Larger sample volumes were, therefore, filtered carefully with a vacuum < 0.2 bar regardless of the PSICAM's insensitive to scattering. Experiments with a dual-beam spectrophotometer which are generally most sensitive to the presence of scattering material showed that the absorption measured before and after low vacuum filtration remained virtually unchanged. This supports the assumption that formation of microbubbles during low vacuum filtration can be considered negligible. The low vacuum, additionally, minimises potential damage of phytoplankton cells and washing-out of pigments which reduces artefacts in filter pad absorption measurements and contamination of CDOM samples.

Natural CDOM samples were prepared by a two-step filtration. First, the sample was filtered through a 47 mm GF/F filter (Whatman, Germany) with a typical pore size of 0.5 µm (Chavez *et al.*, 1995) and then through a 47 mm Nitrocellulose membrane filter with a 0.22 µm pore size (GSWP, Merck Millipore Ltd., Ireland). The filtration units (funnel and flask), filter papers, filter holders and glass bottle were rinsed with purified water followed by approx. 200 mL of sample prior to each filtration.

2.2. Determination of absorption by coloured solutions in a dual-beam spectrophotometer

Absorption determinations of liquids in a dual-beam spectrophotometer were only conducted on artificial samples in the laboratory. For the initial characterisation of the PSICAM, spectrophotometric measurements using a cuvette were used for calibration and comparison. The spectrophotometer (UV2501-PC, Shimadzu Corp., Japan) was allowed to warm up and stabilise for 1 hour before the first measurement. A baseline was recorded with purified water in both cells. The OD was measured spectrally and in triplicate using 10cm quartz-glass cuvettes alternating purified water and the sample solution, finishing with an additional

reference measurement. Each measurement consisted of 5 sample scans and spectra were typically obtained with a 2 nm resolution, resulting in a total acquisition time of a few minutes. Measurements of purified water were used to monitor the stability of the baseline. Sample spectra were corrected for drifts in the baseline by subtracting the corresponding reference measurements.

The temperature of the liquid in both cuvettes was measured at the end of each set of five scans, when it was most stable, and used for temperature correction. The first recorded spectrum typically showed the largest temperature effect. It was therefore neglected in subsequent analysis and the remaining four spectra were averaged. Finally, the spectral absorption coefficient, $a(\lambda)$, was calculated (Eq. 1.15) and corrected for remaining temperature differences between reference and sample cell (Eq. 1.12).

2.3. Absorption measurements with a long-pathlength system

LWCC measurements were mainly used for absorption determination in the field as required for the calibration and the characterisation of the PSICAM performance for determination of absorption by natural CDOM.

2.3.1. Set-up and measurement procedure

All long-pathlength system absorption determinations were performed with a 1 m liquid waveguide capillary cell (LWCC, World Precision Instruments Inc., US). A Deuterium/Halogen lamp with internal shutter (DH-2000-BAL, Ocean Optics Inc., US) was used to illuminate the sample in the UV/VIS/NIR spectral region. Fibre optic bundles (Ocean Optics Inc.) guided light from the lamp to the LWCC and to the detector, a photo-diode mini spectrometer (AvaSpec ULS2048XL, Avantes, Netherlands).

Reference and sample solutions were injected into the LWCC through a 25 mm Spartan filter (Whatman) which had been rinsed with 36 mL of purified water using a 12 mL plastic syringe. Three separate syringes were used for absorption determinations: one for the sample and two for the injection of purified water in order to minimise contamination of the reference (one to rinse, the second to inject clean reference material). No pressure was applied to the syringe in the moment a spectrum was recorded and readings were taken quickly to minimise temperature change of the sample. Sample and purified water were

measured alternatingly starting and ending with the reference. Reference spectra were used to check for changes in the baseline and to correct for drifts if necessary. Absorption coefficients were calculated according to Eq. 1.15 with d = 1 m.

2.3.2. Temperature and salinity correction for LWCC measurements

Monitoring and control of sample temperatures inside the LWCC is not feasible. To minimise temperature effects and artefacts in NIR absorption coefficients, samples and purified water were stored in a water bath for several hours before a measurement. The LWCC was filled with purified water to allow the cell material to heat up and reach ambient temperature. Sample and reference temperature were recorded just before the injection into the cell but measured temperature differences were not representative as sample and reference heat up quickly and not necessarily at the same rate. Absorption spectra were therefore checked for visible temperature effects after baseline correction and manually corrected for small temperature changes (< 0.5 °C).

LWCC measurements are strongly affected by changes in the refractive index caused by variations in the salinity of the sample. The presence of salt ions introduces a high frequency pattern to the absorption spectra which is very difficult to correct. Bin-averaging of the data, however, can remove this feature to some degree. Salinity correction coefficients are instrument specific and have to be determined regularly, as they can change with set-up (Röttgers, pers. comm.). Coefficients were determined by measuring the absorption of a series of different NaCl solutions (> 99.5%, Sigma Chemicals Co.). To minimise measurement uncertainties, solutions should theoretically be as highly concentrated as possible. For example, Röttgers *et al.* (2014b) use a single concentration of roughly 70 g L^{-1}. However, although the changes in pure water absorption increase linearly with salinity, this is not necessarily true for instrument specific coefficients.

Measurements of a series of nine NaCl dilutions showed that LWCC absorption coefficients were not linearly related to the NaCl concentration > 60 g L^{-1} (Fig. 2.1), across all wavelengths. This is presumably due to a non-linear increase in scattering by salt ions at high concentrations (Zhang and Hu, 2009) which is supported by the fact that PSICAM measurements at higher NaCl concentrations do not show this non-linear trend (data not shown). The presence of salt also has an effect on the refractive index and thereby the effective pathlength which is another potential driver for non-linear increase in absorption.

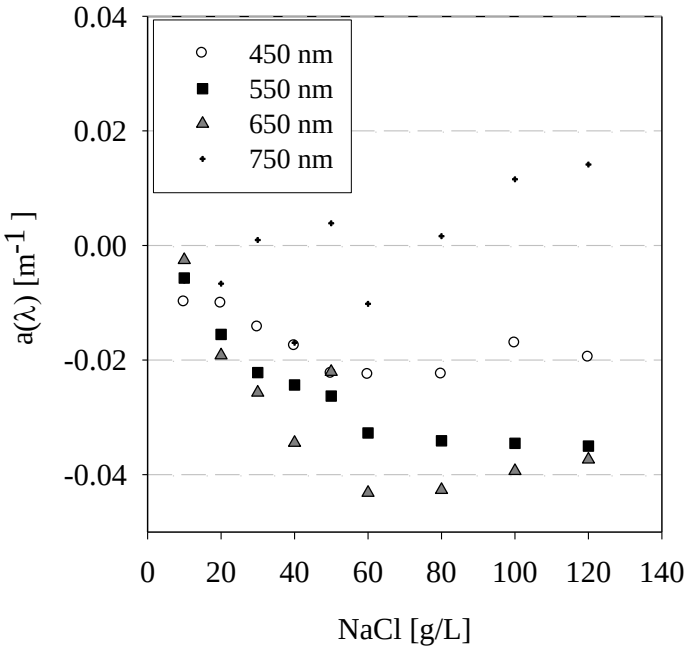

Fig. 2.1 Absorption coefficients of 9 different NaCl concentrations against the respective mass concentration. Data exhibit a clear non-linear trend for higher NaCl concentrations.

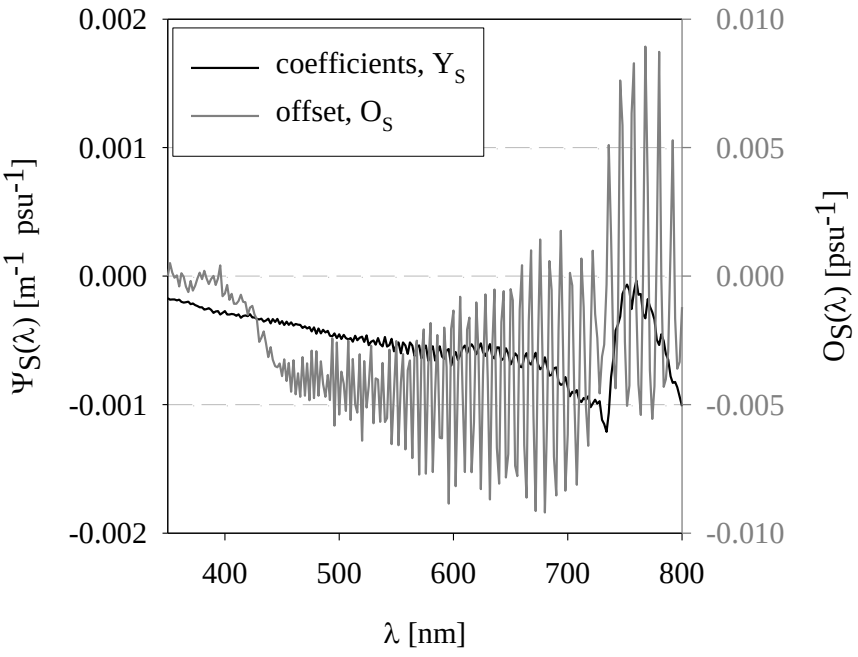

Fig. 2.2 Salinity correction coefficients for LWCC measurements. Absorption spectra are corrected by an offset correction (grey) and a salinity dependent slope which is scaled by the concentration (black).

If a single concentration is used to derive salinity correction coefficients, it is therefore recommended to obtain LWCC salinity correction coefficients at NaCl concentrations < 60 g L^{-1}, ideally close to the typical sample salinity around 35 g L^{-1}. Salinity coefficients will, however, have high uncertainties, particularly in the UV/blue region where contamination is a major issue. This approach might be a compromise for determinations during time sensitive field work campaigns. Alternatively, measurements of a series of different concentrations 10 – 60 g L^{-1} can be used to obtain correction coefficients (a slope and offset; Fig. 2.2) through linear regression. This regression approach was used for all data presented in this thesis.

LWCC absorption spectra are corrected for salinity using

$$a_{corrected}(\lambda,T,S) = a_m(\lambda,T,S) - (S - S_0)\,\Psi_S(\lambda) - O_S(\lambda) \qquad [m^{-1}] \qquad [2.1]$$

where $a_{corrected}$ is the corrected absorption coefficients at wavelength, λ [nm], a_m is the measured absorption coefficients, S [psu], is the sample salinity, S_0 is the reference salinity (= *0*, if purified water is used as reference). Ψ_S [m^{-1} psu^{-1}] and O_S [m^{-1}] are the slope and the offset of the salinity correction coefficients.

2.4. PSICAM measurements

2.4.1. Theory and calculations

Kirk (1997) and Leathers *et al.* (2000) developed the equations to obtain spectral absorption coefficients in a PSICAM based on RT theory. The nomenclature used in this work was modified slightly to fit the practical measurement procedure.

The absorption determination in the PSICAM is based on measurements of the light intensity (irradiance) at the cavity wall when it is filled with either a reference, R, or sample, S, material. The ratio of these two diffuse reflected irradiances, I_S/I_R, is defined as the transmission, T_{SR} (Eq. 2.2). I, in general, is proportional to the average number of times a photon is reflected by the wall, N_C, before being absorbed by the wall or the fluid.

$$T_{SR} = \frac{I_S}{I_R} = \frac{N_C^S}{N_C^R} \qquad [-] \qquad [2.2]$$

N_C is dependent on the probability, P_0, that a photon coming from the central light source reaches the wall directly, on the probability, P_S, that a reflected photon will reach the wall again and the reflectivity, ρ, of the wall itself. For the PSICAM set-up used here including a radiance sensor with a narrow field of view, N_C can also be expressed as the sum of the number of photons reaching the wall directly and the number of photons returning to the wall for a second time, third time etc. (Eq. 2.3).

$$N_C = P_0 \rho P_S + P_0 \rho^2 P_S^2 + ... = P_0 \sum_{n=1}^{\infty} (\rho P_S)^n = \frac{\rho P_0 P_S}{1-\rho P_S} \qquad [-] \qquad [2.3]$$

Therefore

$$T_{SR} = \frac{P_0^S P_S^S (1 - \rho P_S^R)}{P_0^R P_S^R (1 - \rho P_S^S)} \qquad [-] \qquad [2.4]$$

Using a spherical light source with radius, r_S [m], to generate the diffuse light field inside a cavity with radius r [m], the probability, P_0, is calculated using

$$P_0(a,r_0) = \exp(-ar_0) \qquad [-] \qquad [2.5]$$

where $r_0 = r - r_s$ [m]. For a non-scattering solution, P_S can be obtained using

$$P_S(a,r) = \frac{1}{2a^2r^2} [1 - \exp(-2ar) (2ar+1)] \qquad [-] \qquad [2.6]$$

From Eqs. 2.4 - 2.6 the transmission measured in the PSICAM can be related to the absorption coefficients of sample and reference solution using

$$T_{SR} = \exp [-r_0 (a_S - a_R)] \left[\frac{1 - \rho P_S(a_R,r)}{1 - \rho P_S(a_S,r)} \frac{P_S(a_S,r)}{P_S(a_R,r)}\right] \qquad [-] \qquad [2.7]$$

In order to obtain the absorption coefficient of a sample, a_S, the reflectivity, ρ, has to be determined during a calibration following the suggestions of Leathers *et al.* (2000). For the calibration the transmittance, T_{AB}, is determined using Eq. 2.2. Therefore, the light intensities, I_A and I_B, are measured inside the cavity for a calibration solution A, usually Nigrosine, and a reference solution B, usually purified water, respectively. The absorption

coefficients a_A and a_B of the respective solutions, A and B, have to be known or determined spectrophotometrically. Note that a_A represents the total absorption, i.e. the absorption coefficient of Nigrosine plus the absorption by water and can therefore not be smaller than a_B. If purified water is used as reference, the absorption coefficient, a_B, can be taken from the literature (Section 1.4.1). ρ is then given by

$$\rho = \frac{T_{AB}\exp(-a_B r_0)\,P_S(a_B,r) - \exp(-a_A r_0)\,P_S(a_A,r)}{T_{AB}\exp(-a_B r_0)\,P_S(a_A,r)\,P_S(a_B,r) - \exp(-a_A r_0)\,P_S(a_B,r)P_S(a_A,r)} \qquad [-] \qquad [2.8]$$

Once ρ has been determined, the absorption coefficient, a_S, can be obtained numerically. The transmission, $T_{meas} = I_S/I_R$, for a sample reference pair is determined and, for a known a_R, the least-squared function $G(a(\lambda))$ (Eq. 2.9) is minimised for $T_{SR}(a(\lambda))$ and $P_S(a(\lambda))$ using Eq. 2.7 and Eq. 2.6.

$$G(a_{(\lambda)}) = \sqrt{(T_{SR} - T_{meas})^2} \qquad [2.9]$$

2.4.2. PSICAM set-up

The PSICAM set-up (Fig. 1.7) used for the work presented here was built following the description by Röttgers *et al.* (2005, 2007). The cavity was made from OP.DI.MA (Gigahertz-Optic, Germany), a highly diffuse reflective material. The material has a reflectivity of about 98% according to the manufacturer and is water repellent on short time scales so particulate material can be washed off easily. The light source consisted of a 10.0 mm diameter quartz-glass sphere that was placed in the centre of the cavity which has an inner radius of 4.5 cm (i.e. r_0 = 0.04 m). An electronically stabilized 150 W halogen lamp (CF1000, Illumination Technology) was connected to the small scattering sphere using a glass fibre bundle. The light inside the cavity was collected by another quartz-glass fibre bundle, entering the cavity parallel to the central light source, and guided to a photodiode array detector, AvaSpec ULS2048XL. The small viewing angle of the fibre ensured that no light was collected directly from the light source. As any fluid filled into the cavity will enter the micro-pores of the wall material eventually, the cavity was pre-soaked by filling it with purified water at least 12 hours before any experiments were conducted. The lamp was allowed to stabilize for at least 1 hour before first measurements were taken.

The stability of the lamp and the light field inside the cavity were assessed and found to be within 6% of the transmitted signal from 400 - 700 nm over a time period of 45 mins. Towards the edges of the spectrum, absolute noise in the signal increases and in combination with dropping signal levels can result in high relative errors of typically up to 10% and a maximum of 50% at 350 nm (data not shown). As the light field only has to be stable for the time it takes to record a pair of sample and reference measurements – typically a few minutes, the stability of the light source is not considered a major source of error in PSICAM absorption determinations. Small changes in the lamp output between the calibration and a measurement are also not problematic because all intensities are considered relative to reference intensity which essentially compensates for small instabilities. The larger variability in the UV, however, potentially limits the accuracy of the PSICAM for wavelengths < 400 nm.

2.4.3. PSICAM calibration

The accuracy of the PSICAM is limited by the accurate determination of the reflectivity of the inner cavity walls, ρ. Lerebourg *et al.* (2002) have shown that a 1% error in the reflectivity leads to a 10% error in the absorption measured in the PSICAM. Therefore the calibration has to be performed extremely carefully.

A Nigrosine solution was prepared as described in Section 2.1.1. At the beginning of each calibration the PSICAM was bleached with a sodium hypochlorite solution (6 - 14% NaOCl, Sigma Aldrich Co.) for about 15 mins. Afterwards, the cavity was rinsed thoroughly under running tap water and finally twice with purified water. The PSICAM was filled with purified water and lamp intensity and integration time were adjusted so that a signal of about 50,000 counts was achieved. The intensity inside the cavity was measured twice, first when filled with purified water and secondly, when filled with the calibration solution. The sphere has to be bleached and rinsed every time it is filled with Nigrosine because the dye quickly sticks to the walls. After bleaching, another measurement of the light intensity for purified water was made to monitor the stability of the system. The reference intensity for each sample measurement is obtained by averaging the previous and subsequent purified water spectrum. This compensates for potential drifts of the light intensity inside the cavity. This calibration should be performed daily and at least in triplicate (not necessarily consecutively) to obtain an accurate reflectivity of the PSICAM. During field work campaigns or longer experiments the replicates were spread over the course of a day in order to monitor changes in the wall's reflectivity. During all measurements, the cavity was covered with a thick black

cloth to prevent any ambient light entering the sphere from the outside. The temperature of each fluid inside the cavity was recorded just before each measurement for temperature correction of the pure water absorption. One measurement (either reference or sample) typically takes less than 20 seconds and heating of the sample was considered negligible.

The absorption coefficient of the calibration solution has to be known for the calculation of ρ. The absorption of the Nigrosine solution was determined spectrophotometrically, either in a standard spectrophotometer with a 10 cm cuvette in 2013 and early 2014. Later this approached was revised and measurements were conducted using a LWCC system because measurements were found to be less time consuming and more stable on a moving ship. No syringe filter was used for the LWCC determination of Nigrosine absorption coefficients because this was found to remove absorbing material from the solution, due to its dye characteristics. The LWCC was bleached to reduce the risk of contamination after each determination of Nigrosine absorption even though Nigrosine did not seem to affect the cell's performance.

2.4.4. PSICAM measurement procedure

The absorption determination of an unknown sample was performed similar to the PSICAM calibration with the exception that no bleaching of the cavity was required. Lamp intensity and integration time were adjusted to return a detector response of about 50,000 counts when the cavity was filled with purified water. Measurements were conducted in triplicate, alternating measurements of purified water and the sample, finishing with a final reference measurement. Sample and reference temperatures were noted before each measurement to apply a temperature correction during subsequent data processing. For natural samples, the total absorption was determined directly after sampling to minimise temperature changes and their effects on phytoplankton cells. The salinity of the sample was recorded to correct for the salinity dependence of pure water absorption. Finally, the spectral absorption coefficient of CDOM was measured in triplicate.

2.4.5. Correction of chlorophyll fluorescence effects

Absorption coefficients determined for an unfiltered sample were corrected for chlorophyll fluorescence effects following the descriptions in Röttgers *et al.* (2007, 2016). This required additional measurements of the intensity inside the cavity which were made using a short pass filter, restricting the illumination to wavelengths shorter than 620 nm. The total light

emitted by fluorescence, I_{fl_tot}, can be calculated from the measurements of reference and sample intensities, I_{ref_fl} and I_{sam_fl}, with the filter in place using

$$I_{fl\_tot} = \frac{I_{sam\_fl}}{T_{SR}} - I_{ref\_fl} \qquad \text{[counts]} \qquad [2.10]$$

where $T_{SR} = I_S/I_R$ is used to correct for the amount of fluorescence that is re-absorbed by the sample and determined from measurements without the short pass filter.

A portion of the total fluorescence is absorbed by the sample and the fluorescence signal measured by the detector, I_{fl_meas}, can be approximated by

$$I_{fl\_meas} = I_{fl\_tot} \cdot T_{SR} = I_{sam\_fl} - I_{ref\_fl} \cdot T_{SR} \qquad \text{[counts]} \qquad [2.11]$$

The short-pass filter also absorbs a portion, *f*, of the light provided from 350 – 620 nm and measurements have to be corrected for the loss of excitation radiation. *f* can be calculated using

$$f = \frac{\sum_{\lambda=350\ nm}^{620\ nm} \left(I_{sam_{fl}} - I_{ref_{fl}}\right)}{\sum_{\lambda=350\ nm}^{620\ nm} \left(I_S - I_R\right)} \qquad \text{[-]} \qquad [2.12]$$

Using Eq. 2.11, the final fluorescence signal, I_{fl}, can be calculated as

$$I_{fl} = I_{fl\_meas} \cdot f \qquad \text{[counts]} \qquad [2.13]$$

Finally, a corrected transmission, T_{fl}, calculated using Eq. 2.14 can be used to derive corrected absorption coefficients according to Section 2.4.1.

$$T_{fl} = \frac{\left(I_S - I_{fl}\right)}{I_R} \qquad \text{[counts]} \qquad [2.14]$$

2.4.6. Temperature and salinity correction of PSICAM absorption data

A detailed description of the effects of changing temperature and salinity on PSICAM absorption measurements can be found in Röttgers *et al.* (2014b). Artefacts originate predominantly from changes in the refractive index (from sample to reference) which is dependent on temperature and salinity. In order to obtain instrument specific temperature coefficients a sample of 10 °C purified water was measured against a reference of purified water at 20 °C. Temperatures of both liquids were recorded before each reading was taken and temperature coefficients were calculated assuming a linear relationship between temperature and changes in absorption. The instrument specific correction coefficients were very similar to values of the temperature dependency of pure water absorption (Fig. 2.4; Sullivan *et al.*, 2006, Röttgers *et al.*, 2014b).

A series of 6 NaCl concentrations between 10 g L^{-1} and 100 g L^{-1} was used to obtain salinity correction coefficients for PSICAM measurements. The absorption of NaCl solutions was measured in triplicate against purified water as reference. Changes in absorption were found to be linearly related to changes in NaCl concentration and no significant offset was observed. 65% of the linear regression coefficients, R^2, were found to be greater than 0.8 between 400 - 800 nm. Salinity correction coefficients were found to be in good agreement with coefficients obtained for pure water absorption by Sullivan *et al.* (2006) (Fig. 2.5). The recently published coefficients of the salinity dependence of pure water determined with a dual-beam spectrophotometer and a PSICAM by Röttgers *et al.* (2014b) are generally lower than values presented here. This is because their values represent coefficients for the salinity dependence of pure water rather than correction coefficients for absorption measurements which include correction for complex interactions between the instrument and saline solutions. They applied a series of corrections to the data in order to remove instrument artefacts in the salinity dependency. Correction coefficients used here did, however, capture instrument specific features to allow their subsequent correction.

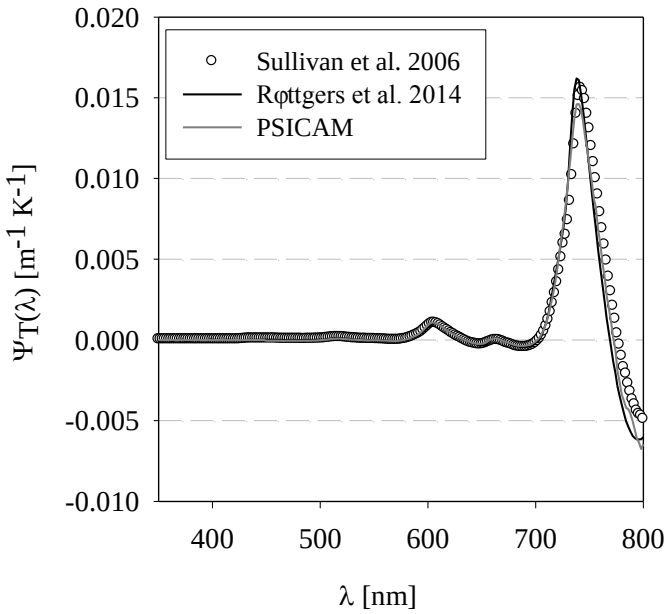

Fig. 2.3 Instrument specific correction coefficients for the temperature dependence of pure water absorption. Comparison with literature values of Sullivan *et al.* (2006) and Röttgers *et al.* (2014).

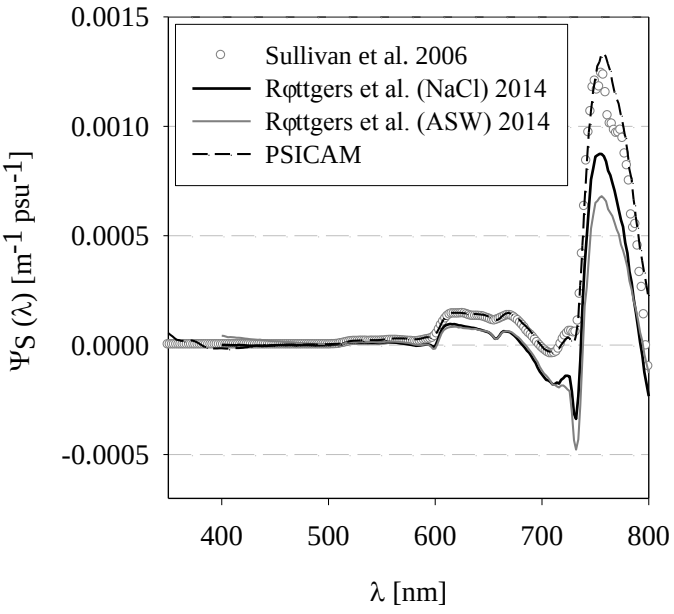

Fig. 2.4 Comparison between different recently published salinity correction coefficients and the instrument specific coefficients obtain for the PSICAM used in this study.

2.5. Filter pad absorption measurements

The OD of particulate matter collected on filter papers was measured in a dual-beam spectrophotometer (UV2501-PC, Shimadzu Corp., Japan) using the simple direct transmission method (T-method; Yentsch, 1962, Trüper and Yentsch, 1967, Mitchell, 1990). The spectrophotometer was allowed to warm up for 1 hour before the first measurement was taken. Two reference filters were prepared by running 300 mL of CDOM (filtered seawater) through 47 mm GF/F filter paper under a low vacuum. A baseline was recorded with no filters in the beams and a reference measurement was taken with the two rinsed filters attached to the alcohol-cleaned glass windows placed directly against the exit ports inside the spectrophotometer. Varying volumes of sample were filtered through 47mm GF/F filters (~ 0.5 μm pore size) using a low vacuum of < 200 mbar to reduce breakage of cells and loss of pigments. The volume was adjusted for each sample individually to avoid any artefacts due to saturation, non-linearity or limited sensitivity. Volumes were chosen so that the maximum OD was close to, but did not exceed, 0.4 OD. Funnel and filter paper were kept covered at all times to avoid contamination and the absorption was determined directly after filtration. Sample filters were hydrated with CDOM in between measurements. The OD of a filter was determined in a single scan to minimise artefacts due to heating or bleaching of the filter inside the spectrophotometer (alteration of the filter absorption by replicating the measurement was observed for multiple scans). Four different measurements were made against the same reference filter: (1) a reference to get a measure of the baseline, (2) the sample filter, (3) sample filter after bleach treatment and (4) a second scan of the reference filter used for (1) to monitor drifts in the baseline. Observed shifts were usually smaller than the measurement error. To remove all pigments from the filter, a few drops of dilute sodium hypochlorite where added to the filter paper and left until no colour changes could be observed anymore and for a maximum of 3 minutes. Incomplete bleaching was observed for any of the samples collected for this work. Afterwards the bleach was washed out by rinsing the filter with 300 mL of CDOM.

2.6. AC-9 absorption and attenuation measurements

The WETLabs AC-9 submersible absorption and attenuation meter was used to collect *in situ* profiles of $a(\lambda)$ and $c(\lambda)$ on three research cruises in 2009 and 2012 (Section 2.8.1 –

2.8.2). A detailed description of the AC-9 set-up and principle can be found in Twardowski *et al.* (1999). Measurements were conducted broadly following the methodology described in the AC-9 manual and protocols (WETLabs Inc., 2008, 2011). Absorption and attenuation coefficients were determined for nine different wavebands (10 nm FWHM) centred on 412, 440, 488, 510, 532, 555, 650, 676 and 715 nm. The 25 cm pathlength AC-9 was calibrated and refurbished by the manufacturer in 2008 and 2013. Additional calibrations were performed before and during each cruise measuring signals when ultrapure water (Milli-Q, Millipore) was pumped through the instrument.

Data were corrected for the temperature and salinity dependence of pure seawater (Pegau *et al.*, 1997) and for scattering errors using three different correction methods: (1) the proportional correction by Zaneveld *et al.* (1994), (2) the semi-empirical correction (Röttgers *et al.*, 2013) and (3) the iterative method (McKee *et al.*, 2014). A detailed description and discussion of the scattering corrections can be found in Chapter 5.

2.7. Algal culture data

Two different sets of algal cultures were used addressing two questions investigated in this work: (1) the AC-IOPs dataset was used to assess the variability and measurement uncertainties in filter pad absorption measurements (Chapter 4) and had been collected as part of an experiment investigating IOPs of algal cultures and (2) the second dataset was used to investigate the magnitude of inelastic scattering effects in PSICAM measurements (Chapter 5). All cultures with one exception were provided by the Culture Collection of Algae and Protozoa (CCAP, Oban). No information was available on the growth phase in which these cultures were sample.

2.7.1. AC-IOPs dataset

This dataset (AC-IOPs) was collected during a series of laboratory experiments at the Scottish Association for Marine Science (SAMS) in Oban in June 2014. Total absorption and CDOM absorption of 14 different samples were prepared as dilutions from nine different cultured algal species and measured in a PSICAM. Additional data included CDOM absorption measured with a LWCC system and filter pad absorption measured with a dual-beam spectrophotometer.

Table 2.1 Details on nine algal species, their origin and culturing conditions, which were used to compose the AC-IOP dataset. Cultures were grown at SAMS, Oban, UK, and used for the assessment of uncertainties in filter pad absorption determination.

species	type	medium	source	Prod./ no	isolation
Alexandrium minutum	dino-flagellate	marine L1	CCAP, SAMS	1119/50	2008, Scapa, Orkney (58° 55'N 003° 06' W)
Alexandrium temarense	dino-flagellate	marine L1	CCAP, SAMS	1119/28	2008, Scapa, Orkney (58° 55'N 003° 06' W)
Heterocapsa spp.	dino-flagellate	marine L1	CCAP, SAMS	1125/4	2011, Argyllshire
Karenia mikimotoi	dino-flagellate	marine L1	SCCAP	K-0260	1977, Oslofjorden, Norway
Microcystis aeruginosa	cyano-bacteria	fresh water BG11	CCAP, SAMS	1450/2	1954, Little Rideau Lake, Ontario, Canada
Pseudonitzschia seriata	diatom	marine L1 + silica	CCAP, SAMS	1061/42	2012, Loch Creran, Argyll
Scripsiella sp.	dino-flagellate	marine L1	CCAP, SAMS	1134/8	2003, LY5 sampling site (SAMS)
Skeletonema marinoi	diatom	marine L1 + silica	CCAP, SAMS	1077/5	1956, Long Island Sound, Milford Harbour, Connecticut
Synechococcus sp.	cyano-bacteria	fresh water BG11	CCAP, SAMS	1479/9	1989, South Basin, Windermere, Cumbria, England, UK

Table 2.2 Summary of cultures used to investigate the magnitude of inelastic scattering signals in PSICAM measurements – type, medium and origin.

species	type	medium	source	Prod./ no	isolation
Dunaliella maritima	green algae	2 ASW	CCAP, SAMS	19/1	1938, Lacal Sarat, Romania
Phaeodactylum tricornutum	diatom	F/2 + Si	CCAP, SAMS	1055/1	2003, Blackpool, England
Arthrospira maxima	cyano-bacteria	ASW:BG	CCAP, SAMS	1475/9	1963, Lake Tchad, Africa
Synechococcus sp.	cyano-bacteria	fresh water BG11	CCAP, SAMS	1479/9	1989, South Basin, Windermere, Cumbria, England, UK

The dataset contained a total of nine different algal species which were cultured in the Scottish Association for Marine Science (SAMS) by Rebecca Weeks. All cultures were grown at 15 °C with a 12h dark/light cycle and in L1 medium (dinoflagellates), L1 medium + silica (diatoms) and in BG fresh water (cyanobacteria). Detailed information on these cultures is given in Table 2.1. The concentrated cultures were diluted in filtered seawater (or distilled water in case of cyanobacteria) to make up the final sample.

2.7.2. Cultures used for investigating phytoplankton fluorescence

A second set of cultures included four different types of micro algae which were grown at the University of Strathclyde at 16 °C in a 12 hour dark/light cycle and varying media (Table 2.2). Samples were made up by diluting some of the culture in artificial sea water (34 g L^{-1} ASW; Ultramarine synthetica sea salt, Waterlife Research Ltd.) or distilled water and measured within 24h. Spectral absorption and fluorescence data of these samples compose this dataset.

2.8. Field data

2.8.1. Ligurian Sea cruise - 2009

This dataset (LS) includes 46 profiles of IOP and radiometric data and was used to investigate the degree to which optical closure is currently achievable (Chapter 5). Additional IOP measurements were made for 62 discrete water samples used for the analysis of filter pad absorption measurements in Chapter 4. Collection and initial processing of these data were not part of this project. Data from this cruise have been published previously (McKee *et al.*, 2013, McKee *et al.*, 2014). Underwater light fields were modelled using Hydrolight by Dr. Fethi Bengil. All subsequent analysis and evaluation of optical closure performance using this dataset, however, were part of this project.

Data were collected on board *NRV Alliance* in the Ligurian Sea in March 2009 (Fig. 2.6). Stations ranged from deep, clear oceanic waters (classic Case 1) to shallow, turbid stations including some in the plume of the river Arno. Chlorophyll concentrations varied between 0.29 – 3.31 mg m^{-3}, total suspended solids from 0.133 – 3.77 g m^{-3} and a_{CDOM}(440nm) from 0.012 – 0.19 m^{-1}.

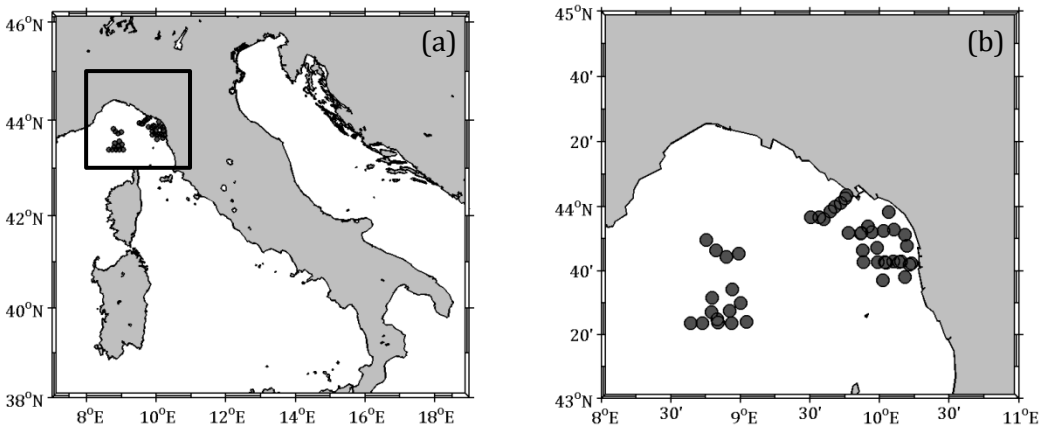

Fig. 2.5 (a) Ligurian Sea study area, (b) sampling sites of the cruise in the Ligurian Sea in March 2009. The dataset includes both deep oceanic and shallow coastal waters.

Profiles of absorption and attenuation coefficients were determined with an AC-9 as described above (Section 2.6). A WETLabs BB-9 was mounted alongside the AC-9 to make concurrent depth profile measurements of backscattering coefficients for surface waters. The instrument was calibrated by the manufacturer in 2007 (Moore *et al.*, 2000). Backscattering coefficients were calculated based on measurements of the volume scattering function (VSF) at an effective scattering angle of 117°, for nine wavebands at 412, 440, 488, 510, 532, 595, 650, 676 and 715 nm. Backscattering data were subsequently interpolated to AC-9 wavelengths and measurements were corrected according to the BB-9 manual (WETLabs Inc., 2010), including: correction for pathlength absorption was performed using AC-9 absorption data corrected with the proportional method (Zaneveld *et al.*, 1994); the total VSF was converted to particulate VSF by subtraction of water VSF calculated from Morel (1974); $\beta_p(117°,\lambda)$ was converted to particulate backscattering coefficient, $b_{bp}(\lambda)$ using a χ-factor of 1.1, as suggested by Boss and Pegau (2001). It should be noted that no dark signals were measured on board. However, particulate backscattering coefficients observed were always > 0.001 m^{-1} and the effect of drifting dark signals can be considered negligible (Twardowski *et al.*, 2007).

Radiometric data were collected using a free-falling HyperPro profiler (Satlantic Inc., Canada) configured with hyperspectral downwards irradiance, $E_d(z,\lambda)$, and upwards radiance, $L_u(z,\lambda)$ sensors. Both sensors had been characterized and calibrated by the manufacturer in early 2008. The profiling radiometer was deployed in a multicast mode to sample the surface layer repeatedly at each station to maximise accuracy of light fields in the top 10 m (Zibordi *et al.*, 2004). In addition, where possible, a deep cast was collected to

study light penetration below the surface layer. A full set of radiometric casts was typically measured within 20 minutes. During this time the ships angle towards the sun was kept constant whilst the vessel was allowed to drift with the current. The final profile for each station was calculated as median of all casts with a 1 m resolution.

A spectral stray-light correction (SLC) was applied to all radiometric data collected with the HyperPro following the suggestions of the NASA Carbon Cycle & Ecosystem Joint Science Workshop (Voss *et al.*, 2008). The SLC in a spectroradiometer can be described by the instrument's spectral line spread function (SLSF). SLC was performed at the NIST Spectral Irradiance and Radiance Responsivity Calibrations using Uniform Sources (SIRCUS) by characterizing the scattering properties of spectrographs and imaging systems using five continuously tuneable lasers (400 to 800 nm) to reduce the magnitude of errors arising from spectral and spatial stray light by one to two orders of magnitude. This additional correction leads to slightly lower E_d and L_u values compared to the uncorrected HyperPro data, especially at wavelengths in the blue.

Measurement artefacts in radiometric profile data were reduced following NASA protocols (Volume III; Mueller, 2003): the ship was positioned so that ship shadow effects were minimised and a deck reference sensor was mounted on the ship's superstructure measuring downwelling above surface irradiance, $E_S(\lambda)$ [W m^{-2} nm^{-1}]. All underwater radiometry profiles were corrected for changes in the incident solar radiation during a cast sequence by normalising to coincident surface irradiance data, $E_S(t,\lambda)$ and then rescaling to the median surface irradiance, $\langle E_S(t, \lambda)\rangle$, calculated over the duration of the *in situ* profiles using

$$\hat{I}_x(\lambda,z)= \frac{I_x(\lambda,z)\langle E_s(t,\lambda)\rangle}{E_s(t,\lambda)} \qquad [2.15]$$

where I_X represents any of E_d, L_u or E_u. Surface irradiance data were smoothed in time to reduce potential artefacts associated with ship movement. Multicast profiles were merged into a single profile before final processing. All radiometric profile data were filtered to remove high tilt values and outliers (outside 95% prediction intervals) associated with wave focussing effects were also removed. A more detailed description of the processing of radiometric profiles can be found in Sanjuan Calzado *et al.* (2011).

2.8.2. West Coast of Scotland cruise - 2012

Data were collected on board *R/V Prince Madog* off the West Coast of Scotland prior to the period of study in June 2012 (WCS dataset; Fig. 2.7). Subsequent processing and analysis of the data has been undertaken as part of this work. The sampling covered various water types including moderately turbid coastal waters, reasonably clear, potential Case 1 waters, and a *coccolithophore* bloom on the edge of the continental shelf. Chlorophyll concentrations covered a range of 0.71 – 2.51 mg m^{-3}, total suspended solids varied between 0.91 – 4.02 g m^{-3} and a_{CDOM}(440nm) between 0.08 – 0.22 m^{-1}.

AC-9 measurements were used to determine attenuation and absorption coefficient profiles as described in Section 2.6. Profiles of spectral backscattering coefficients were determined from BB-9 measurements following the same protocol as on the LS cruise. The instrument was re-calibrated by the manufacturer after the cruise in 2013 and the new calibration was applied retrospectively. Although retrospective calibration is not ideal, this approach was considered to represent the state of the instrument at the time of data acquisition better than the previous calibration performed in 2007. All measured backscattering data were reasonably high and, hence, not significantly affected by potential drift in the dark counts between measurement and calibration. The calculation of $b_{bp}(\lambda)$ was revised and coefficients were calculated using $\chi = 0.9$ according to Sullivan *et al.* (2005).

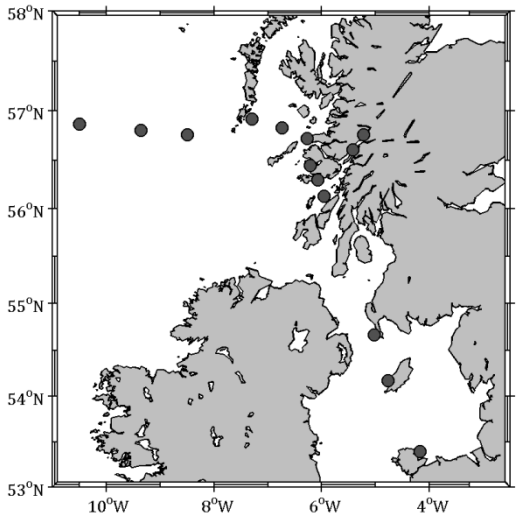

Fig. 2.6 Station locations for the cruise off the west coast of Scotland sampled in June 2012.

Radiometric data collected off the West Coast of Scotland in 2012 were measured with TriOS RAMSES hyperspectral radiometers giving upwards radiance, $L_u(\lambda,z)$, upwards irradiance, $E_u(\lambda,z)$, and downwards irradiance, $E_d(\lambda,z)$. This profiling package was lowered to specific depths and data accumulated over a two minute period at each depth. In this case, the final radiometry profile was composed of median values of each radiometric parameter at each depth step. Data were corrected for changes in the incident surface irradiance (Eq. 2.15). During re-calibration of all sensors post-cruise, damage to the E_s sensor was discovered. Post-cruise re-calibration of the E_s sensor produced above surface $E_s(\lambda)$ data that was subsequently found to be inconsistent with below surface $E_d(\lambda)$ data, tested by RT modelling. This was attributed to further degradation of the sensor between the cruise in 2012 and the re-calibration in 2015. Therefore, it was necessary to adopt an alternative strategy to derive above surface $E_s(\lambda)$ data for input to RT models. This involved extrapolating $E_d(555, z)$ up to and through the sea surface and using this value to rescale measured E_s spectra using

$$E_{s,\,corrected}(\lambda) = \frac{E_s(\lambda)\, E_d(555, 0^+)}{E_s(555)} \qquad [W\ m^{-2}\ nm^{-1}] \qquad [2.16]$$

where $E_{s,corrected}(\lambda)$ is the corrected spectral sky irradiance, $E_s(\lambda)$ is the measured solar downwards irradiance and $E_d(555,0+)$ is the above surface irradiance at 555 nm, derived from extrapolation of $E_d(555,z)$.

The performance of this approach was assessed by comparing measured and modelled $E_d(\lambda)$ data at the shallowest depth available. Fig. 2.8 demonstrates that this approach provides input $E_s(\lambda)$ data that are consistent with subsurface $E_d(\lambda)$ data across the full spectral range considered here. Although this approach limits one degree of freedom, analysis of optical closure for $E_d(\lambda)$ at depth and for $L_u(\lambda)$ and other associated products remains valid.

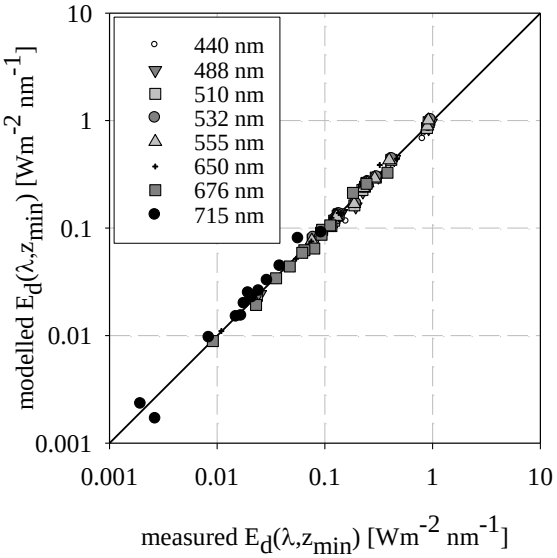

Fig. 2.7 Comparison of modelled and measured subsurface E_d values verifying the corrections applied to derive E_s. Input AC-9 data has been corrected using the proportional correction.

2.8.3. UK coastal waters cruise - 2015

Data were collected on a cruise on *R/V Heincke* in spring 2015 circumnavigating Great Britain (UKWC dataset). The 62 sample sites included stations in the English Channel, Bristol Channel, several Scottish sea lochs, the East Coast of Scotland close to the River Tay and River Forth estuaries as well as several stations in the central North Sea (Fig. 2.9). Water types varied from sediment dominated river plumes, various coastal waters and the start of a phytoplankton spring bloom in Loch Fyne.

In situ IOP profiles of backscattering, absorption and attenuation coefficients were determined with BB-9 and AC-9 instruments using the same methodology as on the WCS cruise in 2012 (Section 2.8.2). In addition to *in situ* profiles, absorption spectra of discrete water samples (mainly surface waters) were measured on board including total, CDOM and particulate absorption determination with two PSICAMs, CDOM absorption measurements with a 1 m long-pathlength LWCC system, and filter pad absorption measurement made with three different methods: (1) using the T-method in a simple spectrophotometer set-up (Section 2.6.) and (2) two additional measurements based on the integrating cavity approach (IS-method and QFT-CAM), made by the Helmholtz-Zentrum Geesthacht (HZG). Both PSICAMs were calibrated several times a day using fresh aliquots from the same Nigrosine

solution. In total 63 spectra of total absorption, 59 CDOM absorption spectra and 51 filter pad absorption spectra (made with all three configurations) were collected. Some samples and stations were excluded based on concerns about contamination of the samples due to residual bleach in the PSICAM cavity. This contamination could be observed as continuing decrease UV/blue absorption in replicate measurements. Sample filtration, measurements and data processing in the laboratory were conducted completely independently by two different research groups. LWCC CDOM absorption spectra were offset corrected to match PSICAM data at 700 nm.

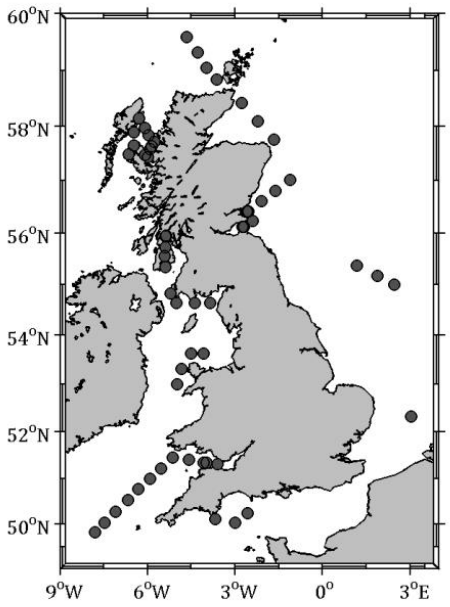

Fig. 2.8 Locations of stations sampled during a cruise around Great Britain on *R/V Heincke* in April 2015.

3. Calibration and validation of a point-source integrating cavity absorption meter (PSICAM)

3.1. Introduction

Obtaining accurate data on constituent absorption for marine waters is generally problematic because measurements are affected by scattering by particulate matter. Scattering leads to an overestimation of sample absorption and measurements have to be corrected for these effects. All commonly used absorption techniques directly operating on suspensions suffer from scattering errors to an often unknown extent.
Absorption measurements with a PSICAM were shown to be virtually unaffected by the presence of particulate matter and to benefit from an increased sensitivity due to a long optical pathlength (Kirk, 1997, Röttgers *et al.*, 2005). According to these studies, the PSICAM, enables the determination of 'true' absorption coefficients for natural water samples and potentially provides a standard which can be used to validate other absorption techniques and identify sources of uncertainties.

Having previously introduced the different absorption measurement concepts and protocols, this chapter will characterise the performance of the PSICAM in particular. Demonstrating the accuracy of PSICAM absorption data will form the foundation for further investigation of other techniques during this project. The aim is to establish the PSICAM as a credible standard which other absorption techniques can be compared against. This chapter will, therefore, focus on the determination of robust measurement uncertainties for PSICAM measurements and on understanding of the rather complex mathematics that underpin its operation.

The characterisation of the PSICAM includes:

1) Validating the accuracy of PSICAM absorption coefficients against dual-beam spectrophotometer and LWCC system measurements using a range of different non-scattering samples, from coloured solutions to natural CDOM.

2) Testing the sensitivity of PSICAM measurements to the presence of scattering material.

3) Assessing PSICAM measurement uncertainties, in terms of
   - precision of PSICAM measurements of turbid sample absorption and CDOM absorption.
   - differences in the standard deviation in triplicate measurements made with the dual-beam spectrophotometer, LWCC system and PSICAM.
   - overall uncertainties of the method which is achieved by comparing two independent PSICAMs.

4) Investigating the stability of PSICAM calibrations over time.

5) Using a theoretical approach to assess the sensitivity of PSICAM measurements and calculations to uncertainties in the various input parameters.

3.2. Accuracy of PSICAM absorption measurements

3.2.1. PSICAM comparison with a spectrophotometer

The initial validation of the PSICAM was demonstrated using coloured, non-scattering solutions. Spectral absorption coefficients of three solutions, Nigrosine, $CuSO_4$ and humic acid, were determined and compared to data obtained with a spectrophotometer equipped with a 10 cm cuvette.

Fig. 3.1 shows the agreement for absorption coefficients of 2 Nigrosine concentrations measured with the 2 instruments. PSICAM absorption coefficients were within ± 3% of spectrophotometer data for the higher concentration and within ± 5% for the lower concentration. A general increase in noise could be observed at red/NIR wavelengths. This is attributed to the high absorption by water, reducing detectable signals significantly (Fig. 3.2) which results in a generally lower signal-to-noise ratio. The temperature and salinity dependency of water absorption is also strongest in this spectral region. Although a large portion of these temperature and salinity effects can be corrected for, residual artefacts can lead to an increased deviation between two instruments. For the spectra shown in Fig. 3.1, the deviations exceeded 10% for wavelengths greater than 780 nm which can be attributed to these residual temperature effects.

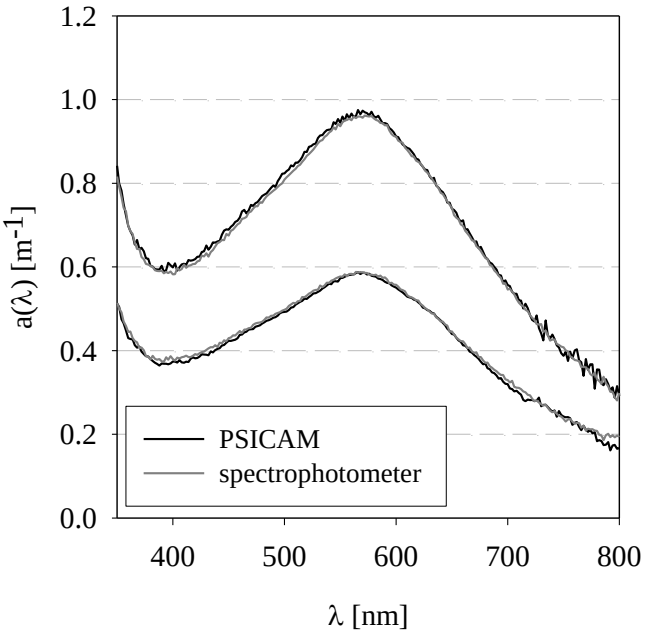

Fig. 3.1 Comparison of spectral absorption coefficients of 2 different Nigrosine concentrations measured in a PSICAM and a dual-beam spectrophotometer with a 10 cm glass cuvette.

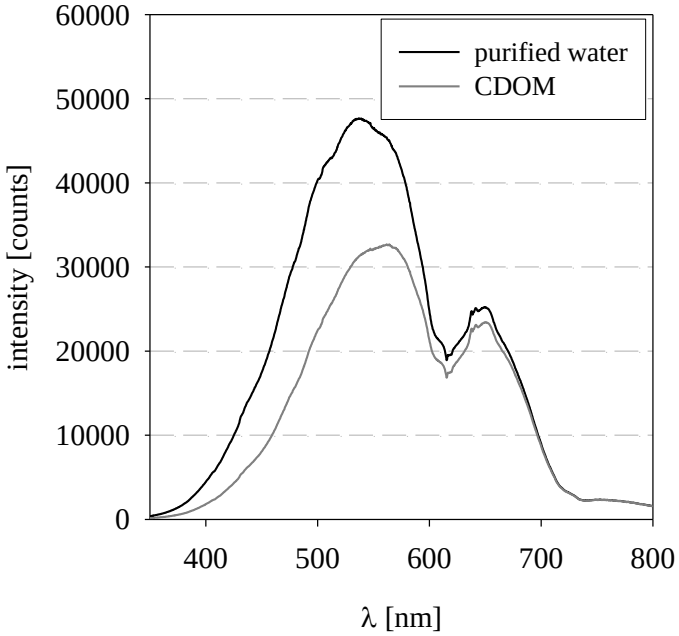

Fig. 3.2 Intensity spectra measured inside the PSICAM when the cavity is filled with pure water and a humic acid (CDOM) sample.

Nigrosine solutions, however, are also used to calibrate the PSICAM, so 2 additional comparisons are made using solutions absorbing in different spectral regions to eliminate potential bias. Humic acid (CDOM) was used to assess the performance in the UV/blue (Fig. 3.3), with spectra generally showing very good agreement for wavelengths between 400 – 800 nm, with an absolute deviation of less than 0.01 m^{-1}. Fig. 3.3 also shows that the PSICAM tends to underestimate other instruments in the UV (typically < 400 nm) by about 10 - 15%. The increased deviation between the two instruments is due to very low signals, typically of a few hundred counts compared to high signals of up to 50,000 counts in the green (Fig. 3.2). Signals are low because of a combination of low lamp output, the low sensitivity of the photo-diode detector at shorter wavelengths and high sample absorption. These in turn lead to a potentially higher sensitivity to internal detector stray light issues or baseline drifts. The PSICAM is also highly sensitive to small errors in the calibration at wavelengths below 400 nm which might affect the agreement with other instruments at these wavelengths adversely.

The quality of absorption coefficients in the red/NIR region was investigated using a $CuSO_4$ solution. Fig. 3.4 shows good agreement between the spectrophotometer and the PSICAM for absorption coefficients ranging over three orders of magnitude. The dual-beam spectrophotometer has a lower sensitivity due to its short optical pathlengths causing a slight increase in noise for wavelengths shorter than 500 nm where absorption coefficients were very low (occasionally negative). The PSICAM outperformed the spectrophotometer for samples with low absorption due to its longer effective pathlength which makes it well suited for clear oceanic water with low constituent concentrations. The PSICAM did not return negative values even for very low absorption as the standard spectrophotometer does. The noise in PSICAM data increased at wavelengths > 700 nm where measured absorption coefficients are high (> 3 m^{-1}). These high sample absorption coefficients at NIR wavelengths in combination with the high absorption of water itself limits the amount of light available to a critical level and can result in lower quality absorption data.

3.2.2. LWCC system – PSICAM comparison

Two datasets of CDOM absorption spectra (350 – 800 nm) collected with both the LWCC system and the PSICAM were used for a comparison of these two instruments. The first contained 26 spectra measured during the algal culture IOPs experiment (AC-IOPs; Section 2.7.1) in 2014. The second dataset was collected on the UK coastal waters cruise (UKCW; Section 2.8.3) in April 2015 where 58 absorption spectra of natural CDOM were determined.

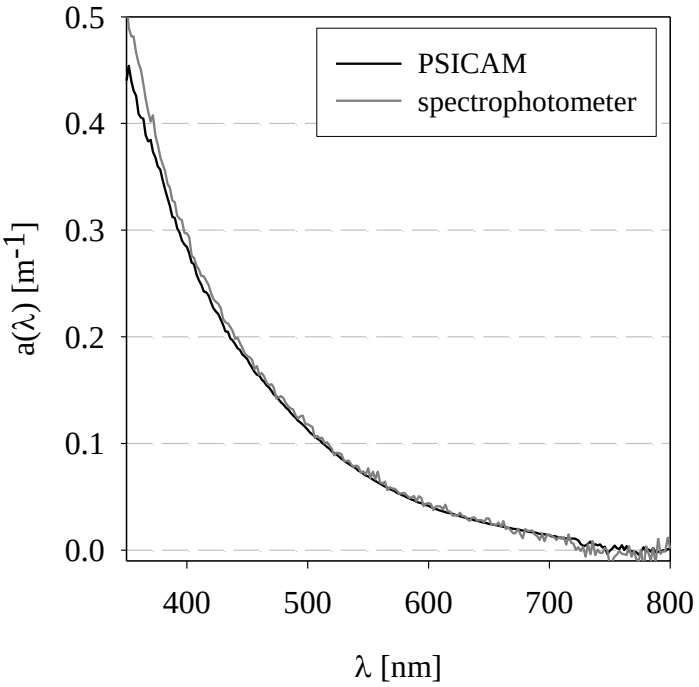

Fig. 3.3 Agreement of humic acid absorption spectre determined with a PSICAM and a spectrophotometer (10 cm cuvette).

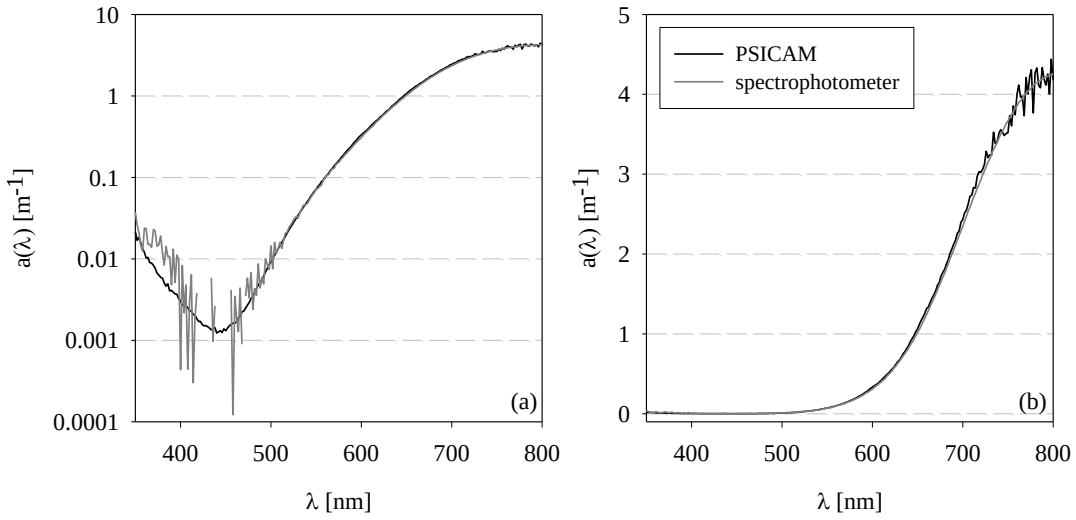

Fig. 3.4 Comparison of absorption coefficients of a $CuSO_4$ solution determined using a dual-beam spectrophotometer (10 cm cuvette) and a PSICAM. $a(\lambda)$ is plotted on (a) a log-scale and negative data are not shown and (b) on a linear scale.

The two methods deviated within 20.2% (Fig. 3.5(a)) and 14.9% (Fig. 3.5(b)) RMedianS%E (Eq. 3.1) for algal culture CDOM and natural CDOM, respectively. Absolute deviation between the LWCC system and PSICAM were of similar magnitude and spectral shape in both datasets. The median absolute deviation was smallest from 450 - 720 nm (< 0.008 m^{-1}) in both cases and increased towards the edges of the spectrum. In general, widest spread in data was observed for low absorption coefficients, i.e. in the NIR. Imperfections in the correction for salinity and temperature effects for both measurement techniques are likely drivers for the increased average deviation of approx. 0.02 m^{-1}, corresponding to a very large relative error for wavelengths longer than 720 nm.

$$\mathrm{RMedianS\%E} = \sqrt{\mathrm{median}\left[\left(\frac{x_{LWCC} - x_{PSICAM}}{x_{PSICAM}} \times 100\right)^2\right]} \quad [\%] \quad [3.1]$$

where x_{LWCC} and x_{PSICAM} are the absorption measured with the LWCC system and PSICAM, respectively.

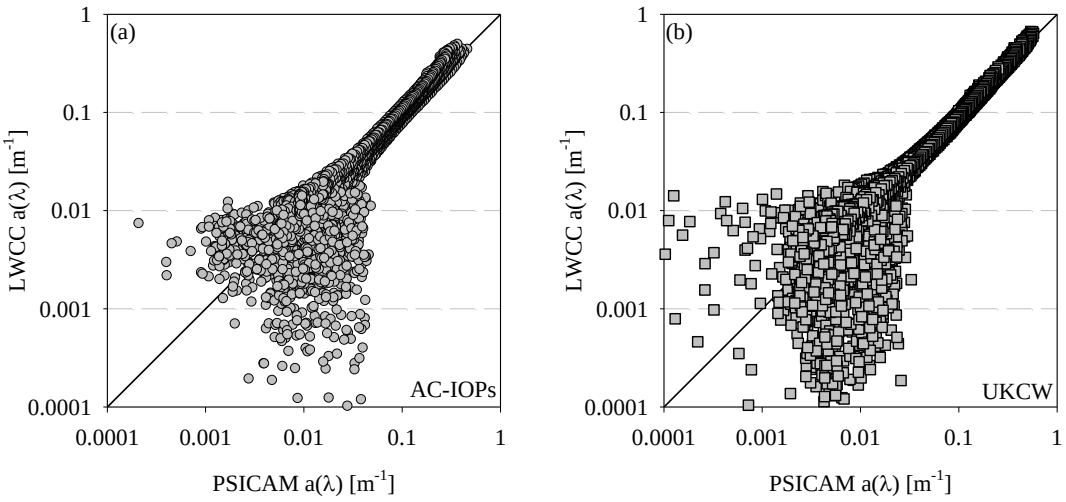

Fig. 3.5 Comparison of CDOM absorption (350 – 800 nm) determined with a LWCC system and a PSICAM (a) as part of the algal culture IOPs experiment (AC-IOPs) and (b) during the UK coastal waters cruise in 2015 (UKCW,).

PSICAM absorption spectra tend to tail off at wavelengths below 400 nm and hence systematically underestimate LWCC absorption in the UV/blue. The absolute magnitude of the difference between absorption coefficients in the UV was reduced by a factor of 3 from 2014 to 2015, corresponding to a reduction from 25% to 10%, and can be attributed to the

improvement of measurement protocols for both methods. For example, during the work on algal culture IOPs in 2014, the applied vacuum was not limited to < 0.2 mbar which potentially generates scattering bubbles in the sample and leads to an increase in LWCC absorption data. Limited availability of PSICAM calibration data for the AC-IOPS dataset (not calibrated daily) is also considered to have a large impact on the agreement between the two instruments as PSICAM absorption coefficients are very sensitive to errors in the reflectivity in the UV (Section 3.4.1).

3.3. Scattering effects in PSICAM measurements

The assessment of adverse scattering effects on PSICAM measurements was following Röttgers *et al.* (2005). The transmission of 4 $BaSO_4$ (98% extra pure, Acros Organics) suspensions, 2 mg L^{-1}, 10 mg L^{-1}, 20 mg L^{-1} and 40 mg L^{-1}, was measured in the dual-beam spectrophotometer and the PSICAM. $BaSO_4$ scatters very efficiently and does not absorb significantly at the concentrations used here. $BaSO_4$ concentrations > 10 mg L^{-1} form milky white, optically dense suspensions.

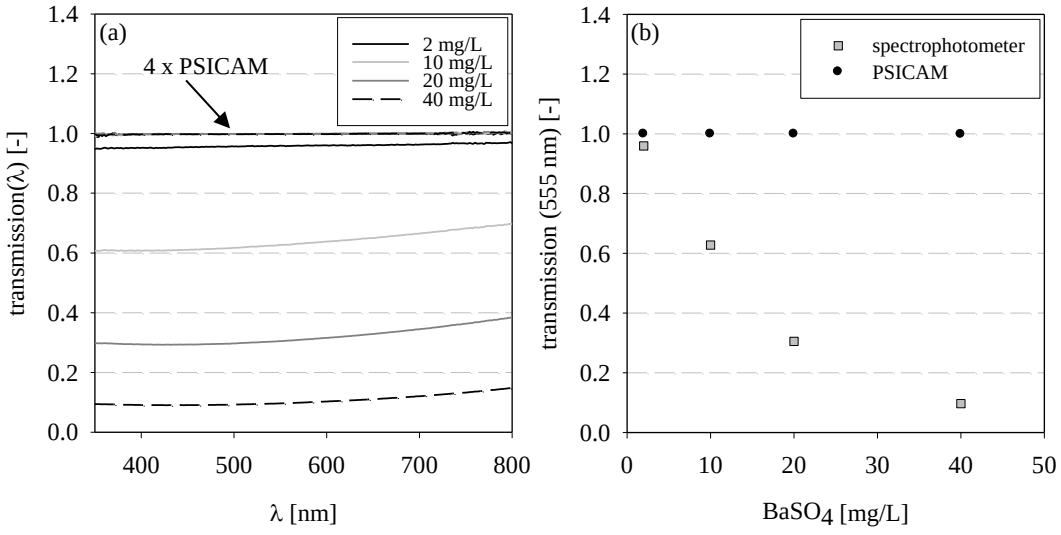

Fig. 3.6 Effect of adding $BaSO_4$ on the transmission measured in a spectrophotometer (10cm cuvette) and in a PSICAM. (a) transmission of 4 different concentrations as function of wavelength. All PSICAM spectra overlay around 1.0. (b) Transmission at 555 nm for different $BaSO_4$ concentrations.

Fig. 3.6(a) shows that the transmission was weakly wavelength dependent and rapidly decreased with concentration for measurements in a spectrophotometer. The transmission at 555 nm measured using a 10 cm cuvette (Fig. 3.6(b)) dropped to 0.1 for the highest concentration while the PSICAM transmission was unaffected by the presence of scattering material in the sample. Even for low concentrations (2 mg L^{-1}) which do not exhibit visible scattering, spectrophotometer measurements underestimate the transmission by ~ 5%. This highlights the limitations of cuvette measurements for unfiltered marine samples which always contain some scattering material.

3.4. Assessment of PSICAM measurement uncertainties

Having demonstrated the accuracy of PSICAM absorption data and its insensitivity to the presence of scattering material, this section will assess measurement precision, i.e. the reproducibility, and uncertainties of the method.

3.4.1. Precision of PSICAM determinations

The standard deviation of triplicates is a measure of the reproducibility or precision of a measurement. In order to quantify the precision of PSICAM measurements, the standard deviation of all samples, i.e. total absorption and CDOM absorption, collected on the UKCW cruise in April 2015 were quantified (Fig. 3.7).

Looking at the mean standard deviation spectrally, total absorption measurements on average exhibited a 2 fold higher values than CDOM absorption measurements due to natural variability in subsamples. The variability is less significant when samples only contain very small particles as observed during the AC-IOPs experiments, where measurements of small cell algae cultures where significantly more stable than of species with larger cells (data not shown). Small cells are more likely to stay in suspension and be distributed homogeneously in the sample and, hence, result in less variability in subsamples. Standard deviations are typically lowest between 450 – 700 nm and increased towards both ends of the spectrum. Increased standard deviations at both ends of the spectrum are a result of a combination of different effects (Section 3.2.1). 93.7% of all standard deviations calculated from the triplicates, of total absorption measurements, were < 0.01 m^{-1} at wavelengths between 350 – 800 nm (Fig. 3.7(a)). For CDOM absorption measurements this level of precision was

achieved for 96.6% of all absorption determinations (Fig. 3.7(b)), and 84.1% were < 0.005 m^{-1}.

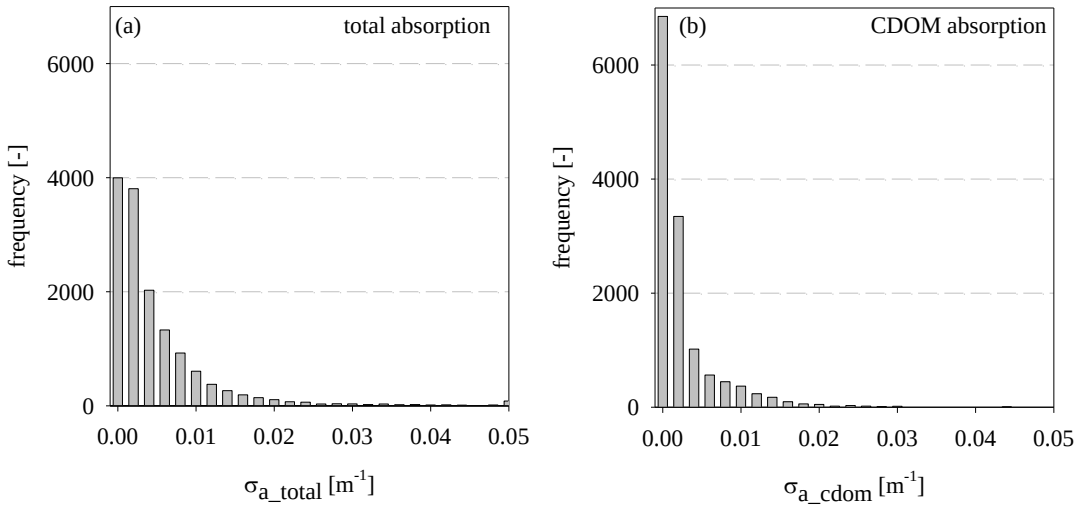

Fig. 3.7 Distribution of standard deviations calculated from triplicates of (a) total absorption and (b) CDOM absorption determinations made on the UKCW cruise in April 2015. Data shown include absorption coefficients from 350 – 800 nm

Absorption measurements of the same humic acid solution made with three different instruments, the dual-beam spectrophotometer with 10 cm cuvette, a LWCC system and the PSICAM, showed that PSICAM measurements have a significantly higher precision and reproducibility than the other two systems. Mean absorption spectra are in agreement within their uncertainties from 400 – 800 nm across all instruments (Fig. 3.8). PSICAM absorption coefficients showed the typical systematic underestimation at wavelengths below 400 nm. The standard deviations of these triplicates, however, varied widely between the different techniques. Variability in PSICAM absorption measurements is up to one order of magnitude smaller than for determinations with the spectrophotometer and LWCC system. The standard deviation for this measurement was < 0.01 m^{-1} from 370 – 800 nm. This level of precision was not achieved with the other methods. For wavelengths between 480 – 700 nm, standard deviations were significantly lower, less than ± 0.004 m^{-1}. The standard deviation of the LWCC measurements was approximately constant with wavelength, around ± 0.013 m^{-1}. Observations showed that measurement uncertainties originate predominantly from offsets caused by a high sensitivity to bubbles in the system and the amount of pressure applied during the injection of the sample which is masking wavelength dependent effects. Standard

spectrophotometer measurements had largest associated uncertainties. Standard deviations had a minimum of ± 0.013 m^{-1} for wavelengths in the green and increased towards the edges of the spectrum with a maximum > 0.04 m^{-1}. The high variability in spectrophotometer measurements is due to its low sensitivity caused by short pathlengths and incomplete correction of temperature effects and potential drifts of the baseline varying during a sequence.

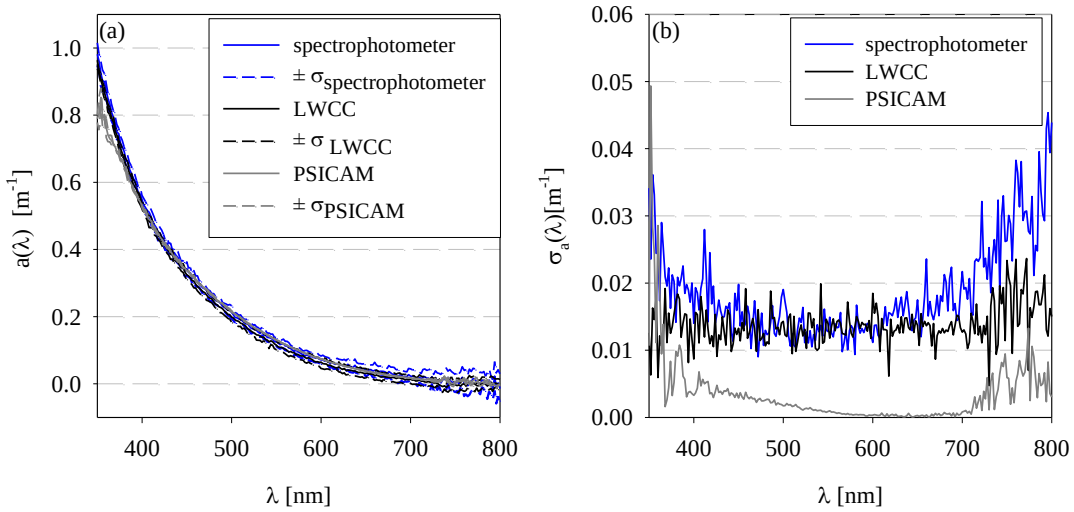

Fig. 3.8 Precision of triplicate determination of humic acid absorption coefficients in the PSICAM, the LWCC system and a dual-beam spectrophotometer equipped with 10 cm cuvettes. (a) Averaged absorption spectrum (solid line) and corresponding standard deviations (dashed lines). (b) Standard deviations for the three different instruments as a function of wavelength, λ.

3.4.2. Cross-comparison with another PSICAM

During the UKCW cruise in spring 2015, 63 total absorption and 59 CDOM absorption spectra were determined using two independent PSICAM measurements – one by the University of Strathclyde (Strath PSICAM) and a second by the Remote Sensing Group at the Helmholtz-Zentrum Geesthacht (HZG PSICAM). Samples were taken from the same Niskin bottle but sample filtration and data processing were done separately by the two groups using their respective filtration set-ups and protocols. Comparison of these measurements allows quantification of the overall uncertainties in the method including the filtration process for CDOM. Absorption coefficients from 362 – 726 nm were compared and relevant statistical parameters calculated. To avoid artefacts due to differences in the

calibration solution, 5 L of a Nigrosine solution, were prepared every morning and two fresh sub-samples were used for each calibration of the two different PSICAMs (3-5 times a day). The required corresponding measurement of Nigrosine absorption spectra was also made independently by the two groups, using long pathlength LWCC systems.

Total absorption data measured with the two instruments were a close match with an overall RMS%E (Eq. 3.2) of 10.6%. The HZG PSICAM, however, returned slightly lower absorption coefficients than the Strath PSICAM (Fig. 3.9(a)). The absolute average deviation (difference between HZG and Strath absorption data) was less than -0.017 m^{-1} across the spectrum (negative indicating the Strath PSICAM returning higher values). Maximum absolute deviations of 0.1 – 0.4 m^{-1} were observed at 362 nm for sediment-loaded samples in the Bristol Channel where very high absorption coefficients (a(362 nm) = 2.2 – 4.6 m^{-1}) were observed. The average relative deviation between the two instruments was spectrally flat and < 10% for wavelengths shorter 650 nm. The relative deviation was largest in the NIR (up to 60% at 726 nm), where the sample absorption is very low and measurement uncertainties have a relatively large effect.

$$\mathrm{RMS\%E}=\sqrt{\frac{1}{n}\sum_{1}^{n}\left(\frac{x_{HZG}-x_{Strath}}{x_{Strath}}\times 100\right)^{2}} \qquad [\%] \qquad [3.2]$$

where x_{HZG} and x_{STrath} are the absorption measured with the HZG PSICAM system and the Strath PSICAM, respectively.

Both groups determined their own temperature and salinity correction coefficients for their respective PSICAMs. In both cases, NaCl solutions were used to derive salinity correction coefficients. Absorption spectra measured with the Strath PSICAM showed a residual artefact (overestimation) in the presence of salt which accounts for most of the deviation between the two instruments in the NIR. The observed overestimation might originate from unaccounted conversion issues between salinity and NaCl concentrations or changes in the reflectivity of the PSICAM cavity due to the different refractive indices of Nigrosine and saline solutions. Residual discrepancies between the two PSICAM datasets presumably originated from differences in processing protocols which could not be identified despite several discussions had.

The comparison of CDOM absorption data showed a similar trend (overall RMS%E = 15.1%) and the HZG PSICAM tended to return lower absorption coefficients than the Strath

PSICAM (Fig. 3.9(b)). Average absolute deviations in CDOM measurements were typically less than -0.009 m^{-1} from 400 – 726 nm, but could reach a maximum of -0.018 m^{-1}. Due to lower overall absorption of CDOM samples, relative deviations were higher compared to total absorption values. The average relative difference between the two methods varied between -4.5% and -9% for wavelengths shorter than 595 nm, with an RMS%E < 6.3%. At wavelengths > 600 nm, CDOM absorption is extremely low and residual artefacts even after correction due to the salinity and temperature dependence of water have a large effect.

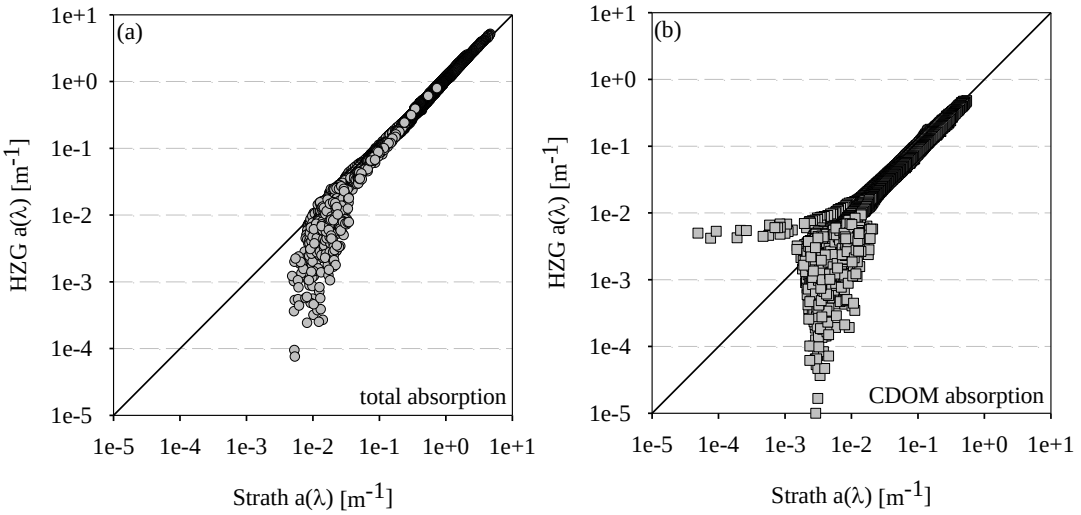

Fig. 3.9 Comparison of measurements with two independent PSICAMs operated by 2 different groups (HZG and Strathclyde). Spectral total absorption (a) and CDOM absorption (b) data (362 – 726 nm) were measured on the UKWC cruise and are shown on a log-log scale.

3.5. Stability of the PSICAM calibration

In order to obtain accurate absorption coefficients, the reflectivity of the cavity walls, ρ, has to be determined with a high accuracy during calibration. Although in theory ρ is only a property of the cavity walls, in practice it is a more complex representation of multiple aspects of the PSICAM design. It is dependent on the illumination as well as the dimensions and state of the cavity.

During the calibration, ρ is effectively a tuning variable used to match PSICAM data with absorption coefficients of the same Nigrosine solution measured with another instrument, modelling PSICAM performance. According to Eq. 2.8, ρ is a function of the radii of the

cavity and light bulb, r and r_0, the absorption coefficient of the calibration solution, a_A and the transmission determined during the calibration, T_{AB}, and will, therefore, be sensitive to uncertainties in these parameters. The dimensions of the cavity, r and r_0, are fixed and variability in the calibration, hence, originates from the uncertainties in the measurements of a_A and T_{AB} only. The state of the cavity and the light bulb potentially change within a short time period due to contamination, ageing of surfaces or varying amounts of water inside the pores of the cavity material. The PSICAM should be calibrated frequently (during heavy use every couple of hours) and at least in triplicate every day. On the UKCW, this was achieved by obtaining a reflectivity spectrum before each station, up to 4 – 5 times a day which were averaged to get a robust daily estimate.

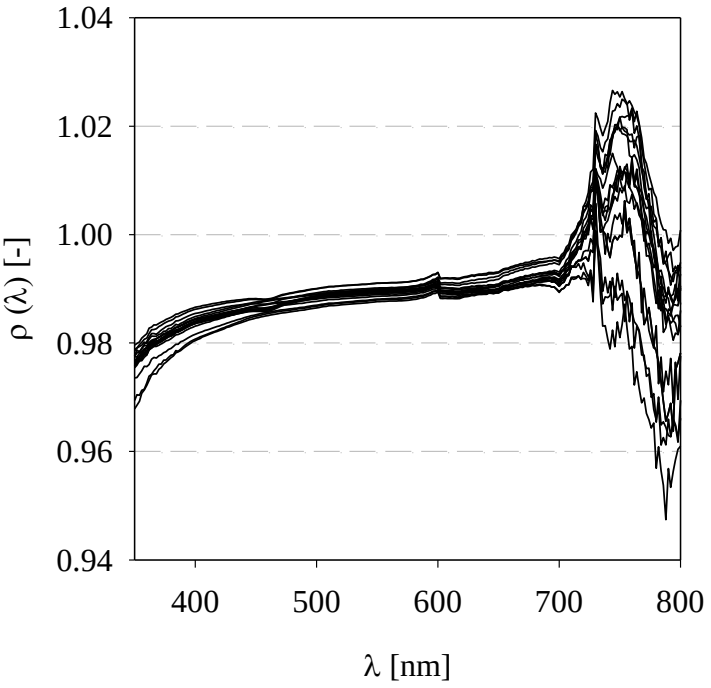

Fig. 3.10 Daily averages of reflectivity spectra obtained for calibration of the PSICAM during the UKCW cruise in April 2015. Two different cavities were used during this cruise.

Fig. 3.10 shows all daily averages derived on the 3 weeks UKWC cruise in April 2015. Observed ρ values were close to manufacturer values for the cavity material, between 97 – 99% from 350 – 700 nm and varied within 0.6% (95% prediction intervals) over the course of 3 weeks. For wavelengths > 700 nm, the reflectivity varied more strongly between 0.95 and 1.03. 95% all calibrations obtained in the NIR were within ± 3.6%. Although a

reflectivity greater than 1.0 is unphysical, absorption coefficients calculated with these reflectivity values showed very good agreement with LWCC data (Fig. 3.5). It is therefore more accurate to consider ρ as a parameter to tune the model which is used to calculate PSICAM absorption coefficients, where $\rho > 1.0$ is compensating for limitations in this model.

This variability is mainly driven by the high sensitivity of ρ to uncertainties in the Nigrosine absorption coefficient, a_A, determined with a spectrophotometer or long-pathlength system (section 3.4.2). The uncertainties in a_A are typically largest for wavelengths longer than 700 nm (Fig. 3.8). Fluorescence by Nigrosine (additional measurements showed emission peaks around 650 - 670 nm), although very small, might also affect the determination of ρ because fluorescence effects might impact the two measurement systems to varying degrees.

3.6. Sensitivity analysis

Having established the performance of PSICAM absorption measurements in terms of precision and accuracy, this section will discuss the influence of uncertainties in all experimentally determined parameters: (1) the sensitivity of ρ to uncertainties in the respective input parameters, a_A and T_{AB} and (2) the sensitivity of a_S to uncertainties in ρ and T_{SR}.

During the course of the analysis, the impact of measurement uncertainties on ρ and a_S was found to be strongly dependent on the ratio of sample absorption to reference absorption. Results shown here are therefore presented dependent on the ratio a_{sample}/a_{ref} (i.e. a_A/a_B and a_S/a_R). a_{sample}/a_{ref} is wavelength dependent: a_{sample}/a_{ref} ratios close to 1.0 occur in the NIR and exhibit a maximum of about 100 for wavelengths < 550 nm (Fig. 1.2). A summary of all parameters and symbols used in this section is given in Table 3.1.

Table 3.1 Variables used for calculation of PSICAM reflectivity and sample absorption coefficients and their associated uncertainties as relevant for sensitivity analysis performed here.

symbol	variable	derivation and associated uncertainties
a_A	absorption coefficient of calibration solution, Nigrosine	spectrophotometric determination with associated measurement uncertainties
a_B	absorption coefficient of reference (pure water) during calibration	literature value, associated uncertainties assumed to cancel out
a_R	absorption coefficient of reference (pure water) during absorption measurement	literature value, associated uncertainties assumed to cancel out
a_{ref}	absorption coefficient of reference in both calibration and measurement	$a_{ref} = a_B = a_R$
a_S	sample absorption coefficient	determined in PSICAM, sensitive to uncertainties in r, r_0, T_{SR}, a_R, ρ
a_{sample}	absorption coefficient of sample in both calibration and measurement	$a_{sample} = a_A = a_S$
I_A	light intensity inside PSICAM cavity when filled with calibration solution, Nigrosine	measurement uncertainties
I_B	light intensity inside PSICAM cavity when filled with reference (pure water) during calibration	measurement uncertainties
I_R	light intensity inside PSICAM cavity when filled with reference (pure water) during absorption measurement	measurement uncertainties
I_S	light intensity inside PSICAM cavity when filled with sample	measurement uncertainties
ρ	reflectivity determined during PSICAM calibration	calculated using/sensitive to uncertainties in r, r_0, T_{AB}, a_A, a_B
r	inner radius of PSICAM cavity	constant, associated uncertainties assumed to cancel out
r_s	radius of PSICAM light bulb	constant, associated uncertainties assumed to cancel out
r_0	distance from light source to cavity wall	$r_0 = r - r_s$, associated uncertainties assumed to cancel out
T_{AB}	transmission measured in PSICAM during calibration	$T_{AB} = I_A/I_B$ and sensitive to associated uncertainties (Eq. 3.1)
T_{SR}	transmission measured in PSICAM during absorption measurement	$T_{SR} = I_S/I_R$ and sensitive to associated uncertainties (Eq. 3.1)

3.6.1. Previous work

Leathers *et al.* (2000) used Monte Carlo simulations to investigate the sensitivity of PSICAM absorption coefficients, a_S, to errors in the parameters, r, r_0, T_{AB}, a_A, as well as the transmission determined during a sample measurement, T_{SR}, and the absorption coefficients of the references (in our case purified water) used during calibration and absorption measurements, a_B and a_R. Their analysis suggests determining ρ by measuring the transmission of two solutions, A and B, with known absorption coefficients, a_A and a_B. This significantly reduces the overall uncertainty in a_S because the effect of error in r and r_0, cancels out and a_S is relatively insensitive to errors in a_B and a_R, when $a_B = a_R$. This approach has been applied in the calibration for this work.

Lerebourg *et al.* (2002) focused on the calculation of absorption coefficients and the sensitivity of a_S to the parameters r, T_{SR}, ρ and a_R, showing that a 10% error in a_S can be caused by either a 5% error in a_R, a 3% error in r or a < 1 % error in ρ, all of which highlights the importance of accurate determination of the calibration solution.

In order to better understand the impact of combined error sources, a new sensitivity analysis was performed here looking at both the determination of ρ and a_S. The same reference absorption (pure water) was used during the calibration and the absorption determination, i.e. $a_B = a_R = a_{ref}$. The reference absorption coefficients for pure water were taken from the literature (Section 1.4.1) and are assumed to introduce no random uncertainty to the analysis. This implies that the effects of uncertainties originating from imperfections in the water purification system are negligible. Uncertainties in r, r_0 and a_{ref} were not considered in the analysis presented here because they were shown to have a relatively insignificant effect on final absorption coefficients when ρ is obtained experimentally (Leathers *et al.* 2000).

3.6.2. Uncertainties in PSICAM transmission measurements

Uncertainties in the measurement of the transmission inside a PSICAM, ΔT_{xy} (either T_{AB} or T_{SR}), potentially originate from fluctuations in the illumination, changes in the detector's sensitivity (with temperature), contamination of the cavity or changes in the sample due to contamination, temperature changes or natural variability. Light source and detector were found to be very stable and changes in the cavity or sample were considered main drivers for

the magnitude of ΔT_{xy}. The standard deviation of replicate measurements of the transmission, σT_{xy} , can be used to get estimates of ΔT_{xy}.

As T_{xy} is the ratio of two measured intensities, I_x and I_y (either I_A and I_B for the calibration or I_S and I_R for the absorption determination), measured when the cavity is filled with two different solutions, σT_{xy}, is derived from the uncertainties in the two intensity measurements, σI_x and σI_y using

$$\frac{\sigma T_{xy}}{T_{xy}} = \sqrt{\left(\frac{\sigma I_x}{I_x}\right)^2 + \left(\frac{\sigma I_y}{I_y}\right)^2} \qquad [-] \qquad [3.3]$$

where σT_{xy} is the standard deviation in the transmission determination of a solution, X, against a reference solution, Y. For a calibration determination, X is the calibration solution A (Nigrosine) whereas for an absorption determination, X is the sample S. The reference Y represents the reference solutions B and R (both purified water), respectively.

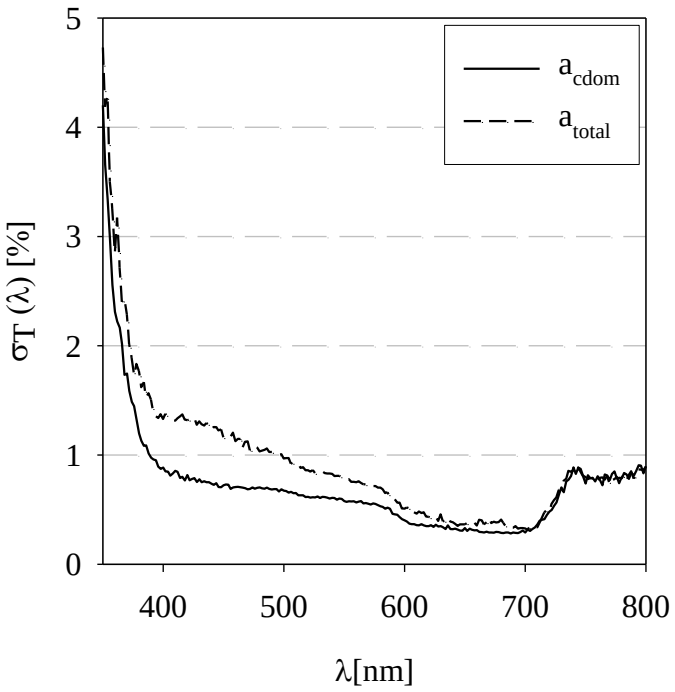

Fig. 3.11 Median standard deviations of triplicate transmission determinations for all total absorption and CDOM absorption measurements made during the UKCW cruise as a function of wavelength.

According to Eq. 3.3, σT_{xy} should be considered as the relative error of the transmission, T_{xy}. ΔT_{xy} was derived from median uncertainties in transmission determination of all total absorption and CDOM absorption measurements made on the UKCW cruise. Values were found to be relatively independent from the strength of the absorption signal, i.e. the magnitude of the transmission. The median σT_{xy} for this dataset was spectrally flat and < 2% from 380 – 800 nm with a maximum of 4% at 350 nm (Fig. 3.11). The uncertainty in the transmission and its variability increased towards the UV (Section 3.2.1).

3.6.3. Sensitivity of ρ to uncertainties in T_{AB} and a_A

The accurate determination of ρ is affected by the accuracy with which a_A can be determined in either a LWCC system or a dual-beam spectrophotometer. Standard deviations of the triplicate determination of a_A provided a measure of the uncertainties, Δa_A. Fig. 3.8(b) shows that both LWCC and the dual-beam spectrophotometer are able to obtain absorption coefficients of coloured solutions with typical average precision of ± 0.015 m^{-1}. Maximum uncertainties of ± 0.05 m^{-1} were observed in dual-beam spectrophotometer measurements. Both average and maximum standard deviations were used in the calculation of ρ (Eq. 2.8) in order to assess their effect on the accuracy of the calibration. Fig. 3.12 shows that Δa_A affects ρ strongest for a_{sample}/a_{ref} close to 1.0, corresponding to the NIR region, where it can result in a maximum $\Delta\rho$ of up to 9% for Δa_A = 0.05 m^{-1}. This result is in agreement with the observed large variability in ρ in the NIR (Fig. 3.10). The average Δa_A of 0.015 m^{-1} propagates into a maximum $\Delta\rho$ of 2.5%. For most of the spectrum, $a_{sample}/a_{ref} > 5$, $\Delta\rho$ is relatively insensitive (≤ 0.15%) to uncertainties in the Nigrosine absorption measurement.

In order to assess the impact of uncertainties associated with T_{AB} on the determination of ρ, an initial value of T_{AB} was calculated assuming ρ = 0.98 (Eq. 2.7). Robust estimates for these uncertainties, ΔT_{AB}, were derived from the analysis of standard deviations in UKCW transmission measurements (Section 3.6.2). ρ was calculated using Eq. 2.8 and ($T_{AB} \pm \Delta T_{AB}$) with varying values of ΔT_{AB} and finally compared to the initial value of 0.98. The sensitivity of the reflectivity to ΔT_{AB} shows a similar trend to Δa_A with a high sensitivity in the NIR (low a_A/a_{ref}) but very little effect on $\Delta\rho$ for most of the spectrum (Fig. 3.13). Average values for ΔT_{AB} resulted in $\Delta\rho$ within ± 2.5%, but maximum errors were found to be as large as + 5% and – 17%. The impact on $\Delta\rho$, however, is larger for positive errors in the transmission than for negative, especially in the NIR when ($T_{AB} + \Delta T_{AB}$) approaches 1.0, the boundary for modelling ρ.

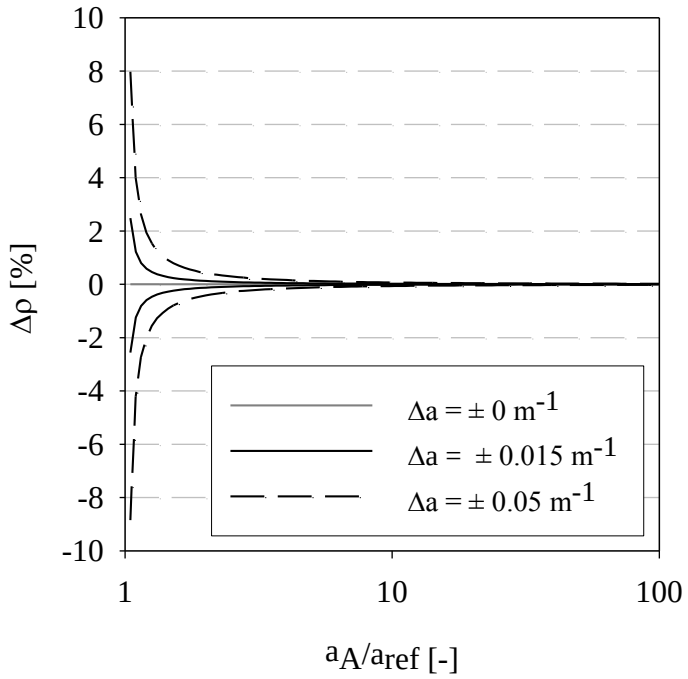

Fig. 3.12 The sensitivity of ρ to uncertainties in the determination of the Nigrosine absorption coefficient, a_A. Data show the effect of absolute errors in a_A on relative errors in ρ depending on the ratio of a_A/a_{ref}.

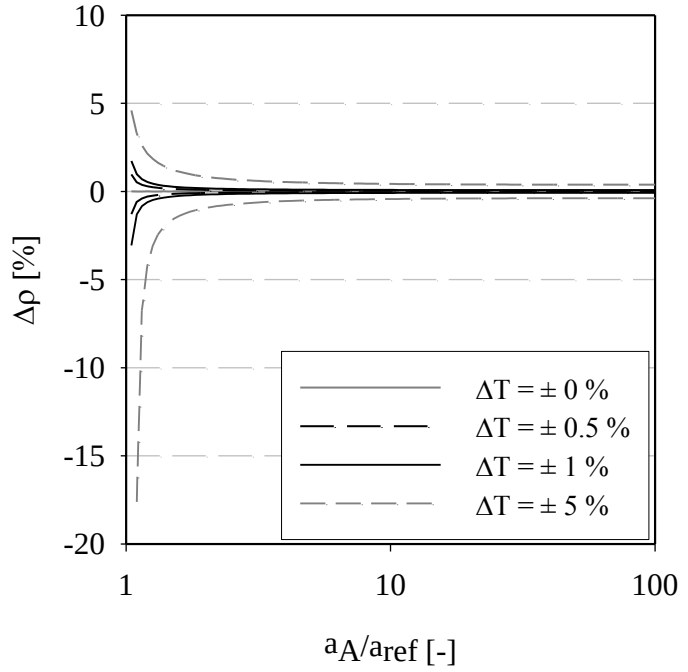

Fig. 3.13 The effect of relative errors in the PSICAM transmission measurement, ΔT_{AB}, on the calculation of ρ depending on the ratio $a_A/a_{ref.}$

3.6.4. Sensitivity of a_S to uncertainties in T_{SR} and ρ

Calculation of a_S is sensitive to measurement uncertainties associated with both input parameters, ρ, and the measurement of the sample transmission, T_{SR}. The sensitivity analysis for ρ using realistic estimates of uncertainties in a_A and T_{AB} has shown changes in ρ of up to 10%. Observations of ρ in the field, however, showed significantly lower variation between 0.3% and 3.6% (Fig. 3.10) and were therefore used as realistic estimates for $\Delta\rho$.

Results showed that the determination of a_S is highly sensitive to uncertainties in ρ (Fig. 3.14). A maximum of almost 30% change in a_S was found for $\Delta\rho$ = 3.5% and a_{sample}/a_{ref} of approx. 5. This analysis supports the work by Lerebourg *et al.* (2002) who also observed a factor of 10 multiplier from uncertainties in ρ into uncertainties in a_S. Fig. 3.14, however, also shows very little sensitivity of a_S to uncertainties in ρ for a_{sample}/a_{ref} close to 1.0, i.e. the NIR. This explains the good accuracy of PSICAM absorption coefficients in the NIR despite large observed variability in NIR ρ.

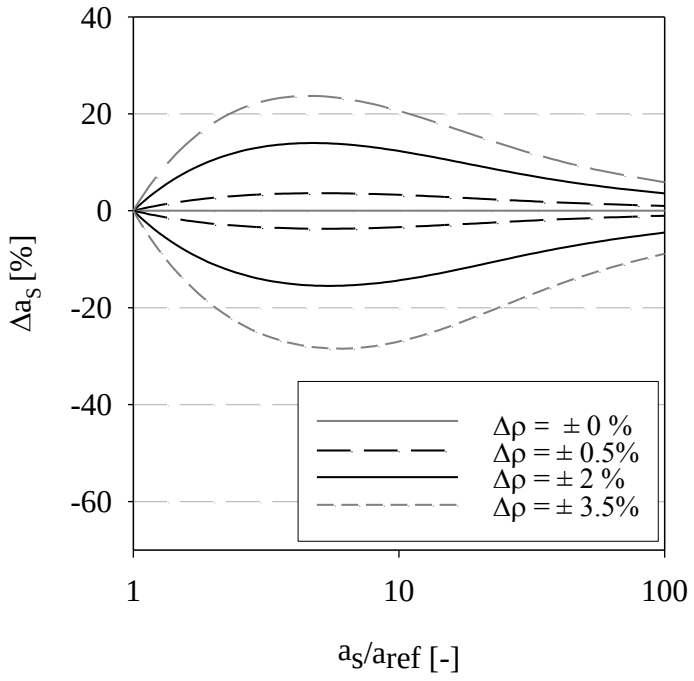

Fig. 3.14 Sensitivity of PSICAM absorption coefficients, a_S, to relative uncertainties in the determination of ρ as a function of a_S/a_{ref}.

Fig. 3.15 shows that a_S is affected by up to ± 3% for typically observed uncertainties in PSICAM transmission measurements, ΔT_{SR}, and we can conclude that the sensitivity decreases from the NIR to the blue, i.e. as a_{sample}/a_{ref} increases.

This theoretical sensitivity analysis shows that it is crucial to determine the reflectivity accurately because this has the largest impact on the quality of PSICAM absorption coefficients. In contrast to errors in the transmission, errors in the calibration affect the absorption coefficients most strongly in the blue/UV where PSICAM values often perform less well than other absorption techniques. Although it is challenging to determine robust NIR reflectivity values, the relatively large uncertainty in ρ does not strongly affect final absorption data. The largest uncertainties in NIR PSICAM absorption coefficients originated from temperature and salinity effects which were not fully accounted for by simple linear corrections.

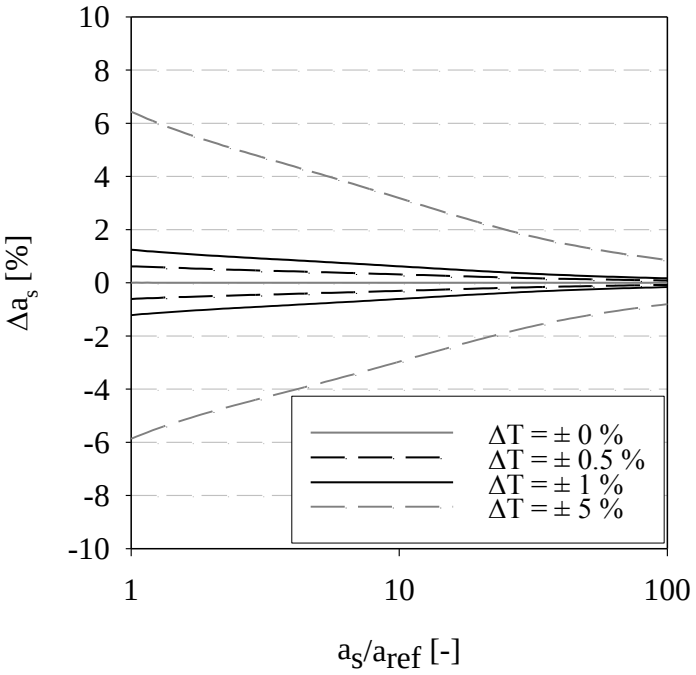

Fig. 3.15 The sensitivity of a_S to uncertainties in the determination of the transmission, T_{SR}. Data show the effect of relative errors ΔT_{SR} depending to the ratio of a_S/a_{ref}.

3.7. Bootstrap uncertainties

Uncertainty estimates for an individual PSICAM absorption measurement have been derived from both comparisons with other instruments and the sensitivity analysis presented here. Combining these new findings, overall uncertainties for PSICAM measurements can be determined. As ρ and a_S are not measured directly but calculated from various parameters, standard deviations of triplicates are not a good representation of overall uncertainties in PSICAM measurements. Standard deviation can provide a measure of precision only but might not capture systematic measurement uncertainties. In order to derive complete uncertainties for each ρ and a_S spectrum, it is necessary to propagate all uncertainties in the respective input parameters into final spectra. The complexity of the relationships for reflectivity and PSICAM absorption coefficients, however, provides a challenge for analytical error propagation. The uncertainties for ρ and a_S are, therefore, estimated using an empirical method, the bootstrap approach.

Bootstrapping is a statistical method to estimate the accuracy of a quantity by repeatedly randomly sampling from an approximating distribution. In this case, distributions of input parameters were approximated and distributions of values for ρ and a_S were computed providing measures for their mean values and overall variability. This method benefits from use of high numbers of repeat samples that enables the calculation of robust statistics.

ρ is dependent on r, r_0, a_A, a_B and T_{AB}. Uncertainties in r, r_0 and a_B were not considered for the bootstrap approach because they do not have associated random measurement uncertainties. Measured ($a_A \pm \sigma a_A$) and ($T_{AB} \pm \sigma T_{AB}$) are assumed to be normally distributed and 1,000 random values for these parameters were generated using a normal distribution based on the mean and standard deviations of a specific triplicate determination. 1,000 reflectivity spectra were calculated and found to be again normally distributed. A mean ρ and a standard deviation $\sigma\rho$ were calculated from this distribution. Once the uncertainty in the reflectivity was determined, the same method was used to derive ($a_S \pm \sigma a_S$) with respect to the input parameters ($T_{SR} \pm \sigma T_{SR}$) and ($\rho \pm \sigma\rho$). For the calculation of a_S, the approach was restricted to 200 samples per distribution due to high requirements regarding computational time.

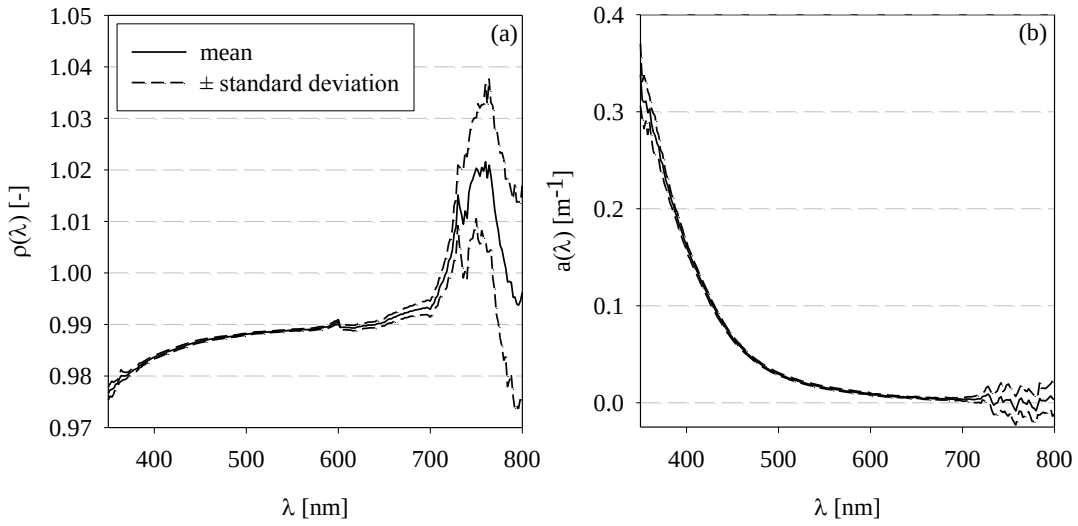

Fig. 3.16 (a) Reflectivity and (b) CDOM absorption spectra with corresponding bootstrap uncertainties. Data were collected at station 16 of the UKCW cruise on 08 April 2015.

Examples for a reflectivity and a CDOM absorption spectrum with corresponding bootstrap uncertainties (standard deviation) collected at station 16 (ST16) of the UKCW cruise showed very small uncertainties for both parameters for most of the spectrum with increasing uncertainties toward the edges of the spectrum (Fig. 3.16). Large uncertainties in NIR ρ, did, however, not propagate into large uncertainties in the corresponding absorption coefficients. This observation is in agreement with findings of the previous sensitivity analysis (Section 2.4.2).

Fig. 3.17 shows a summary of different PSICAM measurement uncertainty estimates determined for UKCW data, including overall accuracy of the method (from cross-comparison of two different PSICAMs), estimates of the overall precision over the course of the cruise (mean standard deviations), and bootstrap uncertainties for an example station, ST16. All three uncertainty estimates were of about the same level, confirming the bootstrap approach as robust method to determine realistic measurement uncertainties. All estimates were lowest in the visible spectrum (typically < 0.005 m^{-1} between 450 – 700 nm) for both total absorption and CDOM absorption determinations and increased towards the edges of the spectrum.

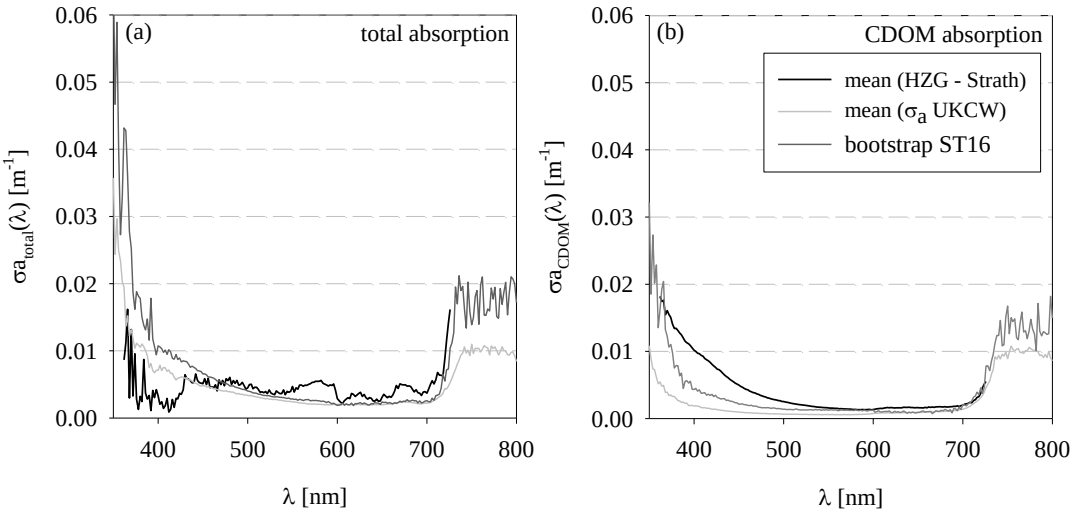

Fig. 3.17 Summary of different uncertainty estimates for PSICAM absorption measurements for (a) total absorption and (b) CDOM absorption determinations made during the UKCW cruise.
Black lines: average spectral deviation between data measured with the HZG and Strath PSICAM; light grey lines: average of all standard deviations determined for Strath PSICAM measurements; dark grey lines: bootstrap uncertainty for an example station (ST16).

3.8. Conclusions

This chapter demonstrated the performance of the PSICAM for absorption determinations of solutions and natural water samples and quantified general measurement uncertainties. The accuracy of PSICAM absorption measurements is at least as good as for determinations with a dual-beam spectrophotometer or a LWCC system except for wavelengths shorter than 400 nm where the PSICAM tends to underestimate other methods. PSICAM data quality in the UV is limited by low signal levels due to low signal levels and limited detector sensitivity. This is problematic in both calibration and absorption determinations. Another source of uncertainty in the UV is the high sensitivity of PSICAM measurements to errors during the calibration, the determination of the reflectivity. The reproducibility of PSICAM measurements is of the same magnitude for CDOM absorption and total absorption coefficients. In comparison to measurements with either LWCC systems or dual-beam spectrophotometers, the precision (standard deviation) of the PSICAM is up to one order of magnitude better due to its long effective pathlength.

The cross-comparison with another PSICAM showed general discrepancies between the instruments of 10 - 15%. The average level of measurement uncertainties in PSICAM

determinations was found to < 0.01 m^{-1} in both CDOM absorption and total absorption coefficients in the visible spectrum. Towards the edges of the spectrum, uncertainties in measured absorption coefficients can, however, be significantly larger. Results showed that bootstrap uncertainties which capture the precision of an individual measurement as well as systematic errors (for example in the calibration), can be used to determine realistic estimates of overall uncertainties in absorption measurements of individual samples. Given the long pathlength and scattering insensitivity of the PSICAM, uncertainty estimates obtained for worst case scenarios point towards a need to carefully re-evaluation measurement uncertainties in other absorption methods. In particular, the accuracy of AC-9 absorption measurements and the performance of commercial ICAM instruments would be of interested as they are accessible to a wide community.

The long pathlength of the PSICAM and its high precision make it well-suited for accurate determination of low absorption coefficients. For untreated samples and samples containing particulate material, the PSICAM outperforms other instruments as it shows insignificant sensitivity to the presence of scattering material. This enables measurements of absolute absorption values that do not rely on scattering corrections which makes the PSICAM ideal for the validation or correction of other established absorption techniques.

4. Improving particulate absorption data using a combination of filter pad and PSICAM measurements

4.1. Introduction

Having established the performance characteristics of the PSICAM, it can now be used to investigate the performance of other absorption measurement methods used to obtain commonly used parameters in oceanographic science. One example is the spectral particulate absorption coefficient which has been routinely measured for many decades using filter pad techniques that are well known to have poorly controlled measurement errors.

4.1.1. Importance of accurate particulate absorption coefficients

All coastal and oceanic waters contain particles which absorb and scatter light. Knowledge on the optical properties of marine particles is therefore important for the parameterisation of RT underwater light field model (Mobley, 1994) and the interpretation of ocean colour remote sensing signals (Lee *et al.*, 2002, Wozniak and Stramski, 2004). Spectral absorption data can be used to gain information on the composition of inorganic and organic material (Chang and Dickey, 1999). Light absorption by phytoplankton cells, in particular, has been of interest in many biological studies as it can yield information on pigment composition and concentration (Hoepffner and Sathyendranath, 1993, Johnsen *et al.*, 1994), as well as the size structure of phytoplankton communities (Ciotti *et al.*, 2002) which can be used to populate biogeochemical models of phytoplankton and photosynthesis (e.g. Behrenfeld and Falkowski, 1997).

The most common method to determine the spectral absorption of light by particles, a_p, is to collect the particulate matter on a glass-fibre filter and measure its absorption in a spectrophotometer. By varying the particle loading, the filter pad technique is sufficiently sensitive even for oligotrophic waters with very low particle concentrations. It also allows the partitioning of particulate absorption into absorption by phytoplankton and non-algal particulate components. Although the PSICAM is well-suited for the determination of absorption by natural water samples (with particles in suspension), there is no established

method to use the PSICAM to measure partitioned algal and non-algal components and it has lower sensitivity than the filter pad technique for oligotrophic samples. There is therefore an ongoing requirement for filter pad absorption measurements and it is essential that major sources of error are identified and appropriate correction methods established.

4.1.2. Sources of uncertainty in filter pad absorption measurements

Great effort has gone into the identification and quantification of measurement uncertainties and subsequent improvement of the filter pad absorption methodology. Error sources include wetness of the filter, different filter types (Mitchell and Kiefer, 1988), filter-to-filter variation even for filters of the same type (Roesler, 1998), storage and freezing of filters (Stramski, 1990, Sosik, 1999), sample loading (Lohrenz, 2000) and improper filtration along with temperature and salinity effects. The major sources of uncertainty, however, are the unknown extent of scattering offsets and limitations in the correction for pathlength amplification (Bricaud and Stramski, 1990, Roesler, 1998, Lohrenz, 2000).

Light loss due to sample scattering can result in a systematic error by introducing a positive offset of unknown magnitude to measured absorption data. In practise, negative offsets due to imperfections in the experimental procedure can also be observed. This is problematic in both filter pad absorption and cuvette measurements. Scattering offset effects are commonly corrected by applying a null-point correction (subtracting the signal measured at wavelengths > 750 nm from the rest of the spectrum) assuming negligible NIR absorption. This assumption, however, does not hold in coastal or mineral-rich waters (Tassan and Ferrari, 2003, Stramski *et al.*, 2007, Röttgers *et al.,* 2014a) and can lead to systematic underestimation of particulate absorption coefficients across the spectrum.

Pathlength amplification occurs when a photon travelling through the sample experiences multiple scattering events within the filter/sample matrix. Pathlength amplification will result in apparent increased sample absorption and data have to be corrected to obtain quantitative absorption coefficients. Measurements are commonly corrected by applying a predetermined pathlength amplification factor, β, which is defined as the ratio of optical to geometrical pathlength. Accurate determination of β is crucial to convert the optical density (OD) of the sample on the filter as measured in a spectrophotometer into quantitative particulate absorption coefficients using

$$a_p(\lambda) = \frac{2.303\ OD_f(\lambda)\ A}{V\ \beta} \qquad [m^{-1}] \quad [4.1]$$

where a_p is the particulate absorption coefficient [m^{-1}] at a given wavelength, λ [nm], OD_f is the optical density of the sample on the filter [-], A is the filter clearance area [m^2], and V is the volume of sample filtered [m^3]. β has typically been derived from experiments with algal cultures and calculated as the ratio between the optical density of a sample on a filter, OD_f, and the optical density of the sample as dilute suspension, OD_s (Bricaud and Stramski, 1990), from which a functional relationship is established and subsequently applied to field samples.

An alternative, widely used approach to correct for pathlength amplification uses a predetermined function, $OD_s=f(OD_f)$, to directly convert OD_f into OD_s. a_p is then calculated using

$$a_p(\lambda) = \frac{2.303\ OD_s(\lambda)\ A}{V} \qquad [m^{-1}] \quad [4.2]$$

This approach was first proposed by Mitchell (1990) who identified a second order polynomial as best descriptor for this relationship. Many studies have since adapted this approach and observed variability in the pathlength amplification correction dependent on phytoplankton species, cell size and shape, OD or wavelength (Mitchell, 1990, Cleveland and Weidemann, 1993, Arbones *et al.*, 1996, Finkel and Irwin, 2001).

4.1.3. OD_f measurement configurations

In order to determine an accurate correction for pathlength amplification, it is necessary to minimise uncertainties in the determination of OD_f and OD_s. Over the past few decades, several geometric configurations for the measurements of OD_f and OD_s have been proposed and tested.

There are currently four different set-ups used to determine OD_f: the transmittance method (T-method), the transmittance-reflectance method (T-R-method) and two measurements inside an integrating sphere (IS-method, QFT-ICAM). Trüper and Yentsch (1967) first suggested measuring the transmittance through a wet glass-fibre filter relative to an empty, wet reference filter. The T-method is by far the simplest and fastest approach and has been used as a standard method for decades (NASA protocols; Mitchell *et al.*, 2003). It has been

suggested, however, that it suffers from limited control over measurement parameters, such as scattering errors, filter-to-filter variation and a high sensitivity to changing wetness of the filter (e.g. Mitchell and Kiefer, 1988, Cleveland and Weidemann, 1993, Arbones *et al.*, 1996, Lohrenz, 2000). As glass-fibre filters effectively act as diffusors, measurements are potentially susceptible to large scattering errors and require null-correction. Scattering errors can be reduced by placing the filters at the entrance of an integrating sphere or close to the detector window.

The transmittance-reflectance method proposed by Tassan and Ferrari (1995, 1998) was introduced to reduce errors when minerogenic material changes the filter backscattering and overcomes some geometric limitations associated with the T-method. It can partially correct for measurement errors due to backscattering losses and filter-to-filter differences. In theory, the T-R method does not require null-point correction but it might be applied in practice to reduce uncertainties originating from imperfections in the measurement set-up. Despites its apparent benefits over the T-method, the T-R-method has not been widely used in the past mainly because of its complex and laborious measurement protocol and the requirement for additional experimental apparatus.

For the IS-method, filter pads are measured with a dual-beam spectrophotometer with scanning monochromatic illumination inside an integrating sphere. In contrast, the QFT-ICAM uses a broadband white light source similar to the PSICAM. Measuring the absorptance of a sample on a filter inside an integrating sphere (IS-method and QFT-ICAM) benefits from a significantly reduced scattering error, high sensitivity and improved signal-to-noise ratio (Maske and Haardt, 1987, Röttgers and Gehnke, 2012, Stramski *et al.*, 2015) but has only been used in a limited number of studies (e.g. Neukermans *et al.*, 2014). Measurements made with a QFT-ICAM or the IS-method do not require null-correction.

It is important to note that mean β-factors vary systematically between different geometric configurations (Röttgers and Gehnke, 2012). This means that there is no universal β-factor and values determined for one measurement geometry cannot be simply ported onto another. All other factors being equal (e.g. availability of relevant equipment), the most favourable method is therefore the one with the smallest associated uncertainty in the determination of β in combination with either a minimal scattering offset or a quantifiable scattering offset correction.

4.1.4. Measuring OD_S

The determination of β requires an associated measurement of OD_s. Accurate determination of OD_s using a cuvette inside a spectrophotometer is extremely difficult and can be significantly affected by scattering losses. Measurement uncertainties can be reduced, but not completely eliminated, when placing the cuvette inside an integrating sphere (Babin and Stramski, 2004). For example there is the potential for such a set-up to also exhibit pathlength amplification effects.

At this time, the most effective measurement set-up uses a PSICAM to determine the absorption of a sample, effectively without any scattering errors, and provides a standard against which filter pad absorption measurements can be validated. PSICAM spectra do not require null-correction, and absorption measured at > 750 nm can be considered to represent real NIR absorption by the sample. It should be noted that PSICAM measurements do not return OD_s but rather a_p directly (from $a_p = a_{total} - a_{CDOM}$). Empirical relationships for $a_p=f(OD_f)$ can be derived, similar to $OD_s=f(OD_f)$, and used to directly convert OD_f into particulate absorption coefficients (Röttgers and Gehnke, 2012, McKee *et al.*, 2014).

4.1.5. Recent developments in filter pad absorption methodology

The accuracy of the filter pad method as quantitative technique has remained controversial at least partly because of the variety of protocols in use. As a result of continuous improvements in instrumentation and methodology, uncertainties in the determination of particulate absorption coefficients were the subject of a number of recent publications. Stramski *et al.* (2015) derived individual functional relationships between OD_s and OD_f for three different geometrical configurations (T-method, T-R method and IS-method) using an extensive dataset of samples with a variety of optically relevant particle characteristics. They recommended the use of a power law function for conversion of OD_f into OD_s for future and historic datasets. The study relied on OD_s measurements from cuvettes placed inside an integrating sphere. Neeley *et al.* (2015) performed a multi-analytical approach to get robust estimates of uncertainties in a_p for selected ocean colour remote sensing wavelengths. They incorporated different experimental and analytical methods to derive a_p and found large variability between the different approaches for different water types.

PSICAM data with minimal scattering error and baseline artefacts enables investigation of the impact of different error sources in filter pad absorption measurements and can help to establish a protocol for the correction for pathlength amplification and scattering offset. To date, three studies have used PSICAM data to assess the performance of traditional pathlength amplification corrections. All of them found linear relationships between particulate absorption coefficients and OD_f for individual samples using the T-method (McKee *et al.*, 2014) and the IS-method (Röttgers and Gehnke, 2012, Röttgers *et al.*, 2016). This suggests that previously observed non-linear relationships might have been affected by errors in the determination of OD_s. Using PSICAM data for validation, McKee *et al.* (2014) established a linear regression scheme to correct filter pad absorption measurements (T-method). The slope of the linear function effectively represents a wavelength-independent, OD-independent β-factor. The intercept enables correction for scattering offsets without assuming zero NIR absorption.

The aim of this chapter is to investigate uncertainties in filter pad absorption techniques in comparison with PSICAM data. Three datasets will be used to quantify the variability in β-factors determined using a linear regression approach including samples with a variety of optical properties. This linear regression method will be compared to historic approaches to correct pathlength amplification and scattering effects in quantitative filter pad absorption measurements. This work will predominantly focus on the T-method as it is still the most commonly used technique and draw comparisons with more involved methods, such as the IS-method and measurements with a QFT-ICAM. The ultimate goal is to establish an optimised methodology for experimentally determining a_p, drawing on the strengths of both PSICAM and filter pad absorption techniques.

4.2. Methods

4.2.1. Datasets

Variability in corrected filter pad absorption measurements was assessed using three datasets: (1) algal cultures (AC-IOPS; Section 2.7), (2) data from the Ligurian Sea (LS; Section 2.8.1) and (3) data from UK coastal waters (UKCW; Section 2.8.3). All datasets contained at least one PSICAM measurement and one filter pad measurement (T-method) for each sample.

For 51 samples collected on the UKCW cruise in 2015, a more extensive dataset is available. Filter pad data measured with the T-method were collected by the University of Strathclyde and 2 additional filter pad absorption measurements were made by the Helmholtz-Zentrum Geesthacht (HZG). The latter were based on the integrating cavity approach: (1) using an integrating sphere with a spectrophotometer (IS) and (2) using the recently developed QFT-ICAM. Two independent sets of PSICAM data (Strath PSICAN and HZG PSICAM) were also available for this subset from the UKCW cruise (Section 2.8.3).

4.2.2. PSICAM measurements

PSICAM particulate absorption coefficients were calculated by subtracting the CDOM absorption from the total absorption coefficient, both measured with a PSICAM (Section 2.4). PSICAM particulate absorption coefficients measured independently with the Strath PSICAM and HZG PSICAM were found to agree within 7.3% RMedianS%E in the visible spectrum (Fig. 4.1). The RMS%E (< 12%; Eq. 3.2) is therefore smaller than for the two initial (total and CDOM, 10.6% and 15.1% respectively) measurements suggesting compensation of systematic errors in both measurements by subtraction. This level of consistency between the two independent datasets is a very encouraging endorsement of the performance of the PSICAM approach and also supports results presented in Chapter 3.

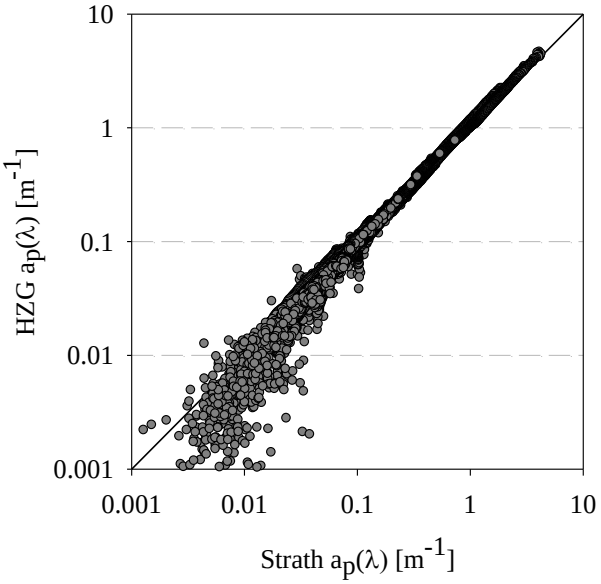

Fig. 4.1 Comparison of particulate absorption spectra (400-700 nm) of all samples collected on the UKCW cruise using the Strath PSICAM and HZG PSICAM.

4.2.3. Filter pad absorption data

OD_f of particulate matter collected on a filter paper was measured in the Shimadzu dual-beam spectrophotometer using the T-method, following the protocol described in Section 2.5. No integrating sphere was used for T-method determinations made in this work. Volumes filtered for the three different datasets ranged from 0.05 L to 5 L. Measurements with the IS-method were performed following the procedure described in Röttgers and Gehnke (2012). All data collected by HZG have been published together with a detailed description of set-up and measurement protocols for the recently introduced QFT-ICAM in Röttgers *et al.* (2016).

4.3. Alternative approaches to corrected filter pad absorption measurements

4.3.1. Historic correction methods

Numerous studies have investigated the performance of quantitative filter pad absorption measurements and acknowledged the susceptibility to errors in the correction for pathlength amplification and scattering offsets. Various factors have been identified to affect the magnitude of pathlength amplification (see above) and proposed correction methods vary strongly. Some studies suggest a dependency of β on OD_f (Maske and Haardt, 1987, Lohrenz, 2000). Bricaud and Stramski (1990) described the relationship between β and OD_f using a power function. Mitchell (1990) proposed the use of a second order polynomial to describe the relationship between OD_f and OD_s. This approach was adopted in many subsequent studies in which alternative coefficients for this model were derived. Stramski *et al.* (2015) recently found that a power law function is the best descriptor for the relationship between OD_f and OD_s, based on extensive laboratory work using samples with a wide range of different optical properties.

Most investigations used algal cultures to determine a function for the correction of pathlength amplification which can then be applied to field samples (Tassan and Ferrari, 1995, Arbones *et al.*, 1996, Roesler, 1998, Finkel and Irwin, 2001). Some studies suggested that a single correction for pathlength amplification might be sufficient if its determination is based on a large number of samples with different particle characteristics (Cleveland and Weidemann, 1993, Roesler, 1998, Stramski *et al.*, 2015). Others, however, point towards a potential dependency on particle characteristics or phytoplankton species, suggesting the

selection of an inappropriate correction for pathlength amplification could result in systematic errors when applied to field samples. So far, no consensus on an appropriate method has been achieved. An overview over the different approaches used to correct filter pad absorption measurements is given in Table 4.1.

Table 4.1 Summary of published pathlength amplification correction as functional relationships $OD_s = f(OD_f)$ and scattering offset corrections for the T-method.

reference	pathlength amplification correction	null-correction	samples type
Stramski *et al.* (2015)	$OD_s = 0.679 OD_f^{1.2804}$	at 750 nm	artificial samples
Stramska *et al.* (2003)	$OD_s = 0.33\ OD_f + 0.983\ OD_f^2$	at 750 nm	field samples
Finkel and Irwin (2001)	$OD_s = 0.446\ OD_f + 0.122\ OD_f^2$	-	
Roesler (1998)	$OD_s = 1/2\ OD_f$	wavelength dependent scattering from AC-9	field samples, cultures
Nelson *et al.* (1998)	species specific	at 750 nm	cultures
Allali *et al.* (1997)	$OD_s = 0.264\ OD_f + 0.322\ OD_f^2$	at 750 nm	field samples
Arbones *et al.* (1996)	$OD_s = 0.38\ OD_f + 0.42\ OD_f^2$	at 750 nm	field samples, cultures
Tassan and Ferrari (1995)	$OD_s = 0.406\ OD_f + 0.519\ OD_f^2$	at 750 nm	cultures
Moore *et al.* (1995)	species specific		cultures
Cleveland and Weidemann (1993)	$OD_s = 0.378\ OD_f + 0.523\ OD_f^2$	at 750 nm	cultures
Hoepffner and Sathyendranath (1992)	$OD_s = 0.31\ OD_f + 0.57\ OD_f^2$	-	cultures
Bricaud and Stramski (1990)	$OD_s = 1/1.63\ OD_f\ (\lambda)^{-1.22}$	empirical relationship	field samples, cultures
Mitchell (1990)	$OD_s = 0.392\ OD_f + 0.655\ OD_f^2$	at 750 nm	cultures

4.3.2. Linear regression correction

Few studies investigating pathlength amplification in filter pad absorption measurements have had access to PSICAM data for validation. Röttgers and Gehnke (2012) studied the variability in β for filter pad measurements using the T, T-R and IS method. For low OD (< 0.4 for the T-method and < 0.1 for the integrating sphere methods), they observed linear relationships between OD_f and a_p for all configurations which showed no dependency on wavelength or OD. Their results suggest that availability of PSICAM data is highly advantageous as it enables performance of sample-by-sample correction and cross-validation.

McKee *et al.* (2014) introduced a regression based approach to correct filter pad absorption measurements made for the determination of chlorophyll-specific absorption coefficients using the T-method. Their analysis also showed linear relationships between PSICAM absorption and uncorrected filter pad absorption coefficients. Fig. 4.2 shows the different stages of the linear regression filter pad absorption correction for two samples. In a first step, the uncorrected filter pad absorption coefficient, a_u, is calculated using Eq. 4.1 and β = 1.0 (Fig. 4.2, (a) and (d)). a_u is plotted against corresponding PSICAM particulate absorption coefficients (Fig. 4.2, (b) and (e)) and a linear function is fitted through the data, returning a slope, i.e. the pathlength amplification correction factor, β, and an intercept, i [m^{-1}], which can be used to correct for scattering offsets without assuming zero NIR absorption. Regressions were limited to the linear range of the data (deviations from linearity as shown in Fig. 4.2 (e) are discussed in Section 4.2.3). a_u can then be converted into quantitative filter pad absorption coefficients, a_p, using Eq. 4.3 (Fig. 4.2, (c) and (f)).

$$a_p(\lambda) = \frac{a_u(\lambda) - i}{\beta} \qquad [m^{-1}] \qquad [4.3]$$

Röttgers *et al.* (2016) recently introduced a field instrument to determine the OD of a sample collected on a filter pad, the QFT-ICAM. They analysed the performance of this new instrument in comparison to the IS-method used in Röttgers and Gehnke (2012) and estimated a mean β-factor for both methods. They found comparable mean β values for the different techniques, generally 2 fold higher than for the T-method, but observed much lower variability in β for the determinations with the QFT-ICAM.

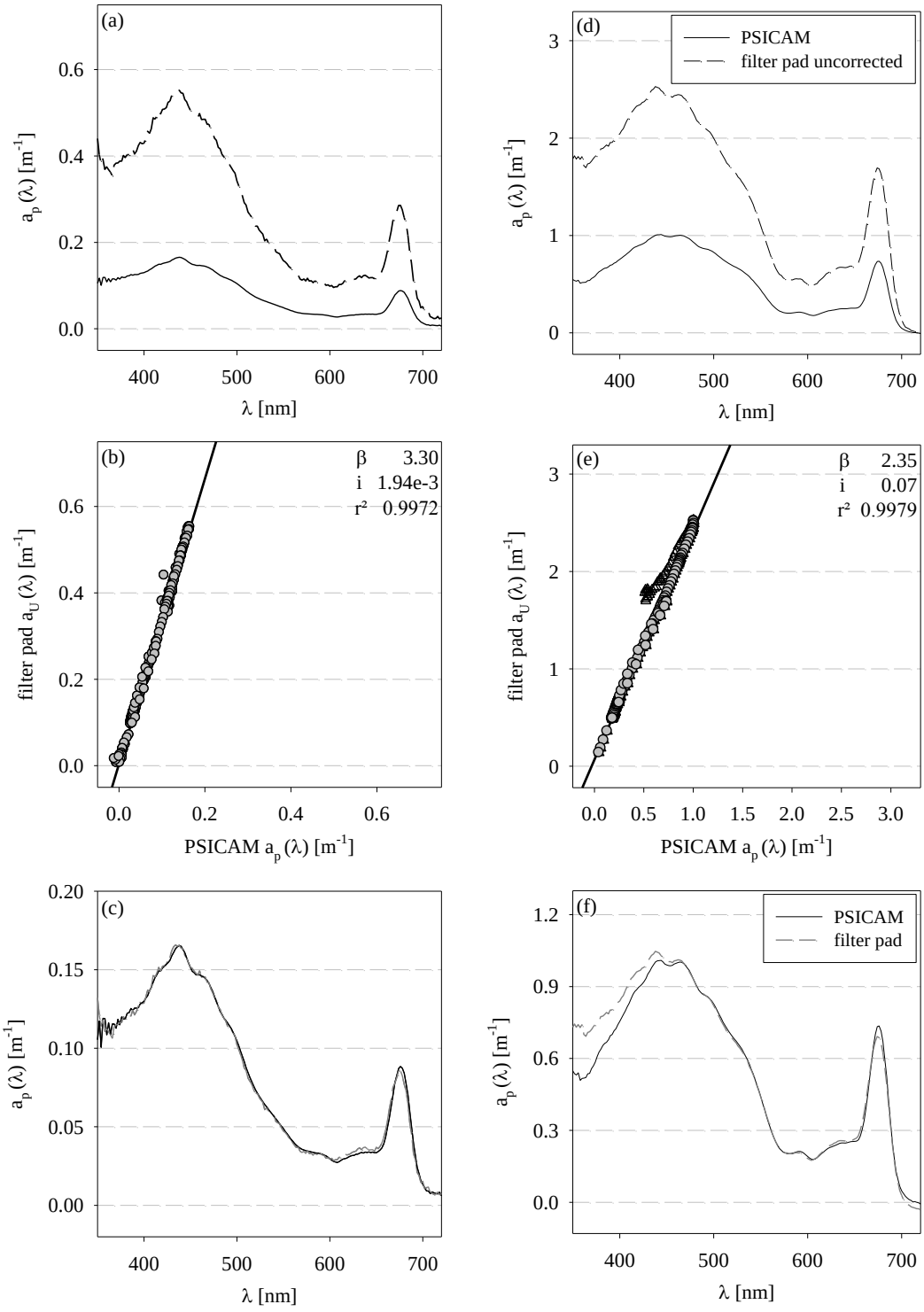

Fig. 4.2 (a) and (d) PSICAM data, a_p, and uncorrected (β = 1) filter pad data, a_u, of two different samples. (b) and (e) linear regression and corresponding coefficients and R^2 for the same samples. Data ranges for the linear regression were limited to 400 – 700 nm for (b) and 440 – 700 nm for (e). (c) and (f) show final particulate absorption spectra measured with PSICAM and T-method. Filter pad data have been offset corrected and re-scaled using Eq. 4.3 and the coefficients derived in (b) and (e) respectively.

A common feature of these recent studies is the apparent sample-by-sample dependency in β and a linear relationship between a_p and a_u for low OD_f. Results suggest that the OD dependency of β that was previously observed might be due to insufficient accuracy in measurements of OD_s due to scattering effects and/or overloading of filters. The comparison with PSICAM data enables the correction of measurements on a sample-by-sample basis for both β-factor and scattering artefacts.

4.4. Limitations of PSICAM measurements

The PSICAM is well-suited for determining absorption coefficients for natural water samples due to a combination of its insensitivity to scattering and a long effective pathlength. PSICAM measurements require little sample preparation and sample alteration due to handling is minimised. In contrast, measurements with many other commonly available bench-top instruments require filtration or concentration of the sample which might cause cell breakage (and associated loss of pigments) and can potentially change the optical properties of a sample significantly compared to under *in situ* condition.

However, PSICAM measurements outside the visible spectrum have proven to be challenging due to very low signal levels with artefacts regularly observed in both the UV and NIR (as discussed above). Particularly in the blue/UV the current set-up using a tungsten lamp as broadband light source reaches its limits. As this effect can occur in both total absorption and CDOM absorption determinations, it can result in large uncertainties in the blue/UV spectral region when propagated into final particulate absorption coefficients. In the absence of additional measurements, it is very difficult to determine the exact wavelength at which absorption coefficients are affected by this systematic error as it changes with constituent concentration and measurement configurations.

As filter pad absorption is measured in a scanning, monochromatic dual-beam spectrophotometer and gain settings can be adjusted with wavelength, measurements are less susceptible to issues due to low intensity signal levels in the blue/UV. Fig. 4.2 shows data for two samples only one of which exhibits PSICAM underestimation in the UV. By plotting uncorrected filter pad absorption against PSICAM data (Fig. 4.2, (b) and (e)), there is a clear point of deviation in one of the plots (Fig. 4.2(e)) where the effect of PSICAM underestimation becomes obvious. These data points can then be excluded from further analysis. The linear regression slope and offset is generated using only the linear range of the

data, but can be applied to the entire filter pad spectrum. The approach presented here can therefore help extend the range of accurate particulate absorption coefficients into the UV and NIR (Fig. 4.2, (c) and (f)) and at the same time provide a quality control mechanism for PSICAM measurements. The combination of filter pad absorption data measured with the T-method and PSICAM is recommended for generating best quality particulate absorption data.

4.5. Variability in β-factors

4.5.1. Differences between geometric configurations

Using the linear regression approach, distributions of β-factors were derived for measurements made on the UKCW cruise in 2015 with three different geometrical configurations (T-method, IS-method and QFT-ICAM). The coefficient of determination for linear regression against PSICAM data was > 0.92 for all samples. Observed median β values varied strongly between the different methods and were over 60% larger for the integrating sphere methods with median values of 4.5 for the IS-method and 3.9 for the QFT-ICAM compared to 2.5 for the T-method (Table 4.2).

Table 4.2 Median and 95% prediction intervals for β-distributions derived for three different geometrical configurations used for 51 samples collected on the UKCW cruise in 2015. Data (362 – 726 nm), where PSICAM sensitivity issues in the blue were observed, were excluded from this comparison.

Method	Median	95% prediction intervals
T-Method	2.5	± 1.3
QFT-ICAM	3.9	± 1.0
IS-method	4.5	± 1.7

Mean β-factors varied very slightly from the values (4.56 and 4.06 for IS-method and QFT-ICAM, respectively) presented in Röttgers *et al.* (2016) because here the HZG filter pad data are compared against the Strath PSICAM rather than HZG PSICAM absorption data. Measurements made inside integrating spheres tend to amplify the pathlength more strongly

and hence result in larger β than the T-method. Importantly, the apparent variability in β (95% prediction intervals, Table 4.2) was similar across all geometries, which suggests that the integrating cavity methods might not have a significant intrinsic advantage over the T-configuration.

4.5.2. Variability within the T-method

Across the three different datasets, median β values derived for the T-method ranged from 2.2 for the AC-IOPs dataset to 3.2 for the BP09 cruise with 95% prediction intervals of ± 1.0 to ± 1.7, respectively (Table 4.3). The median value determined for measurements made with the T-method on the UKCW cruise was 2.5 ± 1.3 (Fig. 4.3). Uncorrected filter pad absorption data generally underestimated PSICAM absorption in the NIR which resulted in small negative intercepts (positive offset correction) in the linear regression. 69% of all intercepts, *i*, were within ± 0.025 m^{-1}. Largest intercepts (< -0.2 m^{-1}) were observed for samples with high NIR absorption, e.g. in the Bristol Channel or for bottom water samples.

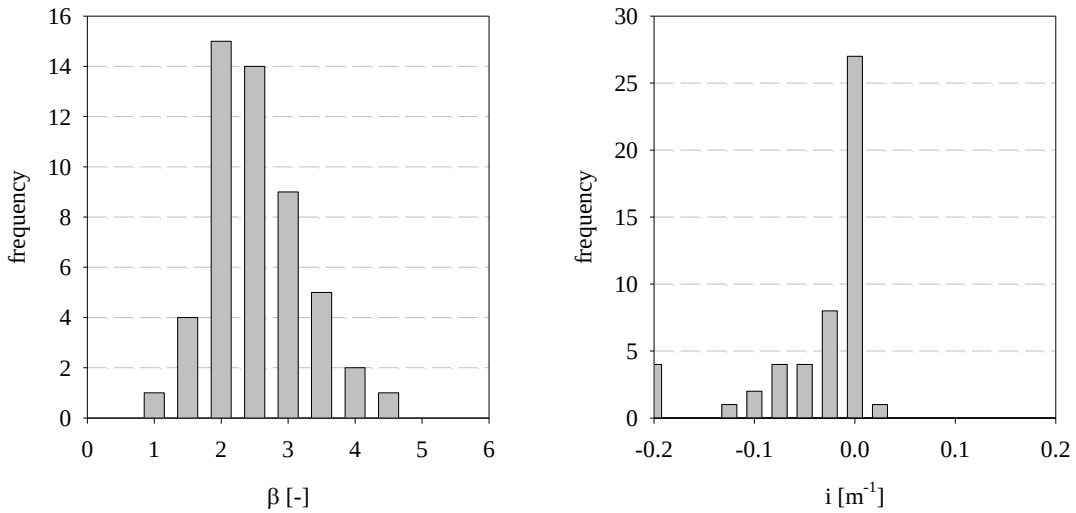

Fig. 4.3 Distributions of (a) β-factors (regression slopes) and (b) scattering offsets (*i*, regression intercepts) determined for 51 filter pad absorption measurements made on the UKCW cruise using the T-method.

4.5.3. Sources of variability in β-factors

An experiment was conducted to investigate the magnitude of differences between β-factors determined for a single sample sub-sampled onto multiple filter papers. The aim was to

assess if the variability within measurements made with the same configuration (Table 4.3) can potentially be explained by natural sample variability or variation between individual filter papers.

Table 4.3 Median and 95% prediction intervals for β-distributions derived for three different datasets and measurements with the T-method.

Dataset	Median	95% prediction intervals
Algal cultures	2.2	± 1.0
BP09	3.2	± 1.7
UKCW	2.5	± 1.3

Two 5 L samples, one natural sample collected from a stream in the Scottish Highlands and one from a diluted green algae culture (*D. maritima*), were divided into five 1 L sub-samples and the particulate absorption was measured with the PSICAM and T-method filter pad absorption technique. For the natural sample, a high CDOM concentration, $a_{CDOM}(440\ nm) = 0.95\ m^{-1}$, resulted in low PSICAM signal levels in the blue, and the linear range was limited to data from 480 – 700 nm for all natural sub-samples in this experiment.

Fig. 4.4 shows the regression plots and associated β-factors for the different sub-samples. Observed median β values were (by chance) similar, approx. 2.75, for both the natural sample and the algal culture sample. The variability in β of ± 0.25 observed here, which is assumed to be due to differences between individual filter pads, does not fully explain the overall variability of > ± 1.0 in β in the T-method for natural sample datasets. This suggests that variability in β is due to a combination of both filter pads and sample variability.

During the AC-IOPs experiments, samples from 4 cultures were measured 2 - 3 times within a 2 week period. β-factors determined for samples of the same species varied strongly and showed a tendency to increase over time (Fig. 4.5), suggesting that stable species-specific β values are not easily reproduced. A potential explanation for the observed tendency in β to increase could be increasing concentrations of bacteria and detrital material due to ageing of the cultures which might affect the packaging of cells on the filter paper. Results, however, remain somewhat inconclusive due to the limited amount of data available.

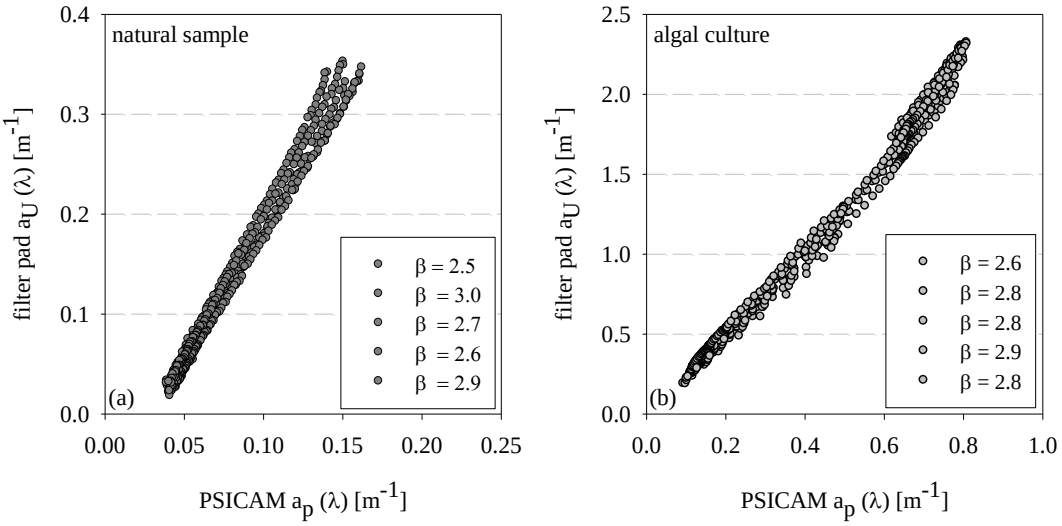

Fig. 4.4 Slopes of linear regression applied to uncorrected filter pad absorption, a_u, (Eq. 4.1 with β = 1.0) vs. particulate absorption measured in a PSICAM, a_p, for 5 sub-samples of the same (a) natural sample and (b) sample of *D. maritima*. Data in (a) is limited to the linear range from 480 – 700 nm, data in (b) to 400 – 700 nm.

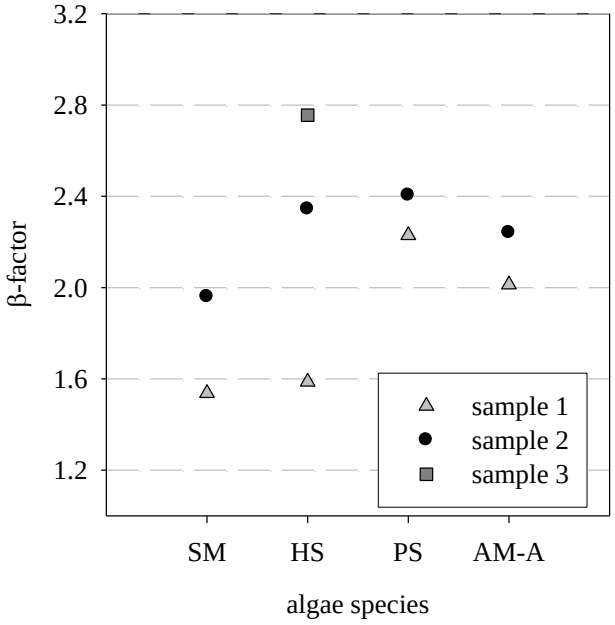

Fig. 4.5 Multiple determinations of β-factors for samples made up using 4 different algal species within a 2 week time period. SM – *Skeletonema marinoi*, HS – *Heterocapsa spp*., PS – *Pseudonitzschia seriata*, AM – *Alexandrium minutum.*

4.6. Effect of different filter pad absorption corrections

The performance of different correction methods for filter pad absorption measurements with the T-method was tested on the UKCW dataset. The analysis was limited to the spectral range in which linear relationships between a_u and PSICAM data were observed, and up to a maximum range of 362 – 726 nm. Results showed excellent agreement (RMS%E = 3.2%) between measurements corrected with the linear regression approach and a_p measured with a PSICAM (Fig. 4.6(a), Table 4.4). This value, however, masks remaining large individual errors, some greater than 100%, for particulate absorption values < 0.5 m^{-1}. Any deviation from the sample-by-sample approach, such as applying an average slope (Fig. 4.6(b)) or a null-correction (Fig. 4.6(c)), leads to larger differences greater than 20%, between the two measurements. The linear regression approach improves the agreement of filter pad data with PSICAM data in 2 ways: (1) sample-specific β-factors have a positive effect by accounting for filter and sample artefacts discussed above and (2) the application of offsets accounts for sample dependent scattering artefacts.

Fig. 4.6 also shows examples of performance of two previously published corrections, the earliest (Mitchell, 1990) and most recent work (Stramski *et al.* 2015). Data correction with historic correction methods (Table 4.4) showed lower agreement with PSICAM data, with a minimum RMS%E of 20.7% and a maximum of almost 46% for the approach proposed by Allali *et al.* (1997).

The regression approach to correct NIR scattering offsets resulted in 1 order of magnitude smaller intercepts derived from subsequent linear regression applied to the comparison with PSICAM data (Table 4.4) and high R^2 (> 0.95) even when approximated β-factors were applied. Null-correcting filter pad absorption data consistently resulted in negative intercepts compared to PSICAM measurements, which means that NIR absorption values are systematically underestimated. Inappropriate correction of NIR-offsets therefore clearly has a strong impact on the overall performance of the quantitative filter pad technique.

To date, the effect of pathlength amplification and scattering artefacts on bleached filters remains unknown and future work is required to investigate if required correction coefficients change from measurements of the unbleached filter to the bleached sample. However, the absence of a partitioning method for PSICAM measurements, and hence lack

of validation data, is currently hindering studies of non-algal particulate absorption measurements.

Table 4.4 Slope, intercept and coefficient of determination (R^2) for linear regression applied to corrected filter pad absorption data vs. PSICAM data (in the linear range). Overall agreement is given as RMS%E.

reference	slope [-]	intercept [m^{-1}]	R^2	RMS%E [%]
regression slope + offset	0.99	0.000	0.999	3.2
regression slope + null correction	1.38	-0.012	0.913	19.7
average slope + regression offset	0.72	-0.001	0.954	19.6
average slope + null correction	1.00	-0.012	0.877	20.8
Stramski *et al.* (2015)	0.77	-0.017	0.801	42.6
Stramska *et al.* (2003)	0.94	-0.018	0.814	29.6
Finkel and Irwin (2001)	0.96	-0.012	0.871	22.4
Roesler (1998)	1.04	-0.013	0.877	20.7
Allali *et al.* (1997)	0.63	-0.010	0.849	45.7
Arbones *et al.* (1996)	0.90	-0.014	0.851	26.9
Tassan and Ferrari (1995)	0.98	-0.015	0.847	24.4
Cleveland and Weidemann (1993)	0.92	-0.015	0.845	26.6
Hoepffner and Sathyendranath (1992/1993)	0.79	-0.013	0.836	34.5
Bricaud and Stramski (1990)	0.79	-0.016	0.818	38.7
Mitchell (1990)	0.98	-0.016	0.839	25.2

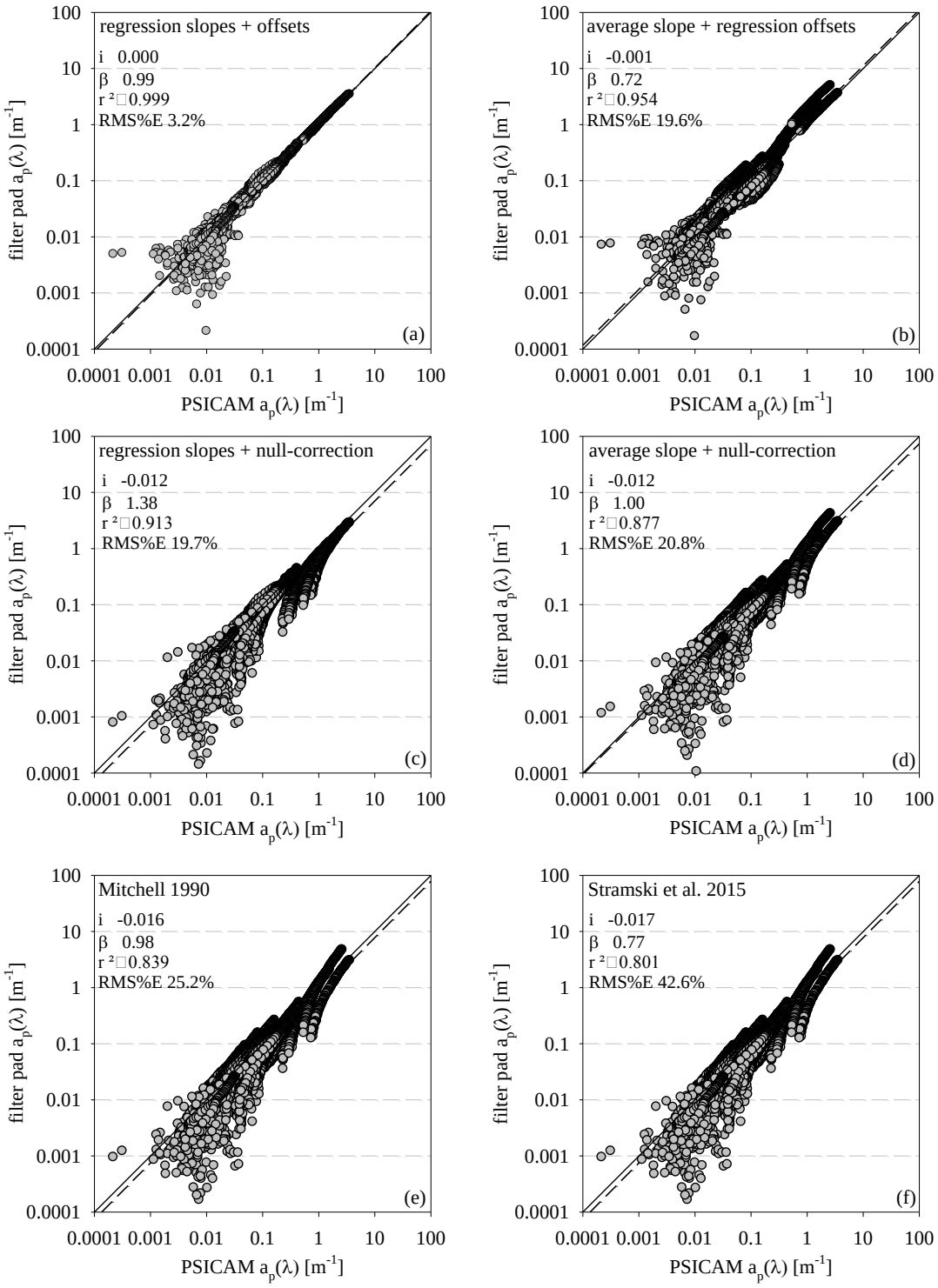

Fig. 4.6 The effect of different filter pad absorption correction methods on the agreement between a_p derived from PSICAM and filter pad measurements from 362 – 726 nm (except where PSICAM data were limited to eliminate artefacts due to very low intensity signals), made on the UKCW cruise in 2015. (a)-(d) show variations of the linear regression correction in comparison to two previously published corrections by (e) Mitchell (1990) and (f) Stramski *et al.* (2015).

.

4.7. Comparison of different geometric configurations

Fig. 4.7 shows the agreement of corrected filter pad absorption data obtained using the T-method, the IS method and the QFT-ICAM with a_p measured in a PSICAM. Data from all four measurements were available for a total of 51 samples. RMS%Es were broadly comparable for all three filter pad methods (1.7 - 3.2%) and regression slopes against PSICAM data were all within 1.5% of unity (Table 4.5).

Given the comparable levels of performance, there appears to be no clear benefit to more complex approaches over the relatively simple T-method. Correction for scattering effects using the regression approach effectively compensates the T-method for the sensitivity to scattering errors. This results in insignificant differences in corrected NIR absorption between the different configurations (Fig. 4.8) which could be observed for the majority of samples from the UKCW cruise with a variety of different constituent compositions and concentration ranges, e.g. more sediment loaded waters North of Anglesey (ST19; Fig. 4.8 (b)) and phytoplankton dominated samples (ST50; Fig. 4.8 (e)).

There is overall little apparent deviation between data measured with the different techniques. However, in some cases (e.g. ST45; Fig. 4.8 (d)), small differences in the spectral shape between data obtained with the QFT-ICAM and the other techniques could be observed. This can potentially be explained by pigment fluorescence which might affect the different geometries to a varying extent. Fluorescence effect might be more of an issue in QFT-ICAM measurements because it uses a white light source, cells are concentrated onto a filter paper and signals are amplified inside the integrating cavity (also Chapter 6). Largest differences between the different techniques could generally be observed at wavelengths < 350 nm but due to a lack of feasible validation data, quantification of measurement performances was not possible.

The three different geometries returned similar corrected a_p which is an indication of reasonable performance of filter pad measurements for wavelengths > 360 nm. This illustrates how filter pad data can help to extend the spectral range of particulate absorption coefficients beyond the range of a typical PSICAM measurement. Cross-validation can also be helpful to identify PSICAM data of poorer quality, e.g. in the NIR for ST38 (Fig. 4.8 (c)).

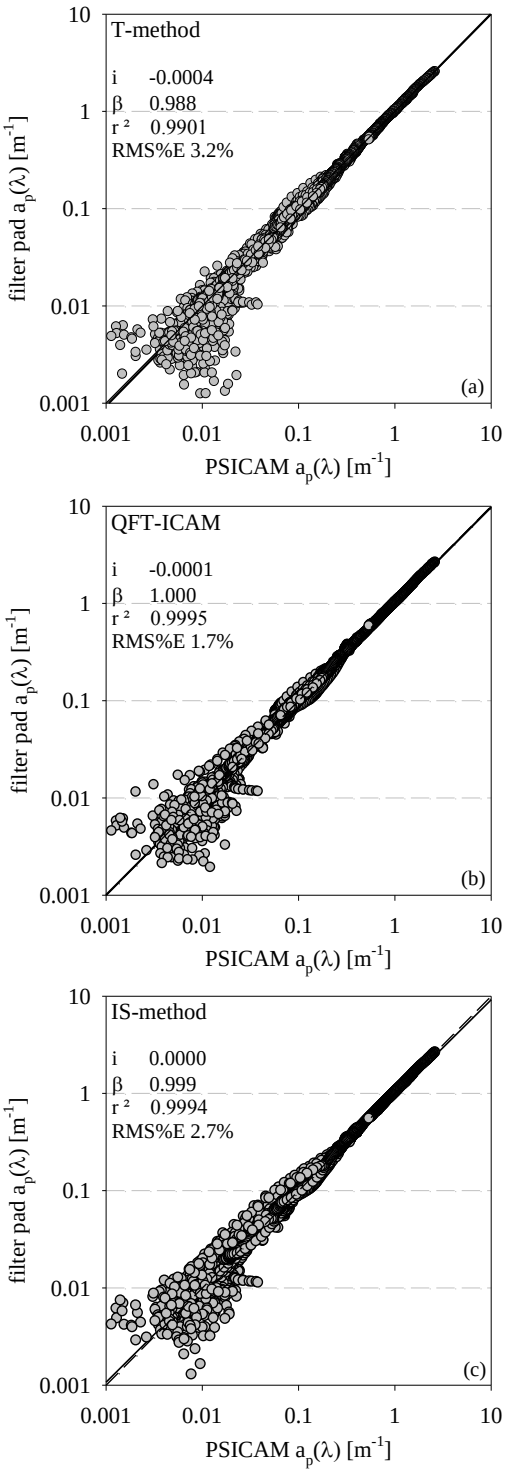

Fig. 4.7 The effect of the linear regression filter pad absorption correction methods on the agreement a_p derived from PSICAM and filter pad measurements using different geometric configurations: (a) T-method, (b) QFT-ICAM and (c) IS-method. Data presented is a subset of 51 stations sampled during the UKCW cruise in May 2015, from 362 – 726 nm (except where PSICAM data were limited to eliminate artefacts due to very low signal levels).

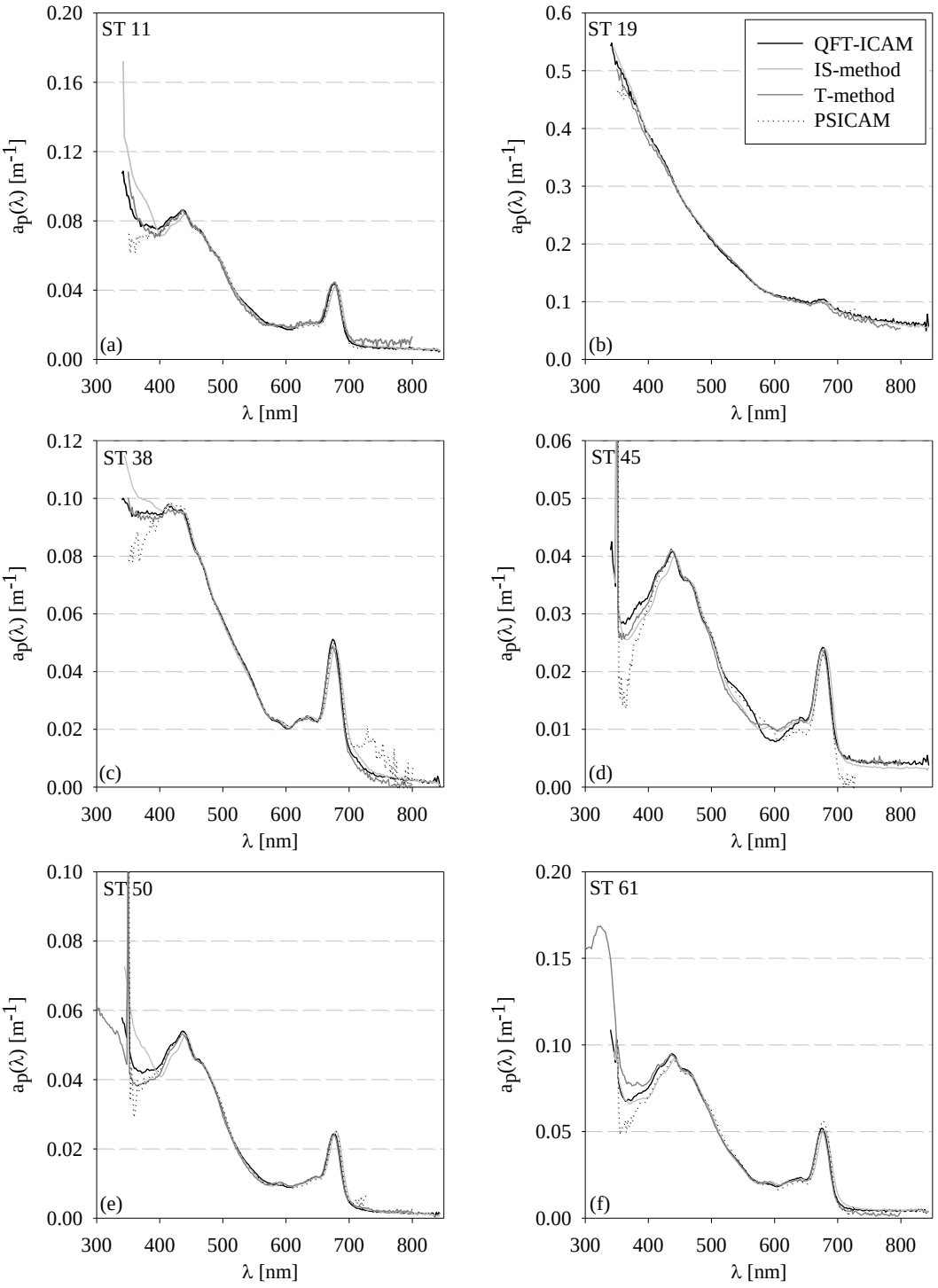

Fig. 4.8 Agreement between particulate absorption coefficients determined from measurements with 3 different filter pad configurations and a PSICAM for 6 example stations sampled on the UKCW cruise in 2015.

Benefitting from relative simplicity and availability, the combination of T-method and PSICAM is capable of producing higher quality a_p data than either technique on its own, and as good as any of the other filter pad techniques in combination with the PSICAM. None of the filter pad techniques offer a satisfactory standalone solution.

Table 4.5 Performance of three different filter pad configurations corrected with the linear regression approach compared to PSICAM data (362 – 726 nm) from the UKCW cruise. Data where PSICAM sensitivity issues in the blue were observed, were excluded from this comparison.

method	slope [-]	intercept [m^{-1}]	R^2	RMS%E [%]
T-method	0.988	-0.0004	0.9991	3.2
QFT-ICAM	1.000	-0.0001	0.9995	1.7
IS-method	0.999	0.0000	0.9994	2.7

4.8. Conclusions

The availability of PSICAM data enabled significant progress in the development of the methodology to determine quantitative particulate absorption coefficients from filter pad measurements. The comparison of filter pad and PSICAM data confirmed previous observations of linear relationships (Röttgers and Gehnke, 2012, McKee *et al.*, 2014, Röttgers *et al.*, 2016). Fitting a linear function through the data provides regression coefficients (slope and intercept) which can be used to correct filter pad absorption measurements and match them with PSICAM data on a sample-by-sample basis, resulting in agreement within 3.2% RMS%E. The linear regression approach clearly distinguishes between pathlength amplification and scattering offset artefacts and has the advantage that it can be extrapolated to wavelengths where the PSICAM data are either suspect or otherwise unavailable, e.g. filter pad data beyond spectral range of the PSICAM data. The linear correction outperforms previously proposed correction methods (RMS%E > 20%) but is dependent on the availability of PSICAM data. Unfortunately, this eliminates application to historic datasets and imposes a significant additional experimental burden on future work. However, improved quality absorption data might be more accessible to the wider community in the near future through new commercially available integrating cavity absorption meters, such as the Trios OSCAR and the Turner Designs flow-through ICAM.

The traditional T-method, despite its theoretically higher measurement uncertainties, does not perform significantly worse than more complex configurations. In fact, the simplicity of the measurement protocol makes the T-method favourable for future field work campaigns where time and labour are limited.

It has been demonstrated here that filter pad absorption measurements benefit from complementary PSICAM measurements to derive appropriate correction coefficients. At the same time, PSICAM data have been shown to benefit from the availability of corresponding filter pad data as this enables identification of wavelengths at which sensitivity issues occur. Cross-validation with filter pad absorption data can provide a quality control mechanism which is useful in identifying measurement artefacts and improves the overall quality of measured IOPs.

5. Optical closure for marine waters from *in situ* IOP measurements

5.1. Introduction

Similar to the developments made with regards to filter pad absorption data, PSICAM data has been used to develop new scattering corrections for submersible AC-9 measurements. Two new scattering correction schemes for *in situ* absorption and attenuation data measured with AC-9 instruments have been published recently using PSICAM data for direct validation (Röttgers *et al.*, 2013, McKee *et al.*, 2013). This chapter will attempt a different approach based on radiative transfer simulations to investigate the impact of these new scattering corrections through comparison with *in situ* radiometry. This will indirectly validate the PSICAM performance as the new AC-9 correction being tested, are designed to replicate PSICAM performance. Results and analysis presented here were published in Lefering *et al.* (2016).

5.1.1. Limitations in AC-9 measurements

AC-9 measurements can suffer from significant scattering errors in both the absorption and attenuation sensors. Errors in the absorption measurements originate from limitations in the reflective tube design which fails to collect all scattered light beyond a critical angle of ~41° (McKee *et al.*, 2013). This results in systematic overestimation of absorption coefficients. In water, the AC-9 attenuation sensor has a relatively wide collection angle of ~0.9° which fails to exclude photons scattered in the forward direction at angles smaller than the collection angle of the lens-aperture system. Boss *et al.* (2009) demonstrated that uncorrected AC-9 attenuation data were systematically lower by almost a factor of 2 than equivalent attenuation data from a LISST100X (Sequoia Scientific), which has a much smaller collection angle (~0.02° in water).

A variety of scattering corrections approaches for AC-9 absorption measurements have previously been proposed, making different assumptions about the spectral nature of scattering and volume scattering coefficients and the absorption signal in the NIR. Of these

corrections, the proportional correction (Zaneveld *et al.*, 1994) has been most commonly used in the past (e.g. Twardowski *et al.*, 1999, Sullivan *et al.*, 2006, Mitchell *et al.*, 2014). Two new AC-9 scattering corrections, based on iterative and semi-empirical approaches, appear to offer improvements in the quality of *in situ* absorption and attenuation data which is particularly significant for coastal waters with typically high scattering. Recent studies (de Carvalho *et al.*, 2015, Sokoletsky and Shen, 2014) showed that different AC-9 corrections strongly affect remote sensing signals modelled using RT modelling. It is therefore interesting to re-assess the extent to which these new corrections impact on optical closure.

5.1.2. Applications for optical closure

Here the performance of the two new AC-9 scattering corrections is tested and compared with the proportional correction in an optical closure exercise. Optical closure is effectively a test for consistency between *in situ* IOP and radiometry measurements using RT simulations. In an ideal scenario, underwater light fields, modelled based on measurements of IOPs, precisely replicate radiometric data collected at the same time. Achieving optical closure means that both IOP and radiometry measurements as well as the RT model are at least mutually consistent.

In the past, however, optical closure has proven difficult to achieve and has been used to identify limitations in *in situ* IOP data. For example, Chang *et al.* (2003) identified the scattering correction for AC-9 absorption measurements and assumptions about the volume scattering function as limiting factors. Their work also showed that the parameterisation of chlorophyll fluorescence in the model and the accuracy of radiance measurement are major sources of uncertainty in optical closure tests. Several studies have since investigated the effect of particle characteristics, such as the slope of the particle size distribution and the shape of the VSF, on optical closure (Mobley *et al.*, 2002, Bulgarelli *et al.*, 2003).

Most studies test optical closure on apparent optical properties, mainly the remote sensing reflectance, R_{rs}, rather than underwater radiometric measurements. Tzortziou *et al.* (2006) additionally, attempted optical closure for in-water radiometry profiles and showed excellent agreement for the surface layer (down to 3m) with percentage deviations of < 18% across the spectrum just beneath the surface (1m depth). Their work also highlights the sensitivity of RT models to inelastic effects, in particular chlorophyll fluorescence.

In addition to the assessment of consistency for *in situ* IOP and radiometry measurements, the degree of optical closure achieved can provide a measure of accuracy in modelled

underwater light fields based on *in situ* IOP data. Quantification of uncertainties in RT outputs is of great interest for coupled ecosystem modelling and assimilation of ocean colour remote sensing data. Fujii *et al.* (2007) have shown the advantages of integrating optical and RT models into existing ecosystem models, particularly in improving modelled subsurface light fields as the main driver for many photo-chemical processes. Data from RT models are also commonly used to develop satellite remote sensing algorithms (Stramski *et al.*, 1999, Lee *et al.*, 2002, Mitchell *et al.*, 2014). Understanding the practical performance limitations for modelling underwater light fields is essential in the context of ensuring that RT models are interpreted appropriately.

This chapter will examine closure results for a range of coastal and oceanic waters and test the impact of uncertainties in IOP measurements on both surface reflectance parameters and light field parameters at depth. Simultaneous comparison of simulated profiles of downwards irradiance, $E_d(\lambda)$, and upwards radiance, $L_u(\lambda)$, against *in situ* observations presents a robust test of optical closure. It is insufficient to test against $E_d(\lambda)$ alone as in most cases this is pinned to the above surface irradiance, $E_s(\lambda)$, which is a boundary condition of the RT model. The combination of $E_d(\lambda)$ and $L_u(\lambda)$ profiles effectively provides an end-to-end test of all the major components of the RT model, with successful modelling of these parameters ensuring the quality of derived higher level products. As the new AC-9 scattering corrections effectively match AC-9 absorption data with PSICAM data, demonstrating optical closure using corrected AC- 9 data is an additional indirect validation of PSICAM performance.

5.2. AC-9 scattering correction methods

This section includes the description of the three AC-9 scattering corrections used for the optical closure assessment performed in this work using the LS and WCS datasets. A detailed outline of sampling locations, data acquisition and measurement protocols can be found in Chapter 2.

5.2.1. The proportional correction

The proportional correction was described by Zaneveld *et al.* (1994). It is based on two assumptions: (1) negligible NIR absorption and (2) wavelength independent scattering phase function. Measured absorption coefficients are corrected using the accompanying attenuation measurements of the AC-9 to estimate a wavelength dependent scattering error as follows

$$a_{ac9}(\lambda) = a_m(\lambda) - a_m(715\text{ nm}) \times \frac{(c_m(\lambda) - a_m(\lambda))}{(c_m(715\text{ nm}) - a_m(715\text{ nm}))} \quad [m^{-1}] \quad [5.1]$$

where a_{ac9} is the corrected non-water absorption [m^{-1}] at a given wavelength, λ [nm], a_m is the uncorrected (measured) absorption coefficient [m^{-1}] and c_m is the measured attenuation coefficient [m^{-1}]. The proportional correction forces all absorption spectra through zero at 715 nm, the reference NIR wavelength where non-water absorption is assumed to be zero. However, it has been shown that this assumption does not hold for waters with an increased NIR absorption due to high levels of non-biogenic minerals or CDOM (Tassan and Ferrari, 2003, Stramski *et al.*, 2007, Röttgers *et al.*, 2014a). The extent to which the scattering phase function can be considered wavelength independent also remains a subject of debate with significant wavelength dependence having been found in certain highly turbid areas (McKee and Cunningham, 2005, Chami *et al.*, 2006b, McKee *et al.*, 2009).

5.2.2. The semi-empirical correction

The semi-empirical correction by Röttgers *et al.* (2013) is a development of the basic form of the proportional correction. It includes an additional scattering correction for attenuation measurements and allows for non-zero NIR absorption values (Eq. 5.2).

$$a_{ac9} = a_m - [a_m(715\text{ nm}) - a_{emp}(715\text{ nm})] \text{ x } \frac{\frac{1}{e_c}c_m(\lambda) - a_m(\lambda)}{\frac{1}{e_c}c_m(715\text{ nm}) - a_{emp}(715\text{ nm})} \quad [m^{-1}] \quad [5.2]$$

where $1/e_c$ is a scattering correction for the attenuation measurement. Boss *et al.* (2009) found an average value of $e_c = 0.56$ for a single wavelength. This attenuation correction is used in Eq. 5.2 and for subsequent use of attenuation data in RT simulations testing the performance of the semi-empirical correction method. $a_{emp}(715\text{ nm})$ [m^{-1}] is determined from an empirical relationship (Eq. 5.3). Instead of forcing the absorption spectrum through zero at 715 nm, the semi-empirical correction applies an empirical relationship between uncorrected AC-9 NIR readings and PSICAM absorption data at this wavelength. The PSICAM has a higher sensitivity and accuracy than the AC-9 and can determine very low absorption coefficients in the NIR accurately due to the instrument's long effective pathlength.

$$a_{emp}(715\ nm) = 0.212\ [a_m(715\ nm)]^{1.135} \qquad [m^{-1}] \qquad [5.3]$$

5.2.3. The iterative correction

The iterative correction uses a different approach to correct both absorption and attenuation measurements for scattering errors (McKee *et al.*, 2013). Additional backscattering measurements are used to calculate particulate backscattering ratios which are then used to parameterise the Fournier-Forand phase function (Fournier and Forand, 1994, Mobley *et al.*, 2002). Estimates of the VSF are used in a model to predict appropriate, wavelength dependent scattering errors. Prior Monte Carlo simulations of the absorption and attenuation flow cells were used to tune the instrument-specific wall reflectance, accounting for ageing and imperfections. An appropriate wall reflectance for this sensor was selected through comparison with associated PSICAM data. The limited availability of PSICAM data across the community, however, means that this approach is not as widely available for other users although this might change with increasing use of commercial ICAM instruments. The iterative correction method also makes no assumptions about NIR absorption.

5.3. Radiative transfer modelling

EcoLight 5.0 (Sequoia Scientific) was used to model underwater light fields, i.e. profiles of downward irradiance, $E_d(\lambda)$, and upwards radiance, $L_u(\lambda)$. EcoLight is the faster version of the more complete RT model Hydrolight and is more suitable for many potential applications, such as incorporating RT models into coupled ecosystem models. The difference between outputs from EcoLight and a full Hydrolight run tested on one station sample on the WCS cruise showed differences less than 2.6 % for L_u and less than 0.5% for E_d across the profile and all wavebands considered.

The model was populated using *in situ* IOP profiles of absorption, attenuation (AC-9) and backscattering (BB-9) data collected and processed using the three scattering corrections discussed above. E_d and L_u were computed only for AC-9 wavelengths and depths at which radiometry data were available to minimise artefacts due to inter- and extrapolation. EcoLight requires information on the shape of the VSF and generates Fournier-Forand scattering phase functions from derived particulate backscattering coefficients. The incoming solar radiation was parameterised using estimates of percentage cloud cover and the median

above surface downwards irradiance spectra $\bar{E}_s(\lambda)$, averaged over the acquisition time of the underwater light field profiles. Modelling of inelastic scattering processes was restricted to Raman scattering by water molecules. CDOM and phytoplankton fluorescence were not included in the model due to a lack of required depth profiles of constituent concentrations and fluorescence quantum yields.

5.4. Optical closure assessment

Optical closure was tested by comparing RT model outputs of radiometric parameters and apparent optical properties with profiles derived from *in situ* measurements (Fig. 5.1). Optical closure performance was assessed for profiles of E_d and L_u for three wavebands in the blue, green and red, at 440 nm, 532 nm and 650 nm, respectively.

PAR(z), the depth resolved photosynthetically available radiation, can be used to quantify the overall availability of light for plant growth at a certain depth. It is therefore a parameter of great interest in many bio-optical applications and productivity models. *PAR* is calculated by integrating E_d across the visible spectrum (Eq. 5.4) and is therefore less likely to be sensitive to wavelength dependent artefacts.

$$\mathrm{PAR(z)} = \sum_{400\ \mathrm{nm}}^{700\ \mathrm{nm}} \frac{\lambda}{\mathrm{hc}}\, \mathrm{E_d}(\lambda,\mathrm{z})\, \Delta\lambda \qquad [\mathrm{photons\ s^{-1}\ m^{-2}}] \qquad [5.4]$$

where E_d [W m^{-2} nm^{-1}] is the downwelling irradiance at the centre of an AC-9 waveband, λ [nm], and depth, z [m]. $h = 6.626 \times 10^{-34}$ [N m s] is Planck's constant and $c = 2.998 \times 10^{8}$ [m s^{-1}] is the speed of light in a vacuum.

$R_L(\lambda,z_{min})$ is the wavelength dependent radiance reflectance at the closest measurement to the sea surface, z_{min} [m], and is calculated using

$$\mathrm{R_L}(\lambda, \mathrm{z_{min}}) = \frac{\mathrm{L_u}(\lambda, \mathrm{z_{min}})}{\mathrm{E_d}(\lambda, \mathrm{z_{min}})} \qquad [\mathrm{sr^{-1}}] \qquad [5.5]$$

R_L was used as a proxy for remote sensing reflectance, R_{rs}, and can provide information on the quality of RT model outputs for applications in validation of ocean colour remote sensing data and development of new algorithms.

In order to assess the degree to which optical closure has been achieved for a given dataset (i.e. by cruise), median and range of best-fit slopes were derived from linear regressions applied to each profile (model against *in situ* measurements). All data were log-transformed prior to the analysis as each parameter varied over orders of magnitude with depth. All coefficients of determination, R^2, were found to be > 0.95. Slopes greater than 1.0 indicate modelled values decrease too rapidly with depth, i.e. the corresponding attenuation is overestimated by the model, and vice versa.

Root mean square percentage errors, RMS%E (Eq. 5.6) calculated for the original (not log-transformed) data provide information on the spread between modelled and measured datasets.

$$\mathrm{RMS\%E}=\sqrt{\frac{1}{n}\sum_{1}^{n}\left(\frac{x_{model}-x_{measured}}{x_{measured}}\times 100\right)^2} \quad [\%] \quad [5.6]$$

where x represents either $E_d(z, \lambda)$, $L_u(z, \lambda)$, $R_L(\lambda)$, or $PAR(z)$, n is the number of data points, x_{model} and $x_{measured}$ are the modelled and measured value, respectively.

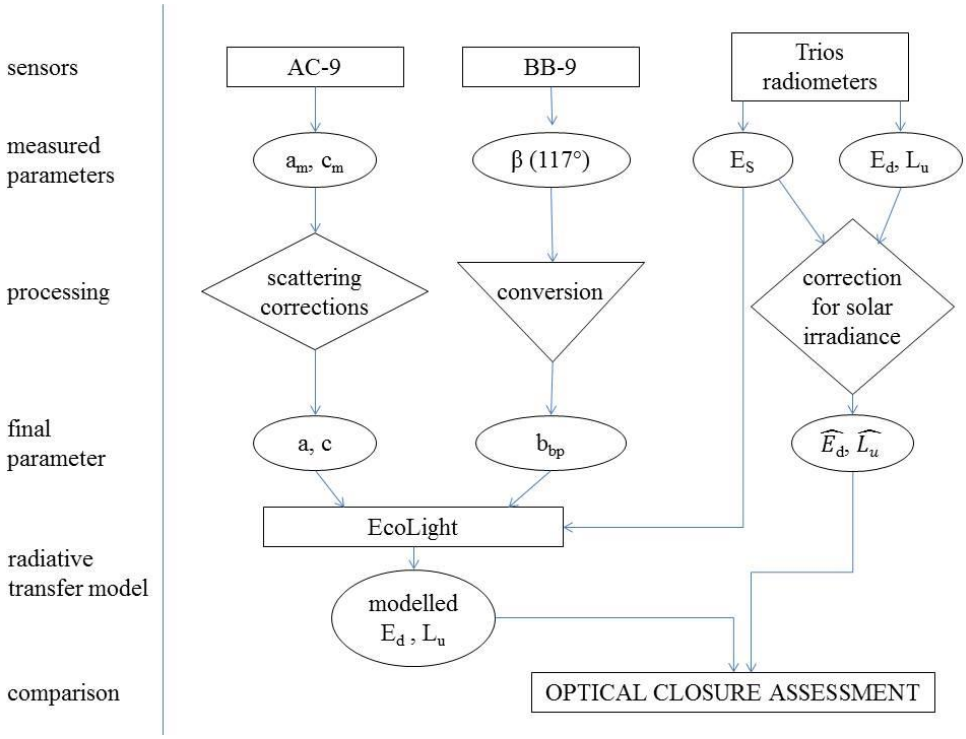

Fig. 5.1 Diagram of optical closure assessment, describing the process from *in situ* determinations, subsequent data processing, and final comparison of measured RT modelled parameters.

5.5. Results

5.5.1. Comparison of different AC-9 correction methods

The effect of the different scattering corrections is presented for two example stations sampled on the WCS cruise in 2012. ST05 was located at 56° 43.317' N, 006° 16.585' W and was a reasonably clear station close to Ardnamurchan Point. ST12 was a more turbid station located in the upper basin of Loch Linnhe at 56° 45.503' N, 005° 13.544' W. Compared to ST05, ST12 exhibited 2 fold higher absorption and backscattering just below the surface, while scattering coefficients were 3 times higher (Fig. 5.2 – 5.4). For these stations, the choice of AC-9 scattering correction had only very little effect on measured absorption spectra, with effectively constant deviation across the spectrum and a maximum of 0.017 m^{-1} (ST12). At longer wavelengths, spectra corrected with the proportional correction exhibited consistently lower absorption values due to the assumption of negligible absorption at 715 nm. The iterative correction performed poorly at two stations sampled in a coccolithophore bloom (data not shown) where it returned negative absorption values at 650 nm and 715 nm. These stations exhibited very high backscattering coefficients (b_{bp}(440 nm) > 0.011 m^{-1}). There are several potential reasons for this. One is that the assumptions underpinning b_b deviation, the so-called χ-factor, are breached in these conditions. This feature potentially points towards issues in the selection of scattering phase functions, as the Fournier-Forand phase function assumes a power law particle size distribution which may not be appropriate in such bloom conditions.

Larger differences between the different correction methods could be observed for attenuation spectra. While the proportional correction does not include a correction for attenuation data (and therefore always gives lowest attenuation coefficients), the semi-empirical correction increases the attenuation by a constant factor of 1.78. The iterative correction changes the magnitude of attenuation for every waveband and station individually which can lead to strong deviations from the original spectral shape. For both ST05 and ST12, the iterative correction returned smaller attenuation values compared to the semi-empirical correction but this pattern was not consistent across the dataset.

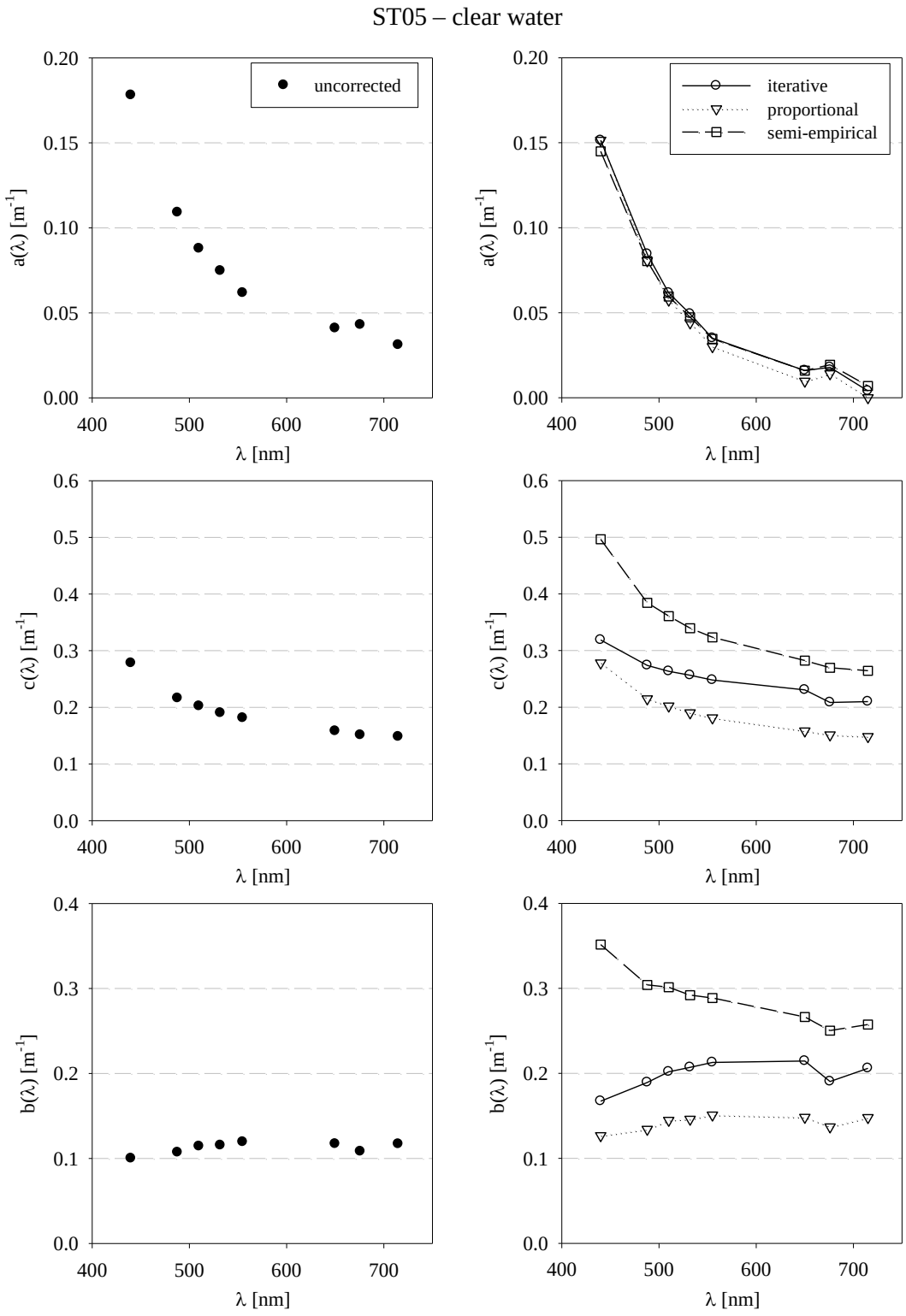

Fig. 5.2 Measured AC-9 absorption, $a(\lambda)$, attenuation, $c(\lambda)$, spectra and calculated scattering ($b(\lambda) = c(\lambda) - a(\lambda)$) spectra for ST05 (clear water) of the WCS cruise. Left: uncorrected measurements. Right: the effect of three different AC-9 scattering corrections, proportional, iterative and semi-empirical, on the different parameters.

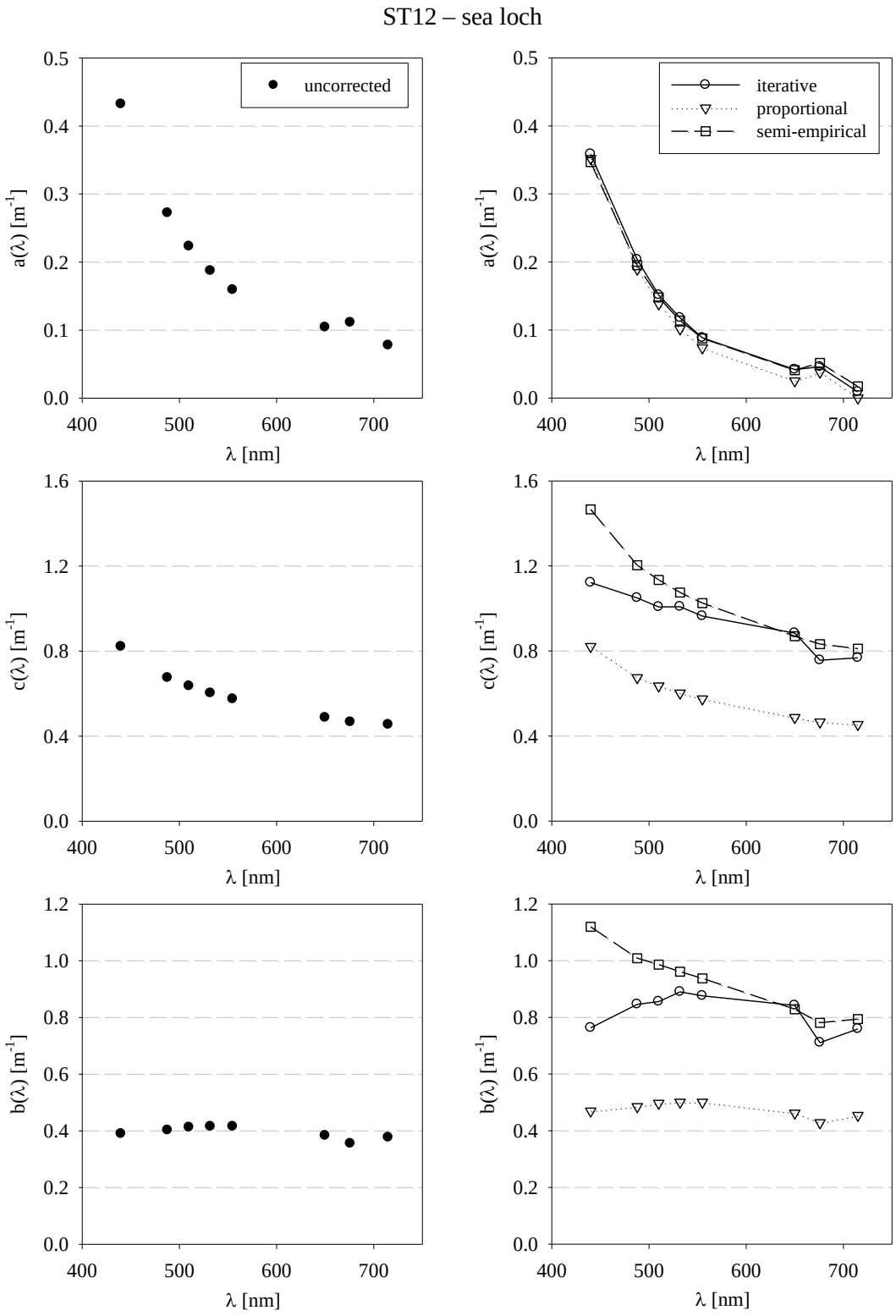

Fig. 5.3 Measured AC-9 absorption, $a(\lambda)$, attenuation, $c(\lambda)$, spectra and calculated scattering ($b(\lambda) = c(\lambda) - a(\lambda)$) spectra for ST12 (sea loch water) of the WCS cruise. Left: uncorrected measurements. Right: the effect of three different AC-9 scattering corrections, proportional, iterative and semi-empirical, on the different parameters.

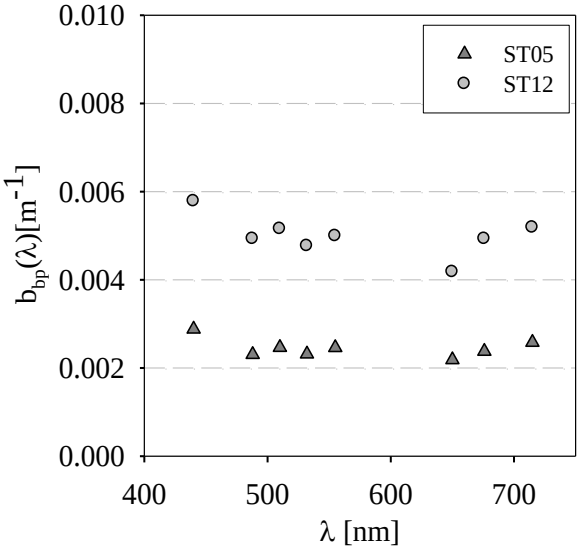

Fig. 5.4 Spectral particulate backscattering coefficients, $b_{bp}(\lambda)$, measured with a BB-9 for station ST05 (clear water) and ST12 (sea loch water) of the WCS cruise (2012), as used to populate the RT model.

Fig. 5.5 shows E_d and L_u profiles for the example stations ST05 and ST12 at 650 nm as this waveband is considered to be least susceptible to any inelastic scattering effect. Limited differences between the different AC-9 correction schemes could be observed for modelled E_d profiles. Modelled E_d(650 nm) values deviated less than 38% from the *in situ* observations and generally with largest percentage differences at greater depths. Profiles of modelled L_u(650 nm) were found to be similarly insensitive to the choice of AC-9 scattering correction. Overall, RT outputs for this dataset show little sensitivity to the different AC-9 corrections despite their large effect on attenuation data. As most of the scattered light will be scattered in the forward direction, changing the magnitude of attenuation coefficients has only very little effect on RT calculations as the impact on the light field structure is minimal (Gordon, 1993).

In the following sections, the performance of the optical closure test is therefore demonstrated graphically using data corrected with the proportional correction only as it is the easiest to implement and most commonly applied in literature. Statistical descriptors of the impact on optical closure are, however, given for all correction methods.

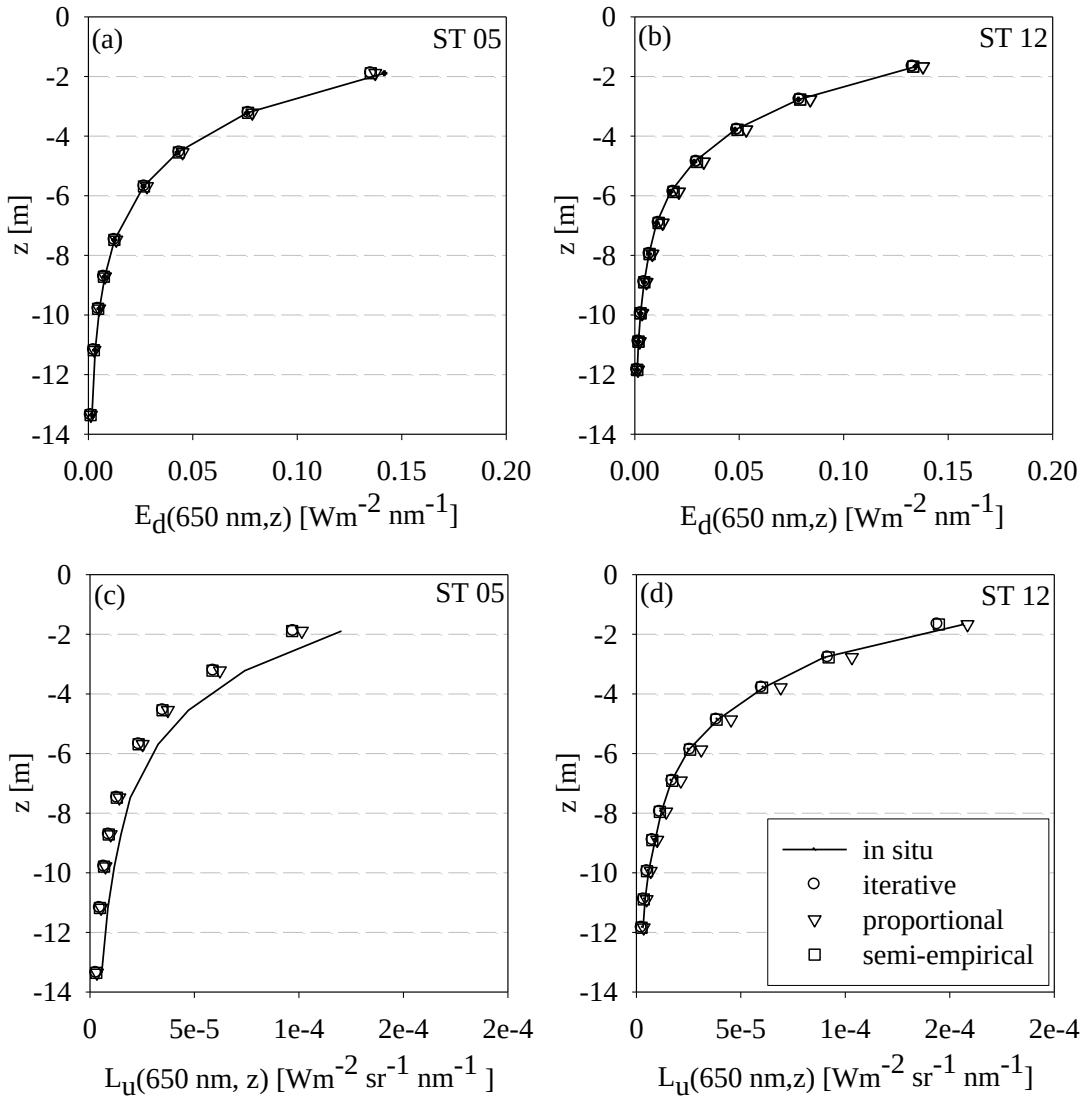

Fig. 5.5 Modelled and measured E_d ((a) and (b)) and L_u ((c) and (d)) profiles measured at two stations, ST05 (clear water) and ST12 (sea loch water), from the WCS cruise. The RT model was populated with AC-9 data corrected with three different corrections: proportional, iterative and semi-empirical.

5.5.2. E_d *closure*

Modelled and measured E_d profiles were overall in very good agreement for both datasets and across all wavebands 440 nm, 532 nm and 650 nm (Fig. 5.6), with RMS%E across profiles between 12 - 38%. Median and variability in regression slopes decreased (approaching 1.0) towards longer wavelengths (Table 5.1 and 5.2). Median regression slopes

> 1.0 are an indicator for a tendency of the RT model to underestimate E_d with depth. Similar model performance was observed for both datasets which were collected with independent radiometry set-ups.

The different AC-9 corrections exhibited a similar spectral pattern of median slopes, with the exception of the semi-empirical correction for E_d determined on the LS cruise (Table 5.1 and 5.2). The lowest spread in E_d data was achieved using the proportional correction and generally for the green waveband for all corrections. Using the proportional correction the RMS%E was 15.3% for the LS dataset and 12.4% for the WCS. The spread was highest for the iterative correction with 19.7% and 21.4%, for LS and WCS, respectively. RMS%E varied typically less than 10% across the different corrections for the datasets analysed here.

The two coccolithophore stations sampled on the WCS cruise showed the greatest deviation of all stations between modelled and measured E_d. The difference was significantly higher in the blue (> 40%) than at red wavelength (typically < 10%) and is potentially a major contributor to the overall optical closure performance for the WCS dataset at 440 nm.

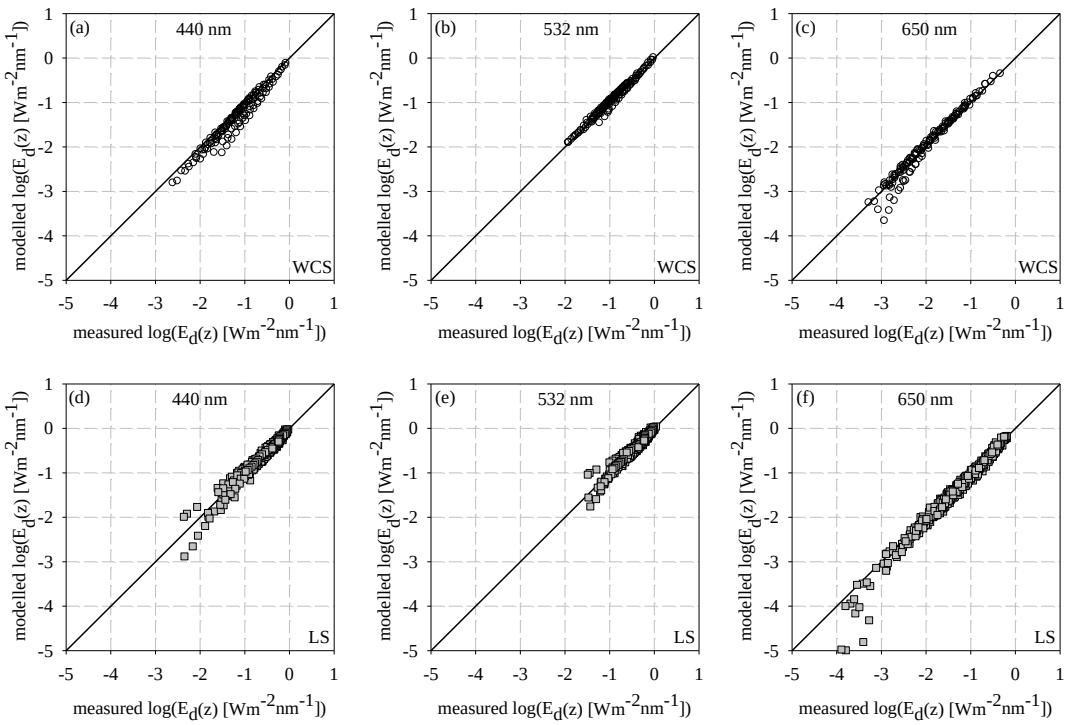

Fig. 5.6 Agreement between modelled and measured $E_d(\lambda,z)$ for data collected off the West Coast of Scotland (WCS; (a) - (c)) and in the Ligurian Sea (LS; (d) - (f)). Results are presented for three different wavelengths, 440 nm, 532 nm and 650 nm (from left to right). All IOP measurements used as input for the RT modelling were corrected using the proportional correction.

Table 5.1 Minimum, maximum and median slopes obtained from linear regressions applied to depth profiles for all stations of the LS cruise in 2009 and each of the AC-9 scattering corrections. Slope values > 1.0 represent a tendency of modelled data to underestimate *in situ* value.

	proportional			iterative			semi-empirical		
LS slopes	median	min	max	median	min	max	median	min	max
E_d(440 nm,z)	1.14	0.80	1.70	1.16	0.83	1.71	0.97	0.72	1.43
E_d(532 nm,z)	1.11	0.83	1.64	1.14	0.90	1.68	0.99	0.60	1.47
E_d(650 nm,z)	1.07	0.96	1.22	1.07	0.96	1.26	1.03	0.93	1.22
L_u(440 nm,z)	1.09	0.62	1.28	1.14	0.63	1.47	0.92	0.60	1.31
L_u(532 nm,z)	1.06	0.48	1.23	1.13	0.48	1.47	0.94	0.47	1.53
L_u(650 nm,z)	1.14	0.89	1.83	1.17	0.91	1.92	1.09	0.85	1.75
PAR(z)	0.96	0.64	1.26	1.07	0.88	1.40	1.05	0.84	1.39

Table 5.2 Minimum, maximum and median slopes obtained from linear regressions applied to depth profiles for all stations of the WCS cruise in 2012 and each of the AC-9 scattering corrections. Slope values > 1.0 represent a tendency of modelled data to underestimate *in situ* value.

	proportional			iterative			semi-empirical		
WCS slopes	median	min	max	median	min	max	median	min	max
E_d(440 nm,z)	1.22	1.06	1.43	1.21	1.08	1.36	1.24	1.07	1.60
E_d(532 nm,z)	1.03	0.90	1.36	1.09	0.96	1.42	1.14	0.96	1.46
E_d(650 nm,z)	1.01	0.94	1.29	1.04	0.96	1.29	1.05	0.97	1.40
L_u(440 nm,z)	1.19	1.04	1.35	1.19	1.03	1.35	1.19	1.03	1.50
L_u(532 nm,z)	1.07	0.91	1.40	1.16	0.94	1.58	1.19	0.94	1.52
L_u(650 nm,z)	1.11	0.95	1.42	1.15	0.97	1.38	1.14	0.97	1.57
PAR(z)	1.06	0.92	1.28	1.09	0.99	1.31	1.13	1.00	1.42

5.5.3. L_u *closure*

Modelled L_u profiles were generally in good agreement with *in situ* observations (Fig. 5.7). L_u median slopes were in the same range as E_d median slopes but lowest for the green waveband in both datasets (Table 5.1 and 5.2). The spread in the data was slightly higher compared to E_d and RMS%E were < 36% and < 47% for the proportional correction and the LS and WCS cruises, respectively. The highest degree of optical closure of L_u, i.e. lowest spread in the data, was achieved with the iterative correction with RMS%E < 42% for both datasets across all wavebands. Results showed that modelled L_u outputs tend to attenuate too quickly. This is to a large extent propagated from the corresponding underestimation of E_d as indicated by significantly better optical closure performance of R_L (Section 5.3.5). Again, the magnitude of median regression slopes for L_u did not differ significantly between the two datasets containing independent radiometry data collected using different instruments. This points towards remaining errors being associated with issues in the parameterisation of IOP inputs rather than in the determination of radiometric profiles in the field.

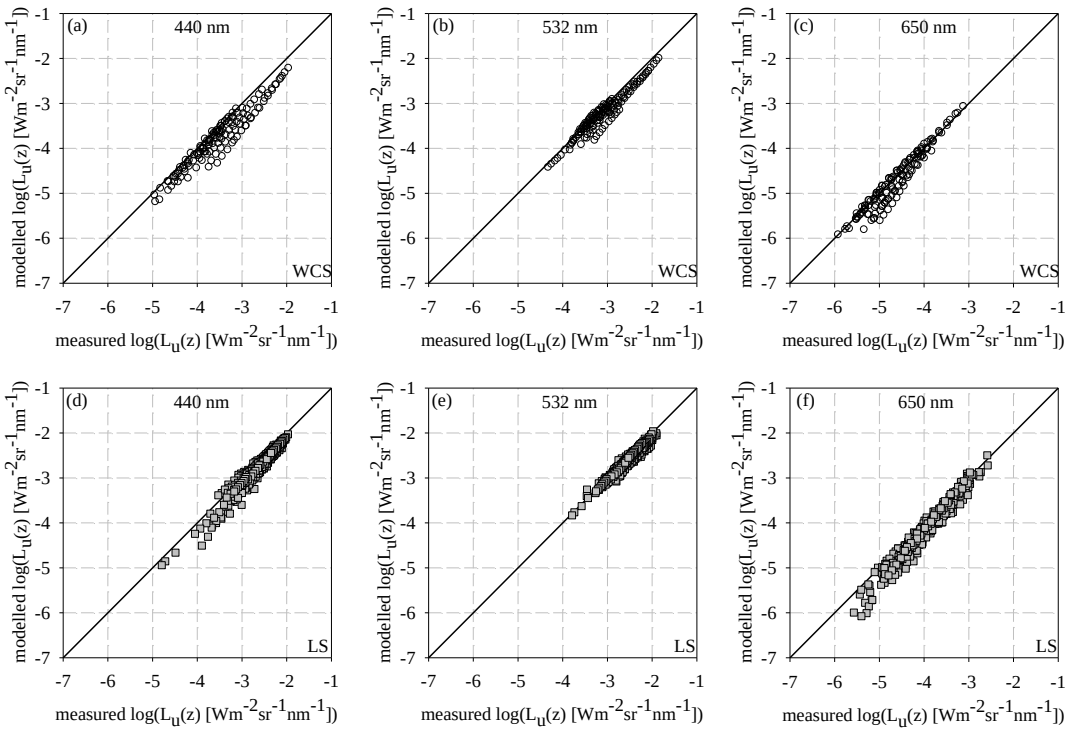

Fig. 5.7 Agreement between modelled and measured $L_u(\lambda,z)$ for data collected off the West Coast of Scotland (WCS - (a), (b) and (c)) and in the Ligurian Sea (LS (d), (e) and (f)). Results are presented for three different wavelengths, 440 nm, 532 nm and 650 nm (from left to right). All IOP measurements used as input for the RT modelling were corrected using the proportional correction.

Table 5.3 RMS%E as a measure for overall agreement between modelled and measured data from LS and WCS cruises. Comparison between different AC-9 scattering corrections.

	proportional		iterative		semi-empirical	
RMS%E [%]	LS	WCS	LS	WCS	LS	WCS
E_d(440 nm,z)	22.3	33.9	22.8	30.7	20.0	37.9
E_d(532 nm,z)	15.3	12.3	18.0	13.0	19.7	21.4
E_d(650 nm,z)	26.1	22.6	28.4	22.4	22.9	25.5
L_u(440 nm,z)	30.4	46.1	33.0	41.3	36.7	49.0
L_u(532 nm,z)	18.9	33.8	25.6	37.4	62.9	45.6
L_u(650 nm,z)	35.9	32.8	40.4	35.0	30.8	40.1
PAR(z)	21.0	15.1	18.1	14.9	15.8	24.4
$R_L(\lambda,z_{min})$	24.0	32.6	24.8	32.2	30.2	31.4

L_u is generally more susceptible to inadequate parameterisation of the RT model, in particular regarding inelastic scattering effects. The non-inclusion of CDOM and chlorophyll fluorescence in the simulations can potentially explain the increased deviation in L_u compared to E_d. For example, the underestimation was found to be significantly greater at 676 nm because chlorophyll fluorescence has a greater effect at this wavelength (not shown).

5.5.4. Modelling PAR

Optical closure for *PAR* was excellent with median best fit slopes within ± 6% of unity for the proportional correction (Fig. 5.8). With a maximum slope of 1.13, the other AC-9 corrections performed at a similar level. *PAR* is typically modelled within 15 - 25% (RMS%E) of measured values demonstrating that it is a more robust parameter than $E_d(\lambda)$ because it is less susceptible to wavelength dependent artefacts.

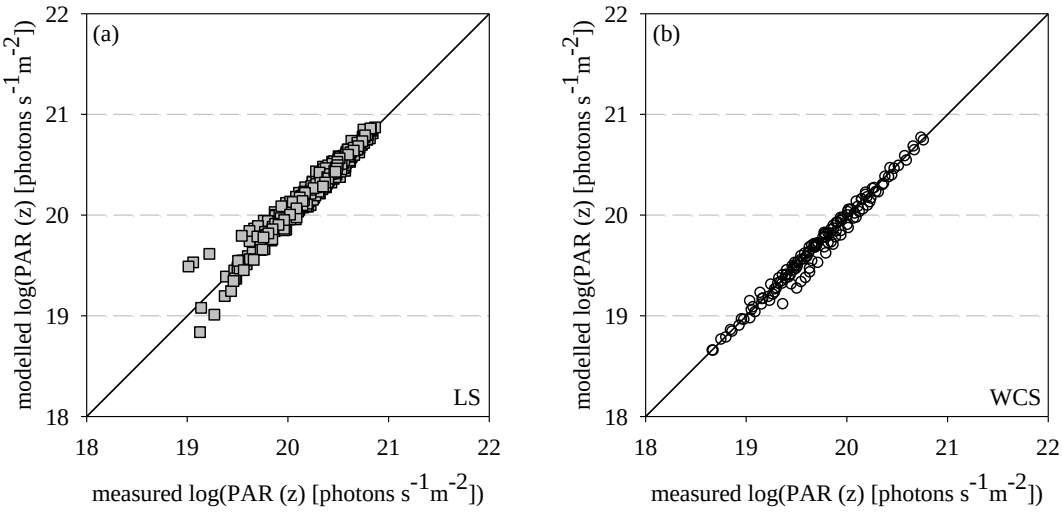

Fig. 5.8 Correlation of modelled and measured data for *PAR*(z) for (a) the Ligurian Sea (LS) and (b) measured off the West Coast of Scotland (WCS).

5.5.5. Modelling remote sensing signals

The degree of optical closure of R_L just below the surface can provide information on uncertainties in RT outputs used for validation of remote sensing reflectance. 'Water leaving' radiances, and hence R_{rs}, were not assessed here to minimise the effect of extrapolation up to and through the surface on closure. As R_L was studied at a single depth only, it was not possible to use regression slopes as informative descriptor for closure.

The comparison of modelled and measured data showed a tendency for RT models to underestimate R_L moderately (Fig. 5.9) across the full spectral range. The agreement was better for data collected on the LS cruise, RMS%E 24%, than for the WCS cruise, 33%. The RMS%E for R_L was slightly smaller than for L_u just below the surface (< 26% for LS data, < 37% for WCS data), suggesting that the mis-match in L_u data was to a small extent a result of underestimation in E_d profiles. The negative impact of not including inelastic scattering effect on L_u closure can propagate through into R_L which has adverse effects on the optical closure performance.

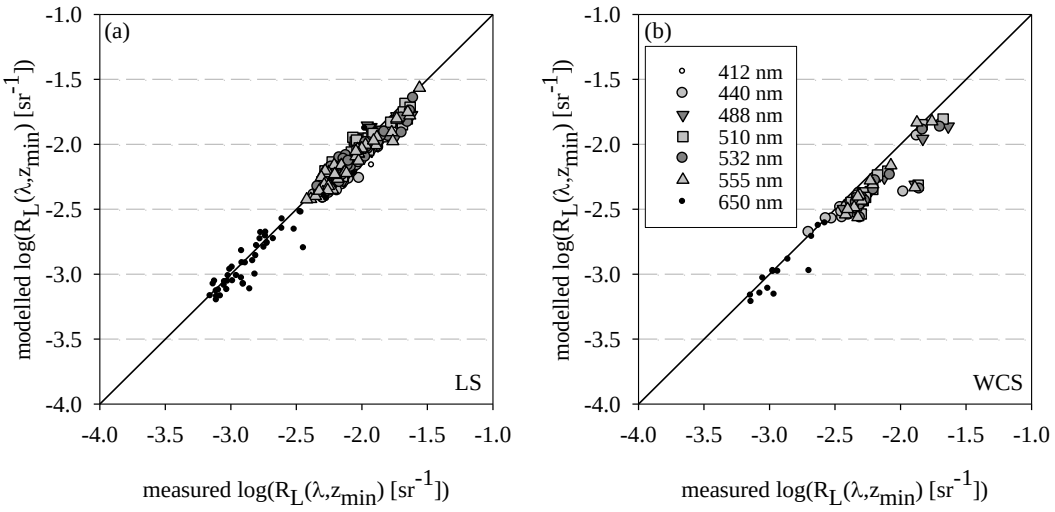

Fig. 5.9 Agreement between modelled and *in situ* data for the radiance reflectance, $R_L(\lambda)$, just beneath the surface for two datasets collected in (a) the Ligurian Sea and (b) off the West Coast of Scotland. 412 nm was excluded from the analysis of the WCS dataset due to sensor failure.

5.6. Effect of *in situ* measurement uncertainties on optical closure performance

5.6.1. Uncertainties in IOP measurements

A comparable degree of closure of E_d and L_u and a general tendency of the model to overestimate the attenuation of both parameters with depth was found for both datasets. The choice of AC-9 correction only weakly influenced the optical closure performance for the majority of stations tested here despite large differences in corrected beam attenuation. These results are in agreement with Gordon (1993) who found that uncertainties in attenuation data did not have a significant effect on RT model outputs. However, it should be noted that applying an appropriate correction to attenuation data might be necessary for other applications, i.e. when deriving scattering coefficients from AC-9 measurements to relate to particle size distributions.

The largest impact of the AC-9 absorption corrections was in the NIR, with the choice of NIR offset corrections affecting data across the spectrum. For the dataset used here (i.e. only moderately turbid waters), non-water absorption at longer wavelengths is a small fraction of the absorption by water itself which is why the differences between corrected AC-9

absorption data were insignificant at most sampling sites. This explains why the proportional correction scheme performed at least as well as the more complex methods despite the assumptions it is based on. The iterative and semi-empirical corrections are expected to outperform the proportional correction in highly turbid waters with high NIR absorption. However, due to the limited number of stations with high turbidity in these datasets, findings remain inconclusive. Results presented here do, however, serve as a warning that limitations in the parameterisation of the VSF are potentially a continuing problem in high turbidity waters due to the fact that both the iterative scattering correction and the EcoLight modelling, performed poorly for the two coccolithophore stations. Further effort, focussed on more turbid systems, is required to address this issue.

The residual mis-match between modelled and measured radiometry also requires further consideration. For example, there are potential errors in the determination and calculation of backscattering coefficients from measurements with a BB-9. b_b is derived by simple extrapolation from a measurement of the VSF at a single angle by application of a χ-factor. The underlying assumptions on the angular distribution of the VSF potentially limit the accuracy of b_b. Although increasing the backscattering coefficient, e.g. by increasing the χ-factor by up to a factor of 2, was found to improve closure for L_u it does so at the expense of closure for E_d. There is, however, scope for a more complex error in b_b than a simple calibration slope error, for example an offset error in the calibration. Unresolved angular structure in the VSF could potentially change the structure of the light field without necessarily having a strong impact on b_b values.

5.6.2. Radiometry

The model tendency to underestimate E_d and L_u with depth occurs for both datasets. This could be due to the RT model overestimating the attenuation of both modelled E_d and L_u with depth, suggesting unresolved issues in the IOP parametrisation in the RT model. Alternatively it would point to errors in the *in situ* radiometry measurements. The degree of optical closure observed for both datasets suggests that both radiometry configurations perform similarly well. Although both radiometer systems were calibrated against NIST standards there is a possibility that they are potentially susceptible to the same type of calibration error. One potential contributor to the residual mis-match could be increasing sensitivity of both radiometer systems to changes in the angular distribution of the light field at greater depths, for example, due to imperfections in the cosine collectors. Although

radiometry errors cannot be ruled out entirely, it seems more likely that other aspects of the RT model parametrisation are responsible for the residual mis-match.

5.7. Parameterisation of the RT model

Observed discrepancies between modelled and measured parameters can to some extent be attributed to either *in situ* measurements (both IOPs and radiometry) or other errors in the parameterisation of the RT model (e.g. the diffuse vs. direct components of the incoming solar irradiance).

The parameterisation of the VSF has a strong impact on optical closure (Chami *et al.*, 2006a, Chang and Whitmire, 2009). As discussed above, our knowledge of the shape of the VSF is limited especially for scenarios where the particle size distribution potentially deviates from a power law relationship. Angularly resolved spectral VSF data are required for future studies to improve our understanding of factors limiting optical closure.

Raman scattering by water was the only inelastic scattering effect incorporated in the RT simulations. Including CDOM and chlorophyll fluorescence in the model will most likely improve the agreement with *in situ* observations for L_u and R_L whilst not adversely affecting E_d. Including chlorophyll fluorescence has been shown to reduce underestimation from 30 - 40% to about 4 - 8% (Tzortziou *et al.*, 2006). Their study also found that, including CDOM fluorescence has a smaller effect on optical closure but can still result in an improvement by up to 5% at green wavelengths. In order to model fluorescence effects constituent concentrations and quantum yields have to be provided. The latter, however, have been shown to be highly variable and challenging to quantify (e.g. resolving depth variation of chlorophyll fluorescence yields (Kiefer, 1973, Andrew *et al.*, 2013). Estimation of quantum yields was beyond the scope of this work but certainly needs further investigation in the future.

5.8. Conclusions

The work presented here was able to demonstrate an improved degree of optical closure with depth compared to previous studies which is evidence for the progress made in the determination of *in situ* optical measurements over the past decade. Developments in basic

radiometric and IOP measurement techniques have led to a good level of agreement between RT model and measurements for clear to moderately turbid waters.

An overall tendency for simulations to slightly underestimate measured radiometry values throughout the water column was observed in the majority of cases, which varied with parameter, wavelength and IOP correction method. The deviation between modelled and measured values typically increased with depth, suggesting either an overestimation of light attenuation in the RT model due to inaccurate parameterisation or unresolved errors in radiometric measurements. Quantification of the contribution of these potential errors sources to the residual mis-match requires future investigation with angularly resolved spectral VSF and radiance distribution data (Voss, 1989, Antoine *et al.*, 2013) for high turbidity waters. Further scope for improvement is the parameterisation of fluorescence effects in the RT model which requires accurate profile data for constituent concentrations and quantum yields.

Regression slopes were used to assess the estimates of light attenuation and were found to be typically within 15% of unity for both E_d and L_u. The overall wide range of slopes, however, highlights that closure can be significantly less satisfactory for individual stations. Results demonstrate that RT simulations, with current IOP measuring capabilities, can produce robust estimates of *PAR* within 15 - 25% (RMS%E) of measured data which is particularly welcome for bio-optical or ecosystem modelling applications. Results for R_L were slightly less satisfactory with RMS%E between 24 - 33%. This level of deviation has to be considered when using RT model outputs for development and validation of remote sensing algorithms.

The exact source of the residual mis-match remains unknown, but does not appear to be directly associated with scattering correction errors for *in situ* absorption and attenuation data. Errors in the scattering correction of *in situ* absorption and attenuation data measured with an AC-9 have been shown to have only very little influence on closure for these clear to moderately turbid samples. Optical closure with different scattering corrections varied by less than 10% (RMS%E) for E_d, and reached a maximum deviation of 44% (RMS%E) for L_u. The performance of the different AC-9 scattering corrections might vary more dramatically in waters with very high turbidity as suggested by the remaining fundamental problems encountered at the stations in strongly scattering waters sampled during the WCS cruise. Such issues are most likely to apply to similar phytoplankton blooms or strong mineral particle suspensions elsewhere. In these scenarios the PSICAM is well-suited to provide

validation data. The degree of closure achieved here strengthens our confidence in current *in situ* IOP measurement capabilities.

6. Inelastic scattering effects in PSICAM measurements

6.1. Introduction

After establishing the performance of the current set-up of the PSICAM (Section 2.4.2), this chapter will investigate what additional useful information can potentially be extracted from PSICAM measurements. It will simultaneously assess to what extent inelastic scattering effects can potentially explain the observed remaining discrepancies in absorption spectra measured with the PSICAM and other techniques, noting that they could influence one or both measurements. The spectral characteristics and magnitude of inelastic scattering signals inside a PSICAM cavity will be measured using a tuneable supercontinuum laser for narrow waveband (~ 10 nm) excitation. These results will be a first indication of whether inelastic scattering signals inside an integrating cavity are sufficiently strong to affect the accuracy of absorption measurements. Observed spectral fluorescence signatures will further indicate what additional information on a sample and its biological activity can collected during a PSICAM measurement. In a second step, the magnitude of inelastic scattering signals in the normal PSICAM set-up (with a broad band tungsten lamp) will be assessed, using a series of short pass cut-off filters integrated in the original set-up.

6.1.1. Inelastic scattering processes in natural waters

Scattering of light occurs where a photon encounters a phase boundary in the medium it is travelling through and is forced to deviate from a straight trajectory. In the process, the incoming photon is absorbed by a molecule which is excited in the process. The absorbed energy is almost immediately emitted as a new photon and the molecule returns to its initial energy state. When the emitted photon exhibits the same energy as the incoming photon, the process is called elastic scattering. An excited molecule can also emit a photon of a different wavelength, either longer or shorter, than the incident and therefore end up in an energy state different from the initial one. This process is then called inelastic scattering.

In the aquatic medium, there are 2 types of inelastic scattering processes of significance: (1) Raman scattering by water molecules and (2) fluorescence by organic components, such as

phytoplankton or CDOM. Knowledge of the inelastic scattering properties of a water body is important for parameterisation of RT models (Chapter 5). It affects the structure of underwater light fields which can be particularly significant in very clear or in phytoplankton or CDOM dominated waters.

Inelastic scattering processes can affect measurements of spectral absorption because the light re-emitted by the sample might increase the amount of light detected at certain wavelengths which would lead to an underestimation in absorption. This becomes particularly problematic when broadband white light is used to illuminate the sample, as is the case for PSICAM, QFT-ICAM and LWCC system determinations. When white light is used, identification and quantification of these effects are challenging because signals cannot be de-convoluted easily. Measurements inside an integrating cavity are particularly vulnerable to inelastic scattering effects due to amplification of these processes. Although PSICAM measurements are routinely corrected for chlorophyll fluorescence effects at red wavelengths (Section 2.4.2), no correction for other inelastic scattering effects are implemented in the current measurement protocol. To date, no study has investigated the impact of inelastic scattering on the accuracy of PSICAM absorption coefficients.

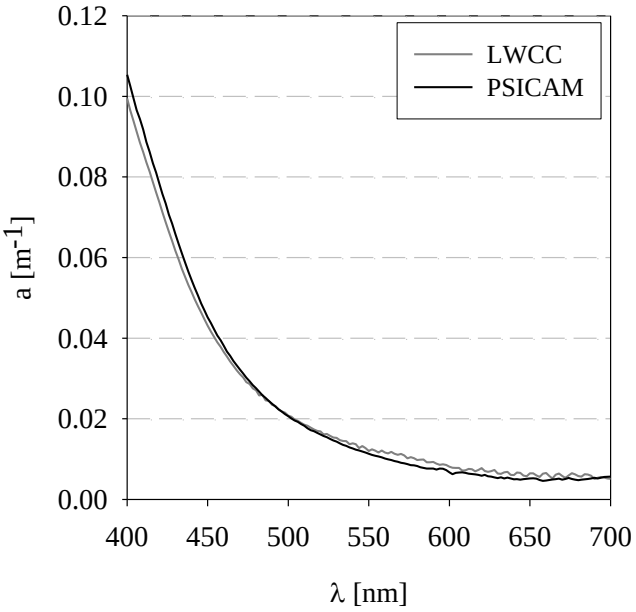

Fig. 6.1 Comparison between CDOM absorption spectra measured in a LWCC system and a PSICAM. The sample was collected in the Celtic Sea during the UKCW cruise in 2015.

Signal changes due to inelastic scattering could potentially explain small spectrally dependent differences which can be observed when comparing PSICAM measurements with other absorption measurements, such as the LWCC system (Fig. 6.1) or the filter pad absorption technique (Fig. 4.8).

6.1.2. The Raman scattering process

In Raman scattering an absorbed photon excites a molecule to a higher virtual energy state, followed by an immediate re-emission of a photon of a wavelength different from the wavelength of the incident photon. It is a very quick process (much faster than fluorescence), occurring on a time scale of picoseconds. There are two forms of Raman scattering, Stokes and anti-Stokes scattering. When Stokes scattering occurs the re-emitted photon is of a longer wavelength than the initial photon. The molecule remains in an excited state, retaining the energy difference as vibrational energy. When the molecule is initially in an excited state, the emitted photon can possess a larger amount of energy than the absorbed photon, i.e. be of a shorter wavelength. This process is called anti-Stokes scattering and is insignificant at temperatures of liquid water. The wavelength of Raman-scattered photons is independent from the incoming photon and corresponds to the difference between the virtual energy level and the energy level of the molecule post-emission (Fig. 6.2).

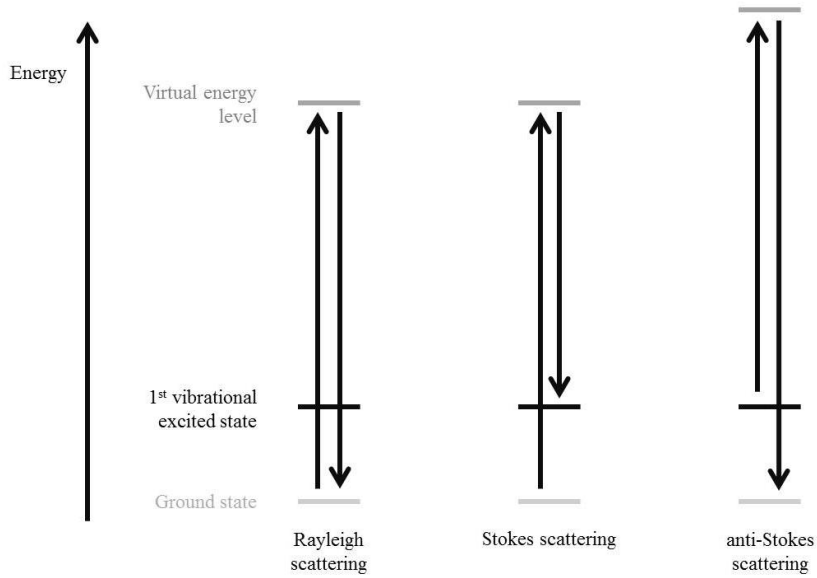

Fig. 6.2 Energy transition during different kinds of light scattering: elastic (Rayleigh scattering) and inelastic scattering (Raman scattering – Stokes and anti-Stokes). The energy difference between the incident photon and the emitted photon corresponds to the energy difference between ground state and the first vibrational excited state.

Marine scientists observed the effects of Raman scattering by water molecules in the early 1980s, when they struggled to compute acceptable pure water absorption coefficients from *in situ* measurements of spectral irradiance (e.g. Spitzer and Wernand, 1981, Sugihara *et al.*, 1984). Especially in clear waters with low absorption, where light penetrates into greater depths, Raman scattering has a large effect on the available light at wavelengths > 550 nm (Gordon, 1999, Schroeder *et al.*, 2003, Zhai *et al.*, 2015). Although almost no solar radiation of wavelengths > 550 nm penetrates the water column deeper than a few meters, light is available through Raman scattering from shorter wavelengths (< 550 nm). In these cases, Raman scattering makes up for a large proportion of available light and needs to be considered for RT calculations (Mobley, 1994). Haltrin and Kattawar (1993) described the Raman wavelength re-distribution function in order to incorporate Raman scattering into the RT equation. Measurements of Raman scattering by water molecules are extremely difficult to make and published values on the fraction of Raman scattered to the total scattered light vary strongly (Marshall and Smith, 1990, Kattawar and Xu, 1992, Ge *et al.*, 1993, Haltrin and Kattawar, 1993).

6.1.3. Fluorescence

The process of fluorescence is much slower than Raman scattering, where the absorption of a photon excites the molecule to a virtual energy state and is followed by almost immediate re-mission of a photon of a wavelength different from the absorbed photon. During the fluorescence process, after the absorption of an excitation photon, the excited electron drops to a lower, semi-stable energy state, the excited singlet state, in a series of rapid downward transitions. From this semi-stable state, the molecule then returns to its initial state by re-emitting a photon of a wavelength shorter than the incident photon. Every molecule possesses a finite number of potential excited singlet states and therefore (different from Raman scattering) a finite number of emission wavelengths. The wavelength at which fluorescence by a pure substance is emitted is independent from the excitation wavelength. The strength of the fluorescence emission, however, depends on a combination of the substance's spectral absorption (wavelength dependent) and the quantum yield of fluorescence.

A fluorescence excitation spectrum therefore has a similar, but not identical, shape to the corresponding absorption spectrum. In order to obtain fluorescence excitation spectra, the intensity of light emitted at a constant wavelength is measured while the excitation

wavelength is varied. Fluorescence emission spectra, on the other hand, describe the intensity of emitted light as function of wavelength for a single excitation wavelength.

A variable fraction of marine CDOM also fluoresces and is therefore called FDOM. The portion of FDOM to CDOM can vary globally by a factor of 3 (Blough and Del Vecchio, 2002). As fluorescence techniques are generally more sensitive than absorption techniques, they are often used to determine the amount of CDOM in a waterbody (Green and Blough, 1994). However, CDOM fluorescence yields are known to be highly variable but very little quantitative data are available (Andrew *et al.*, 2013). The combination of fluorescence excitation and emission spectra can provide details on its chemical composition (Coble *et al.*, 1990). CDOM is a mixture of different molecules and excitation and emission peaks are broad and vary depending on chemical composition but are typically around 250 – 300 nm and 370 – 460 nm, respectively (Coble, 2007). In the visible spectrum CDOM fluorescence can be excited with blue light, resulting in re-emission in the blue/green spectral region.

In a living phytoplankton cell, light is absorbed by the antenna pigments and transferred to a complex chlorophyll *a* molecule which is the final acceptor pigment in photosynthetic reaction centres. *In vivo*, up to 35% of the total energy absorbed is used for photosynthetic activity, 2-5% is emitted as fluorescence, whereas the rest is dissipated as heat (Krause and Weis, 1991). At room temperature, approx. 95% of the *in vivo* fluorescence in phytoplankton originates from the chlorophyll *a* molecule bound to photosystem II (PSII). Chlorophyll *a* fluorescence of PSII is, therefore, an indicator of the efficiency of light-harvesting and utilization (Butler, 1978). Hence, fluorescence excitation spectra, measured at the *in vivo* emission peak of chlorophyll *a* centred at 685 nm, can provide information on the pigment composition of the light-harvesting complex of PSII (Neori *et al.*, 1986, Johnsen and Sakshaug, 2007).

The strength of *in vivo* fluorescence is dependent on the physiological state of the algae. Light-absorbing pigments which are not transferring energy to the reaction centres may also re-emit light and contribute to the specific fluorescence emission signature of a phytoplankton class. Fluorescence excitation emission matrices (FEEMs) can be used to characterise the fluorescence properties of a sample in great detail and enable identification of pigment composition and phytoplankton classes (Yentsch and Yentsch, 1979). Fluorescence excitation spectra can help provide information on photo-adaptation (Mitchell and Kiefer, 1984) and the action spectrum for oxygen evolution, i.e. photosynthesis (Neori *et al.*, 1986).

6.2. Determination of fluorescence excitation emission matrices

6.2.1. Experimental set-up and methods

In order to assess which inelastic signatures can be measured inside the PSICAM integrating cavity, the regular set-up was altered, replacing the tungsten lamp with a tuneable light source consisting of a supercontinuum laser (SuperK Extreme EXB-4) and a linear variable filter unit (SuperK Varia; both NKT Photonics, Denmark). All other components, including optical fibres and the diffuse light bulb, remained unchanged.

Measurements were conducted for a series of 10 nm (FWHM) excitation wavebands centred every 10 nm from 425 -705 nm. Narrower wavebands were found to be unfeasible even though they would have been desirable, because they required significantly longer integration times. At wavelengths shorter than 420 nm, signals dropped to a critical level due to an extremely low output of the laser. Both the laser and the detector were allowed to warm up and stabilise for at least 1 hour before the first measurement was taken. The experiments were conducted in a temperature controlled laboratory and temperature changes and their effect on laser, detector or sample were considered negligible. For each excitation wavelength, 1000 spectra were recorded and averaged to obtain a final intensity spectrum. Integration time and output of the laser were adjusted manually for each waveband so that the excitation peak returned a maximum signal of about 50,000 counts. All recorded spectra were normalised to the measured maximum peak value and inelastic scattering signals were evaluated relative to this maximum.

Dark signal spectra were measured for at least 5 different integration times at the end of each FEEM measurement. They were used to monitor the stability of the detector before, during and after each experiment and were found to be spectrally flat and stable (95% were within ± 3.5%) over the course of an experiment (approx. 5.5 hours). Due to time constrains it was not possible to measure a dark spectrum for every excitation waveband. Hence, the signal at 350 nm was subtracted as constant offset to correct for the dark signal.

The stability of the laser/detector system was tested at three different excitation wavelengths, 450 nm, 550 nm and 650 nm, and the maximum peak signal was found to vary < 1.2% (standard deviation) over 30 mins (Fig. 6.3). The baseline, i.e. signals outside the excitation peak, was generally a small fraction (generally < 10^{-4}) of the signal measured at the

excitation wavelength. 95% of all data measured at 350 nm were within 2.6%, corresponding to a variability of < 20 counts, of the mean value independent from the excitation wavelengths. The variability outside the excitation peak is therefore sufficiently low to consider any signal greater than 10^{-4} of the initial peak signal to represent inelastic scattering effects.

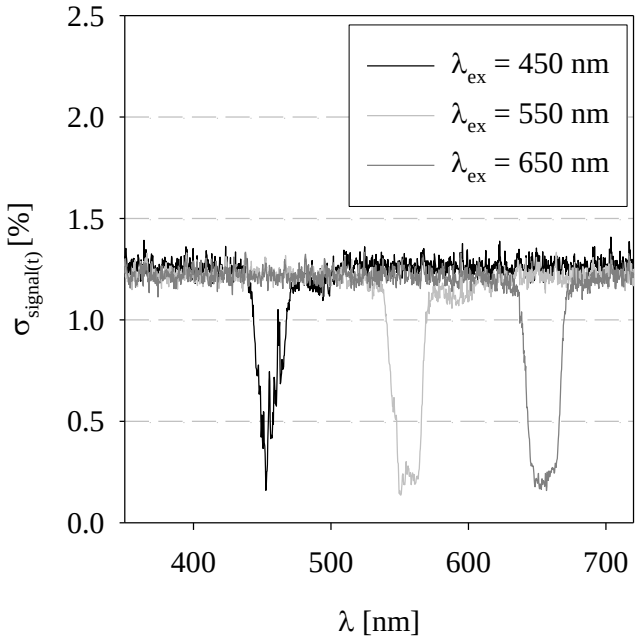

Fig. 6.3 Spectral percentage standard deviation of signals measured for three different wavelengths, 450 nm, 550 nm and 650 nm over the course of 30 minutes as a measure of the stability of the laser/detector system.

6.2.2. Background

Fig. 6.4 shows the illumination matrix used for this experiment, with the excitation wavelengths on the ordinate and the measured wavelengths on the abscissa. Measurements were made pointing the laser straight at the end of the fibre optic guiding light to the detector. The matrix represents the background on which inelastic scattering effects will be superimposed and shows all features of the illumination/detector system.

The signature was dominated by the diagonal line formed from the signal peaks of the excitation wavebands. A shoulder of signals up to 10^{-3}, i.e. 0.1%, of the peak signal was observed for all wavebands, shifted 30 nm towards longer wavelengths from the centre of the

excitation waveband. The source of this shoulder remains unknown but most likely originated from straylight or imperfections in the variable filter unit. Internal straylight errors in the Avantes detector could be ruled out as potential source for this feature based on experiments conducted in the past which used a double-monochromator with better control over spectral output (Lefering, 2012). No other significant spectral features due to straylight in the laser or spectrometer were detected, with background signal levels of generally less than 0.01% (10^{-4}) of the peak signal.

When the cavity is filled with a sample, measured intensities decrease because a portion of the incident light is absorbed. Measured peak signals then represent the amount of light transmitted. The apparent background signal in the matrix increases because of longer integration times, necessary to compensate for the light loss due to absorption by the sample, and subsequent normalisation to the maximum peak value. The background signal level is, therefore, dependent on the concentration of absorbing constituents. Inelastic scattering effects, although also convoluted with the strength of absorption, will appear as elevated signals, i.e. relatively higher than the background and can be identified easily.

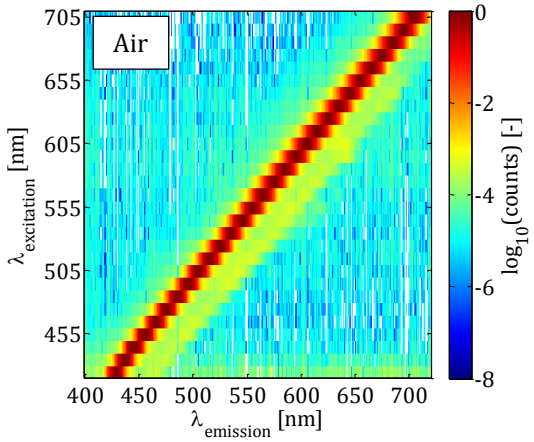

Fig. 6.4 Fluorescence excitation emission matrix representing the baseline for the inelastic scattering measurements, showing all spectral features associated with the set-up (detector, filter, laser) measured outside the cavity. Centres of illumination peaks are plotted on the ordinate against the detector response on the abscissa. Measured signals are normalised to the maximum of the excitation peak and indicated in colour.

6.2.3. Raman scattering in purified water

Raman scattering by water molecules is the only type of inelastic scattering present in purified water samples. Raman scattering makes up to ~ 0.1% of the transmitted excitation

signal and decreases with excitation wavelength. The highest signal due to Raman scattering was measured for excitation at 425 nm.

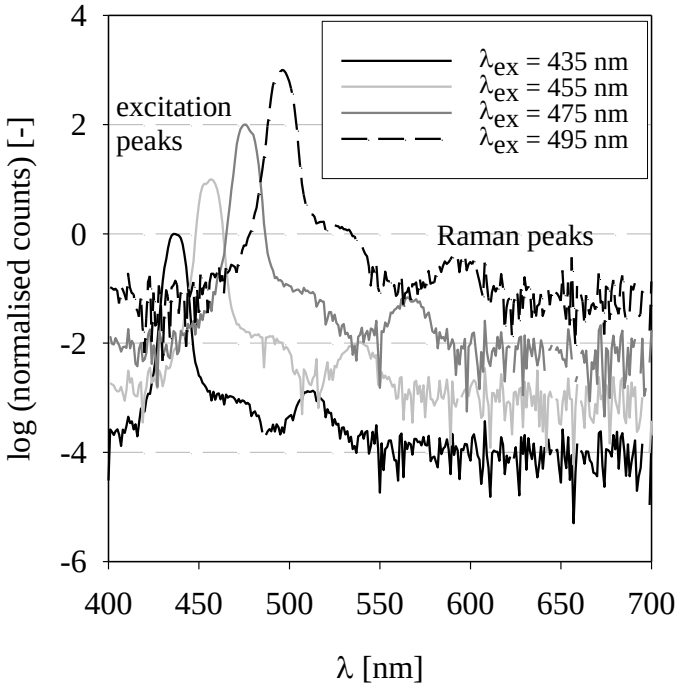

Fig. 6.5 Emission spectra showing the effect of Raman scattering in purified water measured for selected excitation wavelengths. Measurements for excitation at 455 nm, 475 nm and 495 nm are offset for clarity by +1, +2 and +3, respectively.

Table 6.1 Excitation wavelengths and corresponding wavelengths at which the Raman peak is centred.

excitation [nm]	Raman peak [nm]
425	500
445	525
465	550
485	580
505	610
525	640

Fig. 6.5 shows a series of fluorescence emission spectra for excitation wavebands centred at 435 nm, 455 nm, 475 nm and 495 nm, showing that with increasing excitation wavelength, the Raman peak shifts further away from the excitation peak and becomes less distinct (Table 6.1). In the FEEM, Raman peaks became apparent as a line coming off the main diagonal at an angle (Fig. 6.6(a)). Due to the increasing absorption by water and, hence, background signal, the Raman peak cannot be identified for excitation above 525 nm with the set-up used here. A detector with a higher sensitivity or a light source with higher output, however, is expected to be able to resolve the Raman peak for excitation beyond 525 nm.

6.2.4. CDOM fluorescence

A CDOM sample was prepared by filtering a *P. tricornutum* culture sample through a 0.2 µm pore size filter under low vacuum. The corresponding FEEM shows CDOM fluorescence signals between 500 – 600 nm and for excitation up to 495 nm (Fig. 6.6(b)). No significant dependence of the spectral shape and strength of these emission features on the excitation wavelengths could be observed. Signals due to CDOM fluorescence were as strong as 0.1% - 1% of the transmitted excitation signal and clearly distinguishable from the background level of $< 10^{-4}$. The Raman scattering signature was also clearly visible, overlaying the CDOM fluorescence shoulder.

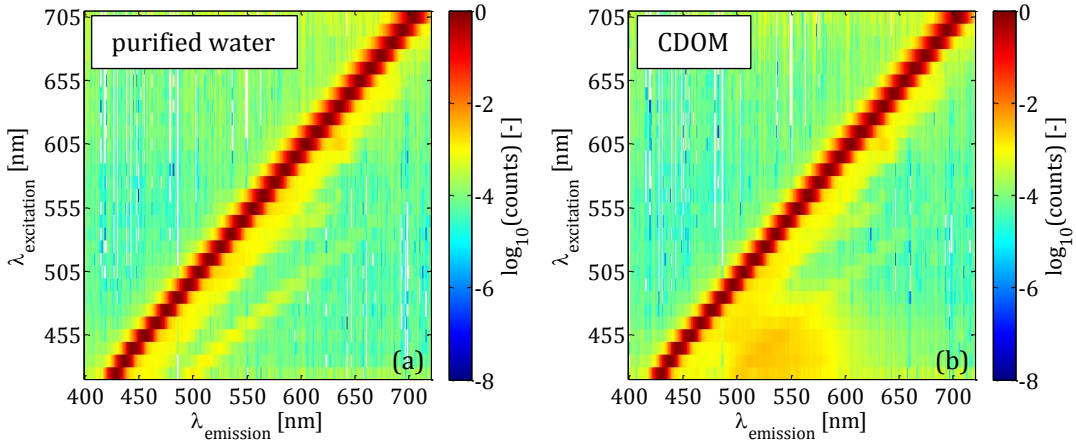

Fig. 6.6 Fluorescence excitation emission matrices for measurements of (a) purified water and (b) a CDOM sample. Centres of excitation waveband peaks are plotted on the ordinate against the detector response (emission wavelength) on the abscissa. Measured signals are normalised to the maximum of the excitation peak and indicated in colour.

6.2.5. Inelastic scattering signatures of different algal cultures

FEEMs were determined for dilute algal culture samples from 4 different species: *A. maxima*, *D. maritima*, *P. tricornutum* and *Synechococcus sp.* (Table 2.2). Overall signal levels varied depending on the strength of absorption of the different samples but inelastic scattering signals were typically one magnitude higher than the background. In addition to Raman scattering and CDOM fluorescence, phytoplankton pigment fluorescence was observed.

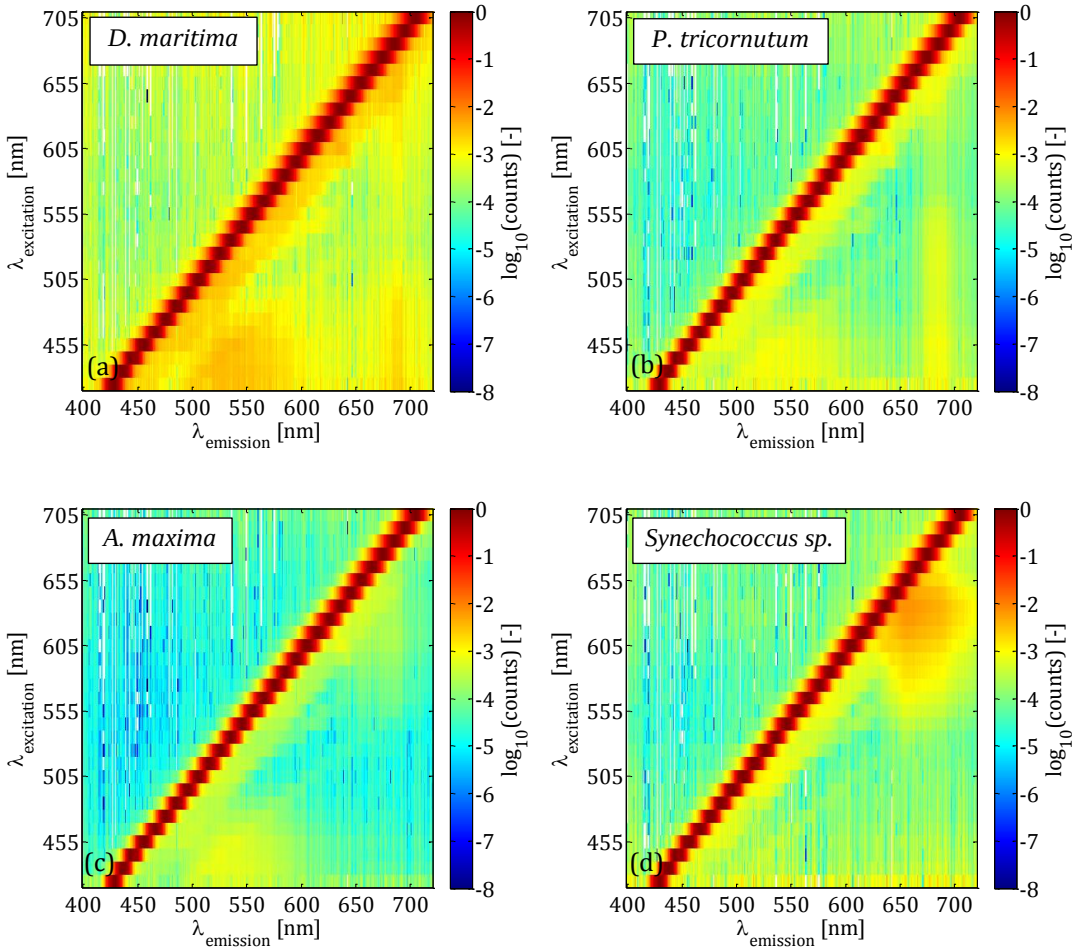

Fig. 6.7 Fluorescence emission excitation matrices of algal culture samples from 4 different species, (a) *D. maritima* and (b) *P. tricornutum*, (c) *A. maxima* and (d) *Synechococcus sp.*. Measured signals are normalised to the maximum of the excitation peak and indicated in colour.

Both the green algae, *D. maritima* (Fig. 6.7(a)), and the diatom, *P. tricornutum* (Fig. 6.6(b)), showed the chlorophyll *a* fluorescence peak centred around 685 nm after excitation from 425 – 675 nm. The intensity of chlorophyll fluorescence emitted was dependent on the spectral absorption and followed the spectral shape of the species specific absorption spectrum with highest intensity for excitation around the blue chlorophyll absorption peak (Fig. 6.8). In contrast, the two cyanobacteria samples from *A. maxima* and *Synechococcus sp*. cultures only exhibited pigment fluorescence for excitation wavelengths longer than 550 nm. In cyanobacteria, most chlorophyll *a* is associated with the non-fluorescing PSI (Bryant, 1986). Only a small portion chlorophyll *a* is connected to PSII and does not play a major role in light-harvesting which is why the dominant chlorophyll *a* fluorescence peak is absent for excitation in the blue/green (Gantt, 1977). Fluorescence by cyanobacteria emitted in the red originates from auxiliary pigments, typically phycobiliproteins, which absorb most of the light used for photosynthesis.

A. maxima (Fig. 6.7(c)) showed fluorescence by phycocyanin which is strongest around 650 nm after excitation at 620 nm (Glazer, 1977) and *Synechococcus sp.* (Fig. 6.7(d)) overall exhibited much stronger fluorescence emission compared to *A. maxima* between 600 - 710 nm for excitation at wavelengths longer than 560 nm. This is potentially due to differences in cell concentration and strength of absorption but remains unknown because no absorption data were available for this particular sample. CDOM fluorescence does not occur in the *Synechococcus sp.* sample because this culture was diluted in distilled water and is therefore lacking organic components of artificial sea water which are the main driver for CDOM fluorescence observed in the marine algae samples. Results presented here are in agreement with previous observations (Seppala *et al.*, 2007, Simis *et al.*, 2012) which showed that the emission by cyanobacteria from 600-690 nm is a combination of fluorescence by Phycocyanin (600 -643 nm) allophycocyanin (655-663 nm) and chlorophyll *a* (682-685 nm).

6.2.6. Fluorescence excitation spectra

Measurements of the fluorescence excitation at 685 nm can provide additional information on the absorption properties of phytoplankton pigments and their role in photosynthesis. The comparison of absorption and fluorescence excitation spectra can help to identify light-harvesting and photo-protective pigments. When light of a certain wavelength is absorbed by light-harvesting pigments, it will trigger chlorophyll *a* fluorescence. *In vivo* fluorescence excitation spectra measured at 685 nm, however, do not respond to absorption by photo-protective pigments (Johnsen and Sakshaug, 2007).

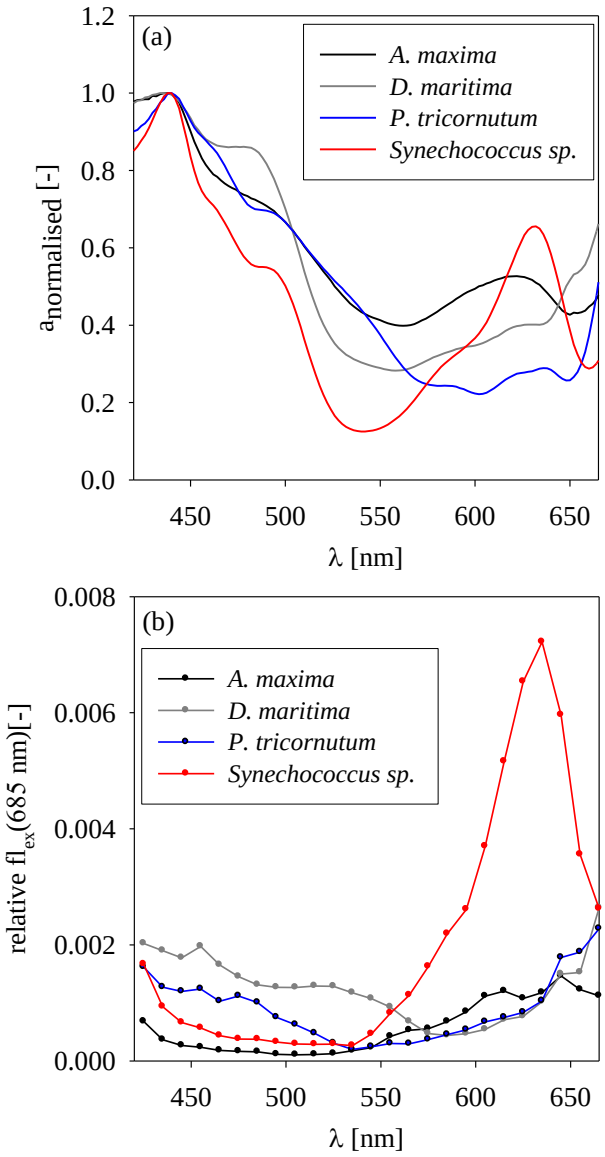

Fig. 6.8 (a) Spectral algal absorption and (b) relative fluorescence excitation for 4 cultured algal species. Absorption spectra were normalised to their maximum signal at 440 nm. Fluorescence excitation spectra were determined with 10 nm resolution and normalised to the signal measured at 685 nm.

Fig. 6.8 shows absorption spectra of the 4 phytoplankton species, which were all dominated by the blue chlorophyll peak. Spectra were normalised to the signal at 440 nm to reduce concentration effects. However, excitation at wavelengths shorter than 530 nm predominantly triggers chlorophyll *a* fluorescence emission in the green algae and diatoms whereas in the cyanobacteria, *A. maxima* and *Synechococcus sp.*, fluorescence is mainly triggered by excitation between 550 – 650 nm. This corresponds to the absorption peak of

phycobiliproteins which is the major photosynthetically relevant pigment group in cyanobacteria, transferring energy to the fluorescing chlorophyll bound to PSII. In cyanobacteria, most of the absorbing chlorophyll which is apparent in the absorption spectrum is bound to PSI and therefore doesn't contribute to chlorophyll fluorescence emission at 685 nm.

The fluorescence excitation spectra of *P. tricornutum* and *D. maritima* also reflect the phytoplankton group specific auxiliary pigments involved in light-harvesting, shaping the absorption spectrum between 480 and 580 nm. Green algae typically contain violaxanthin (Jeffrey, 1968) which absorbs around 415 - 466 nm (Ruban *et al.*, 2001) while diatoms use fucoxanthin to broaden their blue/green absorption peak (460 - 570 nm) (Stauber and Jeffrey, 1988, Mimuro and Akimoto, 2003).

6.2.7. Significance for PSICAM measurements

Detected fluorescence signals were between 0.1% - 1% of measured transmitted signals (50,000 counts) and are potentially sufficiently strong to explain some of the previously observed mis-match between PSICAM and LWCC absorption data (Fig. 6.1). CDOM fluorescence emission was generally as strong as the measured chlorophyll *a* fluorescence suggesting there is a need for the implementation of CDOM fluorescence corrections into PSICAM measurements.

The set-up tested here was able to demonstrate the potential benefits of a double-monochromatic absorption/fluorescence measurement system which would enable the collection of additional valuable information on, for example the origin of dissolved organic matter, which can be gained from FEEMs (Coble *et al.*, 1990) and identification of photosynthetically relevant pigments (Mitchell and Kiefer, 1984, Mitchell and Kiefer, 1988). Monochromatic illumination also enables spectrally resolved quantification of fluorescence signals, required for appropriate correction for fluorescence effects on absorption measurements. Development of such corrections would lead to an improvement in the accuracy of quantitative absorption data derived from PSICAM measurements.

6.2.8. Implications for bio-optical models

With its ability to measure spectral absorption and spectral fluorescence properties of a discrete water sample simultaneously, the set-up tested here potentially has great implications for novel applications. Complimentary absorption/fluorescence data can be used

for primary production studies through parameterisation photochemical models (Yentsch and Yentsch, 1979, Johnsen and Sakshaug, 2007). Double-monochromatic measurement systems therefore have the potential to improve our understanding of the links between light harvesting and utilisation by marine algae. Spectral data on the absorption and fluorescence properties of marine algae can be helpful to identify the role of individual pigment groups within the photosynthetic process.

6.3. Inelastic effects in white light PSICAM measurements

Section 6.2 showed that inelastic scattering effects can be detected inside a PSICAM and that signals can reach up to ~ 1% of the transmitted excitation light. This points towards a need to quantify errors in absorption measurements due to fluorescence effects. Detection and correction of fluorescence effects are extremely challenging when a broadband light source is used and fluorescence signatures are difficult to separate out. This section will investigate the extent to which inelastic scattering processes might affect traditional PSICAM absorption measurements with a white light source.

6.3.1. Methods

In order to gain better control over inelastic effects in regular PSICAM measurements, a series of 5 cut-off filters were mounted on a filter wheel in front of the CF1000 tungsten lamp. Light intensities inside the cavity were measured for white light illumination and for the different filters cutting off the spectrum at 450 nm, 500 nm, 550 nm, 600 nm and 650 nm, for three algal cultures samples, *A. maxima*, *D. maritima* and *P. tricornutum*. Dark counts were measured twice, immediately after illumination with white light as well as at the end of the filter series. The average of these two measurements was then subtracted from each intensity spectrum.

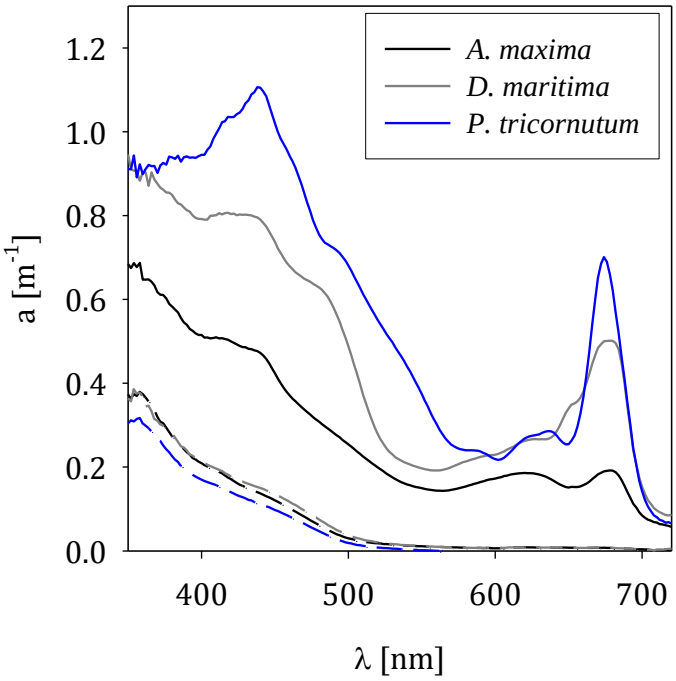

Fig. 6.9 Total absorption (solid lines) and CDOM absorption (dashed lines) spectra of algal culture samples from three different species

Fig. 6.9 shows the total absorption and CDOM absorption spectra of the samples used for this part of the study. The cyanobacteria, *A. maxima*, had lower particulate absorption compared to the samples from other cultured species. The magnitude of CDOM absorption, however, varied considerably less between the different samples. Results showed that it was not possible to resolve Raman scattering features using this experimental configuration with broadband illumination.

6.3.2. Phytoplankton fluorescence signals

For the three samples shown in Fig. 6.9, corresponding fluorescence signals were determined. Signals due to fluorescence are observed as increase in intensity when the cavity is filled with a sample compared to purified water, at wavelengths where the incident illumination is cut off by a filter.

Measurements with the 550 nm and 600 nm cut-off filters revealed the chlorophyll fluorescence peak centred at 685 nm for *P. tricornutum* and *D. maritima* (Fig. 6.10 (b) and (c)). For measurements with the 600 nm filter, the cyanobacteria, *A. maxima*, exhibited a

broad shoulder from ~ 640 – 730 nm rather than a distinct peak (Fig. 6.10 (a)). Using the 600 nm cut-off filter resulted in slightly higher maximum signals compared to the 550 nm filter for the diatom and green algae sample because cells were provided with more light to trigger fluorescence. The 650 nm cut-off filter partially masked the chlorophyll fluorescence peak and was therefore excluded from further analysis. *P. tricornutum* exhibited a fluorescence peak signal of 316 counts at 683 nm, accounting for 3.4% of the initial (unfiltered) signal. This fluorescence signal would lead to an underestimation of absorption of ~ 0.04 m^{-1}, corresponding to ~ 10% of the absorption coefficient measured for the diatom culture at 684 nm (Fig. 6.11 (a) and (b)). The second chlorophyll fluorescence peak located in the NIR makes up for an even larger portion (20% - 140%) of the absorption signal at wavelengths > 700 nm. Chlorophyll fluorescence occurring in *D. maritima* and *A. maxima* resulted in consistently lower errors in the absorption measurements of < 20%.

The difference between fluorescence signals measured with the 550 nm and 600 nm filters was significantly larger for *A. maxima* than for the other species because more fluorescence is triggered by excitation between 550 nm and 600 nm in cyanobacteria compared to other algal groups, which can also be observed in fluorescence excitation spectra (Fig. 6.8).

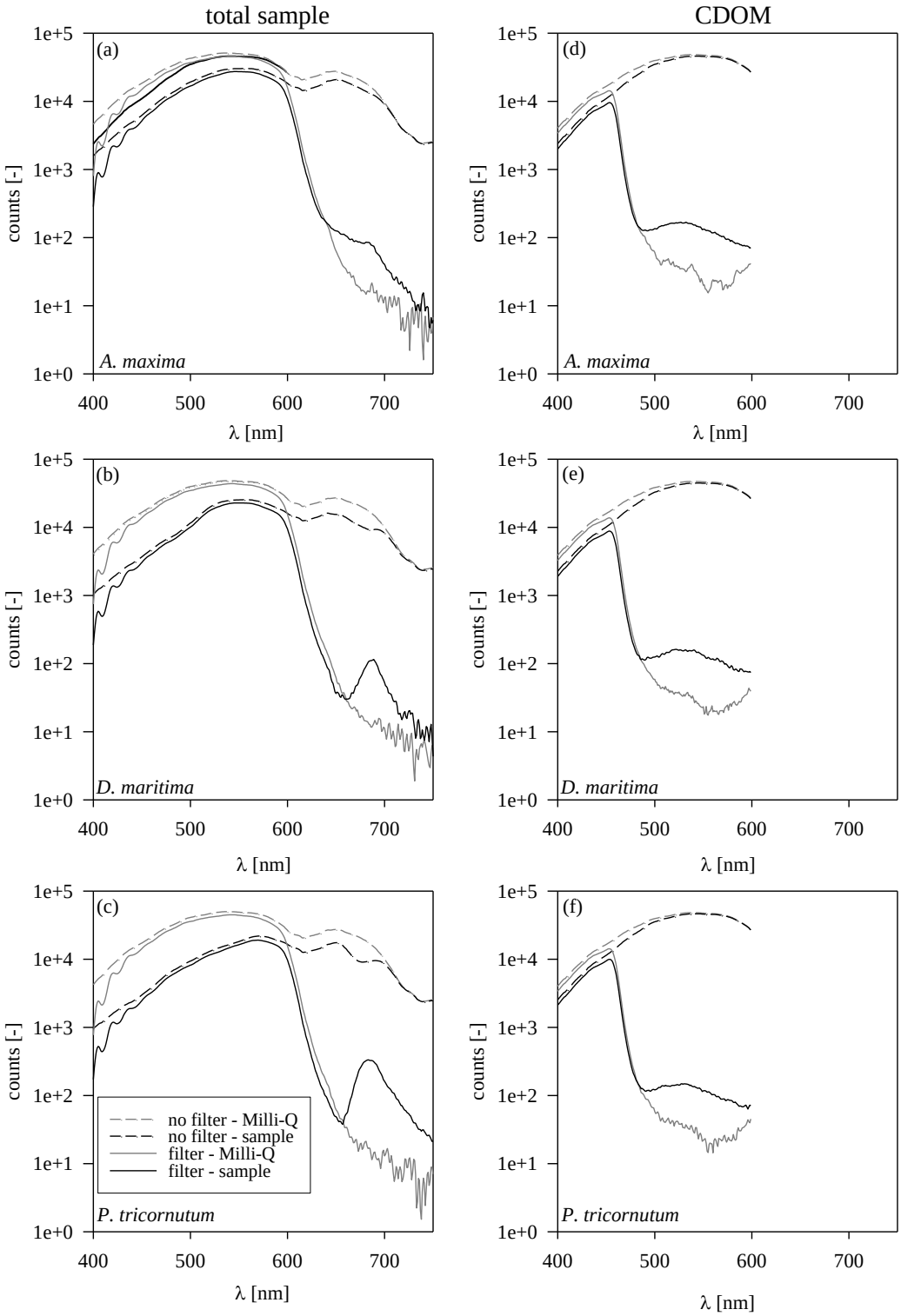

Fig. 6.10 Spectral intensity measured inside the PSICAM when filled with the reference (purified water, grey lines) and a sample (black lines). Left: unfiltered sample made up from three algal cultures: (a) *D. maritima* and (b) *P. tricornutum* and (c) *A. maxima*, with a 600 nm cut-off filter (solid lines) and when no filter is in place (dotted lines); right: (d) – (f) CDOM spectra of the same cultures measured using a 450 nm cut-off filter.

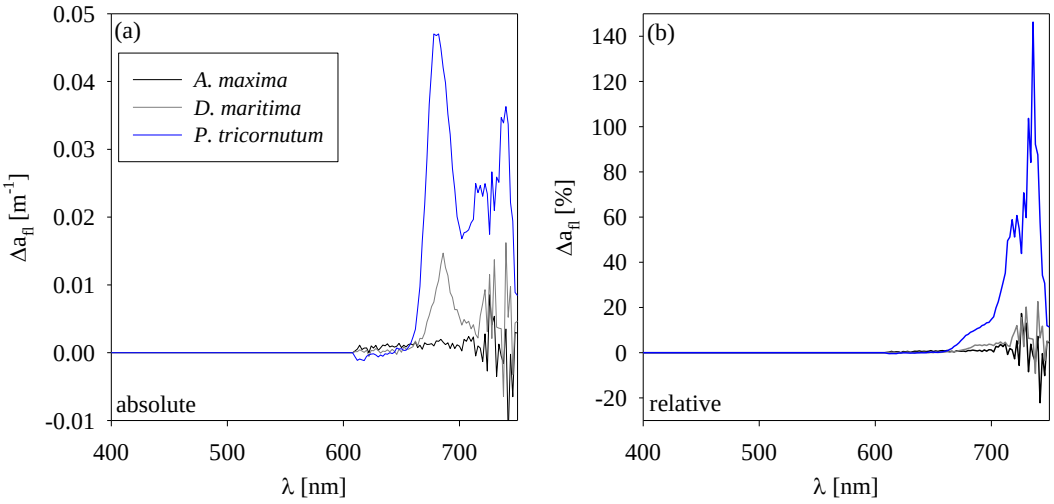

Fig. 6.11 Errors in PSICAM absorption measurements of three different phytoplankton cultures caused by sample fluorescence. Absolute errors in (a) total absorption and (b) corresponding relative errors.

6.3.3. Detection of CDOM fluorescence

No CDOM fluorescence could be detected in measurements of artificial CDOM samples made up from humic acid crystals dissolved in purified water. It was also difficult to measure CDOM fluorescence signals for untreated, i.e. not 0.2 µm filtered, culture samples where fluorescence typically accounted for less than 0.1% of the signal measured under white light illumination (data not shown). Filtration increased the strength and thereby improved the detection of CDOM fluorescence signals, presumably because other absorbing material was removed from the sample and less of the emitted fluorescence is re-absorbed.

In experiments with filtered algal cultures, CDOM fluorescence was observed as a broad shoulder, between 500 and 600 nm, for measurements with the 450 nm (Fig. 6.10(d) – (f)) and 500 nm cut-off filters. The latter resulted in higher fluorescence signals, but did not fully resolve the left edge of the shoulder. The choice of filter to use for future correction of CDOM fluorescence is therefore non-trivial because while a 450 nm cut-off filter does capture the whole fluorescence feature, this measurement does not exhibit maximum fluorescence at all wavelengths. The strength of CDOM absorption and corresponding fluorescence was similar for all three samples (Fig. 6.9). For both the 450 nm and the 500 nm filter, measured CDOM fluorescence signals at 535 nm were less than ~ 0.4% and ~ 0.8% of the initial signal, respectively. CDOM fluorescence resulted in much smaller absolute errors in the absorption measurements (< 0.003 m^{-1}; Fig. 6.12 (a)). On average, this

represents ~ 20% of the absorption coefficient at green wavelengths for all three cultures studied here (Fig. 6.12(b)).

A correction for CDOM fluorescence will be more complex than the correction of chlorophyll fluorescence effects because CDOM fluorescence emission is much more dependent on the excitation wavelength. It is extremely difficult to de-convolute absorption and fluorescence signals especially when non-monochromatic illumination is used. A double monochromatic system is therefore recommended to achieve better control over inelastic scattering effects inside a PSICAM and to enable the development of a CDOM fluorescence correction.

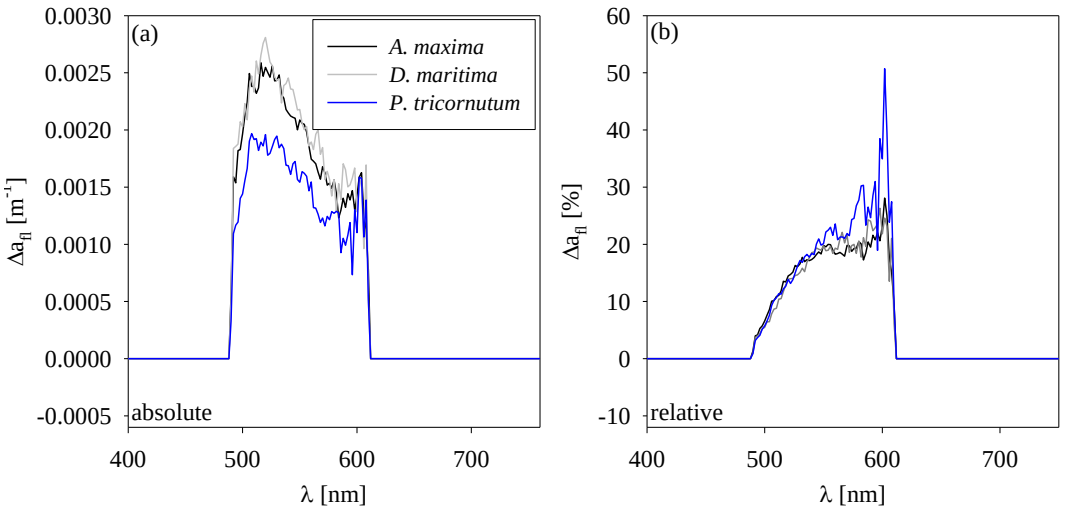

Fig. 6.12 Errors in PSICAM absorption measurements of three different algal cultures caused by sample fluorescence. Absolute errors in (a) CDOM absorption and (b) corresponding relative errors.

6.4. Conclusions

The impact of inelastic scattering effects in natural water samples on measurements of spectral absorption coefficients with a PSICAM was assessed in this chapter. Previous studies have shown that chlorophyll fluorescence at red wavelengths can result in measurement artefacts and appropriate corrections have been implemented in routine measurements (Röttgers *et al.*, 2007). However, to date, no work has been published showing the extent to which CDOM fluorescence or Raman scattering affect absorption measurements in a PSICAM. Measurements inside an integrating cavity are potentially more

susceptible to fluorescence emission than other absorption techniques due to amplification of inelastic scattering effects.

This chapter has demonstrated that Raman scattering, CDOM fluorescence and chlorophyll fluorescence can be detected when using scanning, narrow waveband illumination. Measured signals were sufficiently high to have the potential to significantly impact the accuracy of PSICAM absorption data.

A second set-up closer to the original white light PSICAM configuration showed that CDOM fluorescence signals were about 2 - 6 fold smaller than chlorophyll fluorescence signals. However, both types of fluorescence would result in on average 10 - 20% underestimation of PSICAM absorption coefficients at emission wavelengths. Appropriate corrections for both types of fluorescence will be required to improve the quality of PSICAM data. Results, however, also showed the difficulties of de-convoluting simultaneously measured fluorescence and absorption signals, when using broadband illumination. Routinely measuring spectrally resolved fluorescence excitation emission matrices is recommended to achieve best control over all measurement parameters.

This study has also demonstrated that measurements made with a double-monochromatic system (monochromatic illumination and wavelength resolved detection) can provide additional useful information on the photosynthetic capabilities of marine algae. The combination of absorption, fluorescence emission and fluorescence excitation spectra, allows identification of pigments involved in the utilisation of light which is useful for parameterisation of primary productivity models (Yentsch and Yentsch, 1979, Johnsen and Sakshaug, 2007).

7. Summary and conclusions

The aim of this project was to assess the performance of different methods to measure a variety of spectral absorption characteristics of natural waters and improve the overall quality of collected absorption data. Accurate knowledge of the absorption of light in the oceans is important for our understanding of many biogeochemical and physical processes in the marine environment, such as solar heating, the fate of organic carbon stored in the ocean and on the amount of light available and harvested for primary production by marine algae.

This study focussed on the performance of absorption measurements inside an integrating cavity, using a point-source integrating cavity absorption meter, the PSICAM. The PSICAM has previously been shown to measure absorption data accurately even in highly scattering waters which makes it well-suited to investigate absorption by natural water samples (Röttgers *et al.*, 2005). The concept of the PSICAM was proposed by Kirk (1997) but, to date, the instrument has not been routinely used by the broader community to measure absorption by natural waters because measurements and calibration have proven laborious and non-trivial. However, the potential of measurements made inside an integrating sphere to improve the quality of absorption data of the marine environment has been acknowledged and instruments are commercially available now (e.g. Trios OSCAR, the HOBI labs a-Sphere and the Turner Designs flow through ICAM). This provides a great opportunity for optical oceanographers to routinely collect accurate absorption data with significant implications for the development and validation of ocean colour remote sensing algorithms. The general approach used in this work was to compare commonly used absorption measurement techniques against data measured with the PSICAM, focussing primarily on measurements of discrete samples but also considering implications for *in situ* measurements and RT modelling.

In this work, the performance of the PSICAM set-up developed by Röttgers and co-workers (Röttgers *et al.*, 2005) has been tested, regarding accuracy and precision (Chapter 3). This was done by comparison with two standard absorption measurement techniques, using a long-pathlength LWCC system and a dual-beam spectrophotometer. Absorption measurements from coloured solutions have shown that the PSICAM is as least as accurate and sensitive as the other two methods. It has been confirmed that the addition of scattering

material to a sample has virtually no effect on the transmission measured in a PSICAM, whilst at the same time reducing the transmission measured in a dual-beam spectrophotometer dramatically, by up to 80% of the initial signal. A sensitivity analysis has confirmed previous findings, identifying the errors in the calibration process as major contributors to PSICAM measurement uncertainties. New performance issues have been observed at the edges of the visible spectrum where intensity levels inside the integrating cavity drop to a critical level, resulting in absorption data of limited quality. Cross-validation with filter pad absorption data has revealed that particularly in the blue/UV the quality of PSICAM data can be limited. Filter pad absorption measurements (T-method) can produce accurate particulate absorption coefficients for these wavelengths where sensitivity issues in PSICAM measurements are observed (Chapter 4).

Filter pad absorption measurements themselves, however, are subject to two major sources of experimental uncertainty: the so called pathlength amplification factor, β, and scattering offsets for which previous null-correction approaches have to be questioned after recent observations of non-zero absorption in the NIR (Tassan and Ferrari, 2003, Röttgers and Gehnke, 2012). The comparison of PSICAM and filter pad data presented in Chapter 4 has revealed linear relationships that vary on a sample-by-sample basis. This suggests that previously observed non-linear relationships were due to artefacts in the determination of suspension absorption data with instruments other than a PSICAM. Inaccurate validation data were potentially limiting factors in the development of appropriate filter pad absorption measurement corrections in the past. Linear regression against PSICAM absorption data can be used to correct filter pad absorption data by simultaneously resolving both β and the NIR offset (McKee *et al.*, 2014). This regression approach has provided significantly improved agreement with PSICAM data (3.2% RMS%E) compared to previously published filter pad absorption corrections with RMS%E > 20%. Results presented here have shown that direct transmittance (T-method) filter pad absorption measurements perform essentially at the same level as more complex geometrical configurations, based on integrating cavity measurements (IS-method and QFT-ICAM) because the linear regression correction effectively compensates for the sensitivity to scattering errors in the T-method. A major finding of the thesis is that the combination of filter pad technique and PSICAM can be used to generate best quality particulate absorption data as it enables correction of error sources associated with both measurements.

The PSICAM was used in the past to develop two new correction methods for *in situ* absorption measurements with an AC-9 absorption and attenuation meter (McKee *et al.*,

2013, Röttgers *et al.*, 2013). The new corrections are expected to perform significantly better than earlier approaches, particularly in turbid coastal waters. Optical closure, a test for consistency between RT modelled and measured underwater light fields, was used in Chapter 5 to evaluate the performance of these new correction methods relative to the most commonly applied correction (Zaneveld *et al.*, 1994). For the datasets available here, the selection of AC-9 scattering correction did not have a significant impact on the degree of optical closure, which has been attributed to the nature of the mainly clear and only moderately turbid stations. Results for two stations with increased scattering sampled in a coccolithophore bloom, however, have suggested that there might be still unresolved issues with either *in situ* IOP or radiometry measurements or the parameterisation of the RT model (e.g. unresolved features in the angular shape of the VSF). The agreement between modelled and measured values can also be used to assess our ability to model underwater light fields based on *in situ* IOP measurements. Data from RT models are valuable for the interpretation of ocean colour remote sensing signals and the development of spectrally resolved models of primary productivity (Sathyendranath *et al.*, 1989, Smith *et al.*, 1989). The latter often use the photosynthetically available radiation (*PAR*) as an input parameter. Results presented here have shown an agreement between modelled and measured PAR of 15% - 24% (RMS%E) for all corrections and datasets. The radiance reflectance, R_L, which can be used as a proxy for remote sensing reflectance signals, has shown slightly lower agreement with RMS%E up to 33%. The achieved degree of optical closure has also indirectly demonstrated the accuracy of PSICAM measurements.

In order to further improve quantitative absorption measurements made with a PSICAM potential measurement errors due to inelastic scattering effects inside the cavity have been investigated in Chapter 6. Using narrow bandwidth illumination, it has been demonstrated that Raman scattering, CDOM fluorescence and chlorophyll fluorescence can be detected inside a PSICAM integrating sphere and that it is possible to gain information on fluorescence characteristics from a PSICAM absorption measurement. The derived fluorescence excitation emission matrices can provide useful additional information on a sample with regards to its pigment composition and its photosynthetic abilities (e.g. Johnsen and Sakshaug, 2007). Observed signals due to inelastic scattering were as strong as 1% of the transmitted excitation signal. Results have also suggested that measurements using monochromatic illumination in combination with fully wavelength resolved intensity measurements inside a PSICAM can improve the quality of PSICAM absorption data. The strength of inelastic scattering signals in the current PSICAM set-up, using a tungsten lamp, has been investigated by implementing a series of cut-off filters. Results have shown that it

is possible to detect CDOM and chlorophyll fluorescence, with signals of up to 3.5% of the initial signal. These fluorescence signals can lead to a 10 - 20% error in PSICAM absorption determinations if not corrected appropriately. Appropriate corrections for inelastic scattering effects are therefore required as inelastic scattering has the potential to significantly impact on the accuracy of PSICAM measurements. Currently, PSICAM data are already corrected for chlorophyll fluorescence effects, reducing the level of unresolved error. There is, however, a need to also develop and implement a correction for CDOM fluorescence. The analysis has also revealed the challenges when trying to de-convolute absorption and fluorescence signals in set-ups where non-monochromatic illumination is used.

In summary, this work has shown that PSICAM measurements can provide accurate absorption data for natural waters containing scattering material. This enables re-assessment and improvement of the performance of commonly used absorption measurements, such as particulate absorption and *in situ* absorption profiles with submersible sensors. It has also been demonstrated how these recent developments positively affect the quality of RT simulations of underwater and water-leaving light fields and of ocean colour remote sensing products. This highlights the need for high quality absorption data in the field of optical oceanography.

This study, however, has also revealed that, in order to obtain high quality absorption data, great effort has to go into the calibration and validation of the PSICAM instrument. This makes the PSICAM rather unattractive for applications in the field where time and labour are limited. The benefits of the PSICAM, however, are crucial for progress in technological development and for the assessment of measurement uncertainties in absorption determinations. For studies where data accuracy and precision are paramount, the advantages of the PSICAM outweigh the requirements regarding time and labour.

Integrating cavity absorption measurement techniques are becoming more accessible to a broader community through availability of commercial sensors. These instruments are designed for *in situ* applications and benefit from reduced sample handling compared to the instrument used here due to their flow through designs. They might therefore have an advantage over the bench-top PSICAM and will potentially increase the amount of high quality absorption data available to the community. However, it remains unknown how challenges in the calibration of these instruments will be overcome. To date, there are no studies reported which assess the performance of these commercial instruments, an application the PSICAM would be well-suited for.

8. Future Work

This work has revealed some remaining issues with absorption techniques which require further investigation/developments to improve the quality of IOP measurements of marine waters:

1) There are remaining sensitivity issues in PSICAM measurements at both ends of the spectrum due to very low intensity signal levels (blue/UV) and unresolved issues with the temperature and salinity correction (NIR). At shorter wavelengths this can potentially be explained by internal straylight errors inside the detector (Röttgers, pers. comm.). These effects need to be quantified and appropriate corrections have to be established. Exchanging the tungsten lamp with another light source providing more light at blue/UV wavelengths can also improve the accuracy of PSICAM data at these wavelengths. Finding a suitable light source might, however, be challenging because UV light sources commonly suffer from limited stability.

2) In the current PSICAM measurement protocol, only chlorophyll fluorescence effects are corrected because these are easy to quantify due to their distinct peak characteristics. This study has shown, however, that other inelastic scattering effects also have the potential to cause inaccuracies in absorption measurements (even though only to a smaller extent). Future work is required to develop and integrate corrections for CDOM fluorescence effects in PSICAM measurement.

3) This work has demonstrated that the development of a system to simultaneously measure spectral absorption and fluorescence characteristics would help to deepen our understanding of links between optical and biological processes occurring in the aquatic environment. A new instrument would require a tuneable monochromatic light source with high output, especially in the UV/blue spectral region as well as a detector with extremely high sensitivity, e.g. a cooled camera. Developing such an absorption/fluorescence measurement with reasonably short acquisition times could potentially be challenging or might only be achievable for limited spectral resolution.

4) The evaluation of performances of the different AC-9 scattering corrections has to be extended to highly turbid environments. The analysis described in this work could, unfortunately, provide only little insight in the performance of new scattering corrections in these extreme cases. However, optical closure in high turbidity waters might be difficult with accuracy in both backscattering and radiometry measurements as limiting factors.

5) The work presented here has shown that a satisfactory level (regression slopes typically within 15%) of optical closure can be reached with current *in situ* IOPs and radiometry measurement capabilities for clear to moderately turbid waters. Remaining discrepancies between RT model and measurements might be due to inappropriate parameterisation of, for example, model boundary conditions. Further investigation is required to understand the complex relationships involved in RT processes and how changing parameterisation has an impact on the quality of modelled underwater and water-leaving light fields.

6) Commercially available ICAM instruments still require thorough testing and assessment of measurement limitations. Having established the PSICAM as viable method to provide accurate validation data, a comparison with these commercial sensors would be very interesting.

7) There is a need for a method to partition algal and non-algal particles in suspension, through either chemical or UV-bleaching. Being able to separate phytoplankton and detritus absorption from PSICAM measurements would provide data for the development and validation of a suitable correction for filter pad measurements.

References

ALLALI, K., BRICAUD, A. & CLAUSTRE, H. 1997. Spatial variations in the chlorophyll-specific absorption coefficients of phytoplankton and photosynthetically active pigments in the equatorial Pacific. *Journal of Geophysical Research-Oceans,* 102**,** 12413-12423.

ANDREW, A. A., DEL VECCHIO, R., SUBRAMANIAM, A. & BLOUGH, N. V. 2013. Chromophoric dissolved organic matter (CDOM) in the Equatorial Atlantic Ocean: Optical properties and their relation to CDOM structure and source. *Marine Chemistry,* 148**,** 33-43.

ANTOINE, D., MOREL, A., LEYMARIE, E., HOUYOU, A., GENTILI, B., VICTORI, S., BUIS, J. P., BUIS, N., MEUNIER, S., CANINI, M., CROZEL, D., FOUGNIE, B. & HENRY, P. 2013. Underwater Radiance Distributions Measured with Miniaturized Multispectral Radiance Cameras. *Journal of Atmospheric and Oceanic Technology,* 30**,** 74-95.

ARBONES, B., FIGUEIRAS, F. G. & ZAPATA, M. 1996. Determination of phytoplankton absorption coefficient in natural seawater samples: Evidence of a unique equation to correct the pathlength amplification on glass fiber filters. *Marine Ecology Progress Series,* 137**,** 293-304.

BABIN, M. & STRAMSKI, D. 2004. Variations in the mass-specific absorption coefficient of mineral particles suspended in water. *Limnology and Oceanography,* 49**,** 756-767.

BEHRENFELD, M. J. & FALKOWSKI, P. G. 1997. A consumer's guide to phytoplankton primary productivity models. *Limnology and Oceanography,* 42**,** 1479-1491.

BLOUGH, N. V. & DEL VECCHIO, R. 2002. Chromophoric DOM in the coastal environment. *In:* HANSELL, D. A. & CARLSON, C. A. (eds.) *Biogeochemistry of Marine Dissolved Organic Matter.* Amsterdam: Academic Press.

BOSS, E., SLADE, W. H., BEHRENFELD, M. & DALL'OLMO, G. 2009. Acceptance angle effects on the beam attenuation in the ocean. *Optics Express,* 17**,** 1535-1550.

BRICAUD, A., BABIN, M., MOREL, A. & CLAUSTRE, H. 1995. Variability in the chlorophyll-specific absorption-coefficients of natural phytoplankton - analysis and parameterization. *Journal of Geophysical Research-Oceans,* 100**,** 13321-13332.

BRICAUD, A., MOREL, A. & PRIEUR, L. 1981. Absorption by dissolved organic matter of the sea (yellow substance) in the UV and visible domains. *Limnology and Oceanography,* 26**,** 43-53.

BRICAUD, A. & STRAMSKI, D. 1990. Spectral absorption coefficients of living phytoplankton and nonalgal biogenous matter: a comparison between the Peru upwelling area and the Sargasso Sea. *Limnology and Oceanography,* 35**,** 562-582.

BRYANT, D. A. 1986. The cyanobacterial photosynthetic apparatus: Comparison to those ofhigher plants and photosynthetic bacteria. *In:* PLATT, T. & LI, W. K. W. (eds.) *Photosynthetic Picoplankton.* San Miniato, Italy: Canadian bulletin of fisheries and aquatic sciences.

BUITEVELD, H., HAKVOORT, J. H. M. & DONZE, M. The optical properties of pure water. Ocean Optics XII, June 13-15 1994 Bergen, Norway. SPIE, 174-183.

BULGARELLI, B., ZIBORDI, G. & BERTHON, J. F. 2003. Measured and modeled radiometric quantities in coastal waters: toward a closure. *Applied Optics,* 42**,** 5365-5381.

BUTLER, W. L. 1978. Energy-distribution in photo-chemical apparatus of photosynthesis. *Annual Review of Plant Physiology and Plant Molecular Biology,* 29**,** 345-378.

CARDER, K. L., HAWES, S. K., BAKER, K. A., SMITH, R. C., STEWARD, R. G. & MITCHELL, B. G. 1991. Reflectance model for quantifying chlorophyll-a in the presence of productivity degradation products. *Journal of Geophysical Research-Oceans,* 96**,** 20599-20611.

CARDER, K. L., STEWARD, R. G., HARVEY, G. R. & ORTNER, P. B. 1989. Marine humic and fulvic acids - their effect on remote-sensing of ocean chlorophyll. *Limnology and Oceanography,* 34**,** 68-81.

CHAMI, M., MCKEE, D., LEYMARIE, E. & KHOMENKO, G. 2006a. Influence of the angular shape of the volume-scattering function and multiple scattering on remote sensing reflectance. *Applied Optics,* 45**,** 9210-9220.

CHAMI, M., SHYBANOV, E. B., KHOMENKO, G. A., LEE, M. E. G., MARTYNOV, O. V. & KOROTAEV, G. K. 2006b. Spectral variation of the volume scattering function measured over the full range of scattering angles in a coastal environment. *Applied Optics,* 45**,** 3605-3619.

CHANG, G. & WHITMIRE, A. L. 2009. Effects of bulk particle characteristics on backscattering and optical closure. *Optics Express,* 17**,** 2132-2142.

CHANG, G. BARNARD, A. & ZANEVELD, J. R. V. 2007. Optical closure in a complex coastal environment: particle effects. *Applied Optics,* 46, 7679-7692.

CHANG, G. C., DICKEY, T. D., MOBLEY, C. D., BOSS, E. & PEGAU, W. S. 2003. Toward closure of upwelling radiance in coastal waters. *Applied Optics,* 42**,** 1574-1582.

CHANG, G. C. & DICKEY, T. D. 1999. Partitioning *in situ* total spectral absorption by use of moored spectral absorption-attenuation meters. *Applied Optics,* 38**,** 3876-3887.

CHAVEZ, F. P., BUCK, K. R., BIDIGARE, R. R., KARL, D. M., HEBEL, D., LATASA, M., CAMPBELL, L. & NEWTON, J. 1995. On the chlorophyll-a retention properties of glass-fiber GF/F filters. *Limnology and Oceanography,* 40**,** 428-433.

CIOTTI, A. M., LEWIS, M. R. & CULLEN, J. J. 2002. Assessment of the relationships between dominant cell size in natural phytoplankton communities and the spectral shape of the absorption coefficient. *Limnology and Oceanography,* 47**,** 404-417.

CLEVELAND, J. S. & WEIDEMANN, A. D. 1993. Quantifying absorption by aquatic particles - a multiple-scattering correction for glass-fiber filters. *Limnology and Oceanography,* 38**,** 1321-1327.

COBLE, P. G. 2007. Marine optical biogeochemistry: The chemistry of ocean color. *Chemical Reviews,* 107**,** 402-418.

COBLE, P. G., GREEN, S. A., BLOUGH, N. V. & GAGOSIAN, R. B. 1990. Characterization of dissolved organic-matter in the black-sea by fluorescence spectroscopy. *Nature,* 348**,** 432-435.

COLLINS, J. R. 1925. Change in the infra-red absorption spectrum of water with temperature. *Physical Review,* 26**,** 0771-0779.

D'SA, E. J. & MILLER, R. L. 2003. Bio-optical properties in waters influenced by the Mississippi River during low flow conditions. *Remote Sensing of Environment,* 84**,** 538-549.

D'SA, E. J., STEWARD, R. G., VODACEK, A., BLOUGH, N. V. & PHINNEY, D. 1999. Determining optical absorption of colored dissolved organic matter in seawater with a liquid capillary waveguide. *Limnology and Oceanography,* 44**,** 1142-1148.

DALL'OLMO, G., WESTBERRY, T. K., BEHRENFELD, M. J., BOSS, E. & SLADE, W. H. 2009. Significant contribution of large particles to optical backscattering in the open ocean. *Biogeosciences,* 6**,** 947-967.

DE CARVALHO, L. A. S., BARBOSA, C. C. F., NOVO, E. & RUDORFF, C. D. 2015. Implications of scatter corrections for absorption measurements on optical closure of Amazon floodplain lakes using the Spectral Absorption and Attenuation Meter (AC-S-WETLabs). *Remote Sensing of Environment,* 157**,** 123-137.

FERRARI, G. M. & TASSAN, S. 1999. A method using chemical oxidation to remove light absorption by phytoplankton pigments. *Journal of Phycology,* 35**,** 1090-1098.

FINKEL, Z. V. & IRWIN, A. J. 2001. Light absorption by phytoplankton and the filter amplification correction: cell size and species effects. *Journal of Experimental Marine Biology and Ecology,* 259**,** 51-61.

FOURNIER, G. R. & FORAND, J. L. 1994. Analytical phase function for ocean water. Ocean Optics XII, Jun 13-15 1994 Bergen, Norway. SPIE, 194-201.

FUJII, M., BOSS, E. & CHAI, F. 2007. The value of adding optics to ecosystem models: a case study. *Biogeosciences,* 4**,** 817-835.

GANTT, E. 1977. Recent contributions in phycobiliproteins and phycobilisomes. *Photochemistry and Photobiology,* 26**,** 685-689.

GE, Y. T., GORDON, H. R. & VOSS, K. J. 1993. Simulation of inelastic-scattering contributions to the irradiance field in the ocean - variation in the Fraunhofer line depths. *Applied Optics,* 32**,** 4028-4036.

GLAZER, A. N. 1977. Structure and molecular-organization of photosynthetic accessory pigments of cyanobacteria and red-algae. *Molecular and Cellular Biochemistry,* 18**,** 125-140.

GORDON, H. R. 1992. Diffuse reflectance of the ocean - influence of non-uniform phytoplankton pigment profile. *Applied Optics,* 31**,** 2116-2129.

GORDON, H. R. 1993. Sensitivity of radiative-transfer to small-angle scattering in the ocean - quantitative assessment. *Applied Optics,* 32**,** 7505-7511.

GORDON, H. R. 1999. Contribution of Raman scattering to water-leaving radiance: a reexamination. *Applied Optics,* 38**,** 3166-3174.

GREEN, S. A. & BLOUGH, N. V. 1994. Optical-absorption and fluorescence properties of chromophoric dissolved organic-matter in natural-waters. *Limnology and Oceanography,* 39**,** 1903-1916.

HAKVOORT, J. M. H., BEEKER, A. E. R. & KRIJGSMAN, J. An instrument to measure *in situ* visible light absorption by natural waters. Ocean Optics XII, Jun 13-15 1994 Bergen, Norway. SPIE, 77-88.

HALTRIN, V. I. & KATTAWAR, G. W. 1993. Self-consistent solutions to the equation of transfer with elastic and inelastic-scattering in oceanic optics: 1. model. *Applied Optics,* 32**,** 5356-5367.

HOEPFFNER, N. & SATHYENDRANATH, S. 1992. Biooptical characteristics of coastal water - absorption-spectra of phytoplankton and pigment distribution in the western North-Atlantic. *Limnology and Oceanography,* 37**,** 1660-1679.

HOEPFFNER, N. & SATHYENDRANATH, S. 1993. Determination of the major groups of phytoplankton pigments from the absorption-spectra of total particulate matter. *Journal of Geophysical Research-Oceans,* 98**,** 22789-22803.

HUOT, Y. & BABIN, M. 2010. Overview of Fluorescence Protocols: Theory, Basic Concepts, and Practice. *In:* SUGGETT, D., PRASIL, O. & BOROWITZKA, M. (eds.) *Chlorphyll a Fluorescence in Aquatic Sciences: Methods and Applications.*

JEFFREY, S. W. 1968. Quantitative thin-layer chromatography of chlorophylls and carotenoids from marine algae. *Biochimica Et Biophysica Acta,* 162**,** 271- 285.

JOHNSEN, G. & SAKSHAUG, E. 2007. Biooptical characteristics of PSII and PSI in 33 species (13 pigment groups) of marine phytoplankton, and the relevance for pulse-amplitude-modulated and fast-repetition-rate fluorometry. *Journal of Phycology,* 43**,** 1236-1251.

JOHNSEN, G., SAMSET, O., GRANSKOG, L. & SAKSHAUG, E. 1994. In-vivo absorption characteristics in 10 classes of bloom-forming phytoplankton-taxonomic characteristics and responses to photoadaptation by means of discriminant and HPLC analysis. *Marine Ecology Progress Series,* 105**,** 149-157.

KATTAWAR, G. W. & XU, X. 1992. Filling in of Fraunhofer lines in the Ocean by Raman-scattering. *Applied Optics,* 31**,** 6491-6500.

KIEFER, D. A. 1973. Fluorescence properties of natural phytoplankton populations. *Marine Biology,* 22**,** 263-269.

KIRK, J. T. O. 1983. *Light and Photosynthesis in aquatic ecosystems,* Cambridge Univeristy Press.

KIRK, J. T. O. 1997. Point-source integrating-cavity absorption meter: Theoretical principles and numerical modeling. *Applied Optics,* 36**,** 6123-6128.

KISHINO, M., TAKAHASHI, M., OKAMI, N. & ICHIMURA, S. 1985. Estimation of the spectral absorption-coefficients of phytoplankton in the sea. *Bulletin of Marine Science,* 37**,** 634-642.

KRAUSE, G. H. & WEIS, E. 1991. Chlorophyll fluorescence and photosynthesis - the basics. *Annual Review of Plant Physiology and Plant Molecular Biology,* 42**,** 313-349.

LANGFORD, V. S., MCKINLEY, A. J. & QUICKENDEN, T. I. 2001. Temperature dependence of the visible-near-infrared absorption spectrum of liquid water. *Journal of Physical Chemistry A,* 105**,** 8916-8921.

LEATHERS, R. A., DOWNES, T. V. & DAVIS, C. O. 2000. Analysis of a point-source integrating-cavity absorption meter. *Applied Optics,* 39**,** 6118-6127.

LEE, Z. P., CARDER, K. L. & ARNONE, R. A. 2002. Deriving inherent optical properties from water color: a multiband quasi-analytical algorithm for optically deep waters. *Applied Optics,* 41**,** 5755-5772.

LEFERING, I. 2012. *Stray light and non-linearity characterization of different photo-diode array spectrometers.* B.Sc., Hochschule Bremerhaven.

LEFERING, I., BENGIL, F., TREES, C., RÖTTGERS, R., BOWERS, D., NIMMO-SMITH, A., SCHWARZ, J. & MCKEE, D. 2016. Optical closure in marine waters from *in situ* inherent optical property measurements. *Optics Express,* 24**,** 14036 - 14052.

LEREBOURG, C. J. Y., PILGRIM, D. A., LUDBROOK, G. D. & NEAL, R. 2002. Development of a point source integrating cavity absorption meter. *Journal of Optics a-Pure and Applied Optics,* 4**,** S56-S65.

LEWIS, M. R., CARR, M. E., FELDMAN, G. C., ESAIAS, W. & MCCLAIN, C. 1990. Influence of penetrating solar-radiation on the heat budget of the equatorial pacific-ocean. *Nature,* 347**,** 543-545.

LOHRENZ, S. E. 2000. A novel theoretical approach to correct for pathlength amplification and variable sampling loading in measurements of particulate spectral absorption by the quantitative filter technique. *Journal of Plankton Research,* 22**,** 639-657.

LU, Z. 2006. *Optical absorption by pure water in the blue and ultraviolet.* Ph.D., A&M University Texas.

MARSHALL, B. R. & SMITH, R. C. 1990. Raman-scattering and in-water ocean optical-properties. *Applied Optics,* 29**,** 71-84.

MASKE, H. & HAARDT, H. 1987. Quantitative invivo absorption-spectra of phytoplankton - detrital absorption and comparison with fluorescence excitation-spectra. *Limnology and Oceanography,* 32**,** 620-633.

MCKEE, D., CHAMI, M., BROWN, I., CALZADO, V. S., DOXARAN, D. & CUNNINGHAM, A. 2009. Role of measurement uncertainties in observed variability in the spectral backscattering ratio: a case study in mineral-rich coastal waters. *Applied Optics,* 48**,** 4663-4675.

MCKEE, D. & CUNNINGHAM, A. 2005. Evidence for wavelength dependence of the scattering phase function and its implication for modeling radiance transfer in shelf seas. *Applied Optics,* 44**,** 126-135.

MCKEE, D., PISKOZUB, J., RÖTTGERS, R. & REYNOLDS, R. A. 2013. Evaluation and Improvement of an Iterative Scattering Correction Scheme for *in situ* Absorption and Attenuation Measurements. *Journal of Atmospheric and Oceanic Technology,* 30**,** 1527-1541.

MCKEE, D., RÖTTGERS, R., NEUKERMANS, G., CALZADO, V. S., TREES, C., AMPOLO-RELLA, M., NEIL, C. & CUNNINGHAM, A. 2014. Impact of measurement uncertainties on determination of chlorophyll-specific absorption coefficient for marine phytoplankton. *Journal of Geophysical Research-Oceans,* 119**,** 9013-9025.

MILLER, R. L., BELZ, M., DEL CASTILLO, C. & TRZASKA, R. 2002. Determining CDOM absorption spectra in diverse coastal environments using a multiple pathlength, liquid core waveguide system. *Continental Shelf Research,* 22**,** 1301-1310.

MIMURO, M. & AKIMOTO, S. 2003. Carotenoids of light harvesting systems: Energy transfer processes from fucoxanthinand peridinin to chlorophyll. *In:* LARKUM, A. W., DOUGLAS, S. E. & RAVEN, A. (eds.) *Photosynthesis in Algae.* Dordrecht, The Netherlands: KluwerAcademic Publisher.

MITCHELL, B. G. Algorithms for determining the absorption-coefficient of aquatic particulates using the quantitative filter technique (QFT). Ocean Optics X, Apr 16-18 1990 Orlando, Florida. SPIE, 137-148.

MITCHELL, B. G., KAHRU, M., WIELAND, J. & STRAMSKA, M. 2003. Determination of spectral absorption coefficients of particles, dissolved material and phytoplankton for discrete water samples. *In:* MUELLER, J. L., FARGION, G. S. & MCCLAIN, C. R. (eds.) *Ocean Optics Protocols for Satellite Ocean Color Sensor Validation, Volume IV - Rev.4.*

MITCHELL, B. G. & KIEFER, D. A. 1984. Determination of absorption and fluorescence excitation spectra for phytoplankton. *In:* HOLM-HANSEN, O., BOLIS, L. &

GILLES, R. (eds.) *Marine phytoplankton and productivity*. New York: Springer-Verlag, Berlin.

MITCHELL, B. G. & KIEFER, D. A. 1988. Chlorophyll-alpha specific absorption and fluorescence excitation-spectra for light-limited phytoplankton. *Deep-Sea Research Part a-Oceanographic Research Papers,* 35**,** 639-663.

MITCHELL, C., CUNNINGHAM, A. & MCKEE, D. 2014. Remote sensing of shelf sea optical properties: Evaluation of a quasi-analytical approach for the Irish Sea. *Remote Sensing of Environment,* 143**,** 142-153.

MOBLEY, C. D. 1994. *Light and Water. Radiative Transfer in Natural Waters,* San Diego, CA, Academic Press.

MOBLEY, C. D., SUNDMAN, L. K. & BOSS, E. 2002. Phase function effects on oceanic light fields. *Applied Optics,* 41**,** 1035-1050.

MOORE, C., TWARDOWSKI, M. S. & ZANEVELD, J. R. V. The ECO VSF - A multi-angle scattering sensor for determination of the volume scattering function in the backward direction. Ocean Optics XV, Oct 16-20 2000 Monaco. SPIE, 330 - 337.

MOORE, L. R., GOERICKE, R. & CHISHOLM, S. W. 1995. Comparative physiology of synechococcus and prochlorococcus - influence of light and temperature on growth, pigments, fluorescence and absorptive properties. *Marine Ecology Progress Series,* 116**,** 259-275.

MOREL, A. & PRIEUR, L. 1977. Analysis of variation in ocean color. *Limnology and Oceanography,* 22**,** 709-722.

MUELLER, J. L. 2003. In-water radiometric profile measurements and data analysis protocol in radiometric measurements and data analysis protocols. *In:* MUELLER, J. L., FARGION, G. S. & MCCLAIN, C. R. (eds.) *Ocean Optics Protocols for Satellite Ocean Color Sensor Validation, Volume III - Rev. 4.*

NEELEY, A. R., FREEMAN, S. A. & HARRIS, L. A. 2015. Multi-method approach to quantify uncertainties in the measurements of light absorption by particles. *Optics Express,* 23**,** 31043-31058.

NELSON, N. B. & SIEGEL, D. A. 2013. The Global Distribution and Dynamics of Chromophoric Dissolved Organic Matter. *Annual Review of Marine Science,* 5**,** 447-476.

NELSON, N. B., SIEGEL, D. A., CARLSON, C. A. & SWAN, C. M. 2010. Tracing global biogeochemical cycles and meridional overturning circulation using chromophoric dissolved organic matter. *Geophysical Research Letters,* 37.

NELSON, N. B., SIEGEL, D. A. & MICHAELS, A. F. 1998. Seasonal dynamics of colored dissolved material in the Sargasso Sea. *Deep-Sea Research Part I-Oceanographic Research Papers,* 45**,** 931-957.

NEORI, A., VERNET, M., HOLMHANSEN, O. & HAXO, F. T. 1986. Relationship between action spectra for chlorophyll-a fluorescence and photosynthetic O-2 evolution in algae. *Journal of Plankton Research,* 8**,** 537-548.

NEUKERMANS, G., REYNOLDS, R. A. & STRAMSKI, D. 2014. Contrasting inherent optical properties and particle characteristics between an under-ice phytoplankton bloom and open water in the Chukchi Sea. *Deep-Sea Research Part II -Topical Studies in Oceanography,* 105**,** 59-73.

PEGAU, W. S., ZANEVELD, J. R. V. & MUELLER, J.. 2003. Volume Absorption Coefficients: Instruments, Characterization, Field Measurements and Data Analysis Protocols. *In:* MUELLER, J. L., FARGION, G. S. & MCCLAIN, C. R. (eds.) *Ocean Optics Protocols for Satellite Ocean Color Sensor Validation, Volume IV - Rev.4.*

PEGAU, W. S., GRAY, D. & ZANEVELD, J. R. V. 1997. Absorption and attenuation of visible and near-infrared light in water: dependence on temperature and salinity. *Applied Optics,* 36**,** 6035-6046.

PEGAU, W. S. & ZANEVELD, J. R. V. 1993. Temperature-dependent absorption of water in the red and near-infrared portions of the spectrum. *Limnology and Oceanography,* 38**,** 188-192.

PEPERZAK, L., TIMMERMANS, K. R., WERNAND, M. R., OOSTERHUIS, S. & VAN DER WOERD, H. J. 2011. A mesocosm tool to optically study phytoplankton dynamics. *Limnology and Oceanography-Methods,* 9**,** 232-244.

PEPERZAK, L., VAN DER WOERD, H. J. & TIMMERMANS, K. R. 2015. Disparities between *in situ* and optically derived carbon biomass and growth rates of the prymnesiophyte Phaeocystis globosa. *Biogeosciences,* 12**,** 1659-1670.

POPE, R. M. & FRY, E. S. 1997. Absorption spectrum (380-700 nm) of pure water. II. Integrating cavity measurements. *Applied Optics,* 36**,** 8710-8723.

POPE, R. M., WEIDEMANN, A. D. & FRY, E. S. 2000. Integrating Cavity Absorption Meter measurements of dissolved substances and suspended particles in ocean water. *Dynamics of Atmospheres and Oceans,* 31**,** 307-320.

PREISENDORFER, R. W. 1961. Application of Radiative Transfer theory to Light Measurements in the Sea. *Union of Geodetic Geophysical Institute Monograph, Vol. 10.*

PRIEUR, L. & SATHYENDRANATH, S. 1981. An optical classification of coastal and oceanic waters based on the specific spectral absorption curves of phytoplankton pigments, dissolved organic-matter and other particulate materials. *Limnology and Oceanography,* 26**,** 671-689.

RAICHLIN, Y., MILLO, A. & KATZIR, A. 2004. Investigations of the structure of water using mid-IR fiberoptic evanescent wave spectroscopy. *Physical Review Letters,* 93.

ROESLER, C. S. 1998. Theoretical and experimental approaches to improve the accuracy of particulate absorption coefficients derived from the quantitative filter technique. *Limnology and Oceanography,* 43**,** 1649-1660.

RUBAN, A. V., PASCAL, A. A., ROBERT, B. & HORTON, P. 2001. Configuration and dynamics of xanthophylls in light-harvesting antennae of higher plants - Spectroscopic analysis of isolated light-harvesting complex of photosystem II and thylakoid membranes. *Journal of Biological Chemistry,* 276**,** 24862-24870.

RÖTTGERS, R. & DOERFFER, R. 2007. Measurements of optical absorption by chromophoric dissolved organic matter using a point-source integrating-cavity absorption meter. *Limnology and Oceanography-Methods,* 5**,** 126-135.

RÖTTGERS, R., DOERFFER, R., FISCHER, J., HOLLSTEIN, A., LAVENDER, S. & MCKEE, D. 2009. Water Radiance - Literature Review Report. GKSS.

RÖTTGERS, R., DOXARAN, D. & PUPOUY, C. 2016. Quantitative filter technique measurements of spectral light absorption by aquatic particles using a portable integrating cavity absorption meter (QFT-ICAM). *Optics Express,* 24**,** A1-A20.

RÖTTGERS, R., DUPOUY, C., TAYLOR, B. B., BRACHER, A. & WOZNIAK, S. B. 2014a. Mass-specific light absorption coefficients of natural aquatic particles in the near-infrared spectral region. *Limnology and Oceanography,* 59**,** 1449-1460.

RÖTTGERS, R. & GEHNKE, S. 2012. Measurement of light absorption by aquatic particles: improvement of the quantitative filter technique by use of an integrating sphere approach. *Applied Optics,* 51**,** 1336-1351.

RÖTTGERS, R., HAESE, C. & DOERFFER, R. 2007. Determination of the particulate absorption of microalgae using a point-source integrating-cavity absorption meter: verification with a photometric technique, improvements for pigment bleaching, and correction for chlorophyll fluorescence. *Limnology and Oceanography-Methods,* 5**,** 1-12.

RÖTTGERS, R., MCKEE, D. & UTSCHIG, C. 2014b. Temperature and salinity correction coefficients for light absorption by water in the visible to infrared spectral region. *Optics Express,* 22**,** 25093-25108.

RÖTTGERS, R., MCKEE, D. & WOZNIAK, S. B. 2013. Evaluation of scatter corrections for ac-9 absorption measurements in coastal waters. *Methods in Oceanography,* 7**,** 21-39.

RÖTTGERS, R., SCHÖNEFELD, W., KIPP, P. R. & DOERFFER, R. 2005. Practical test of a point-source integrating cavity absorption meter: the performance of different collector assemblies. *Applied Optics,* 44**,** 5549-5560.

SANJUAN CALZADO, V., MCKEE, D., TREES, C. & ZIBORDI, G. Multi and single cast radiometric processing and merging in the Ligurian Sea. Optics of Natural Waters, Sep 6-10 2011 Saint Petersburg.

SATHYENDRANATH, S., PRIEUR, L. & MOREL, A. 1989. A three-component model of ocean color and its application to remote-sensing of phytoplankton pigments in coastal waters. *International Journal of Remote Sensing,* 10**,** 1373-1394.

SCHROEDER, M., BARTH, H. & REUTER, R. 2003. Effect of inelastic scattering on underwater daylight in the ocean: model evaluation, validation, and first results. *Applied Optics,* 42**,** 4244-4260.

SEGTNAN, V. H., SASIC, S., ISAKSSON, T. & OZAKI, Y. 2001. Studies on the structure of water using two-dimensional near-infrared correlation spectroscopy and principal component analysis. *Analytical Chemistry,* 73**,** 3153-3161.

SEPPALA, J., YLOSTALO, P., KAITALA, S., HALLFORS, S., RAATEOJA, M. & MAUNULA, P. 2007. Ship-of-opportunity based phycocyanin fluorescence monitoring of the filamentous cyanobacteria bloom dynamics in the Baltic Sea. *Estuarine Coastal and Shelf Science,* 73**,** 489-500.

SIEGEL, D. A. & MICHAELS, A. F. 1996. Quantification of non-algal light attenuation in the Sargasso Sea: Implications for biogeochemistry and remote sensing. *Deep-Sea Research Part II -Topical Studies in Oceanography,* 43**,** 321-345.

SIMIS, S. G. H., HUOT, Y., BABIN, M., SEPPALA, J. & METSAMAA, L. 2012. Optimization of variable fluorescence measurements of phytoplankton communities with cyanobacteria. *Photosynthesis Research,* 112**,** 13-30.

SMITH, R. C. & BAKER, K. S. 1981. Optical-properties of the clearest natural-waters (200-800 nm). *Applied Optics,* 20**,** 177-184.

SMITH, R. C., PREZELIN, B. B., BIDIGARE, R. R. & BAKER, K. S. 1989. Biooptical modeling of photosynthetic production in coastal waters. *Limnology and Oceanography,* 34**,** 1524-1544.

SOKOLETSKY, L. G. & SHEN, F. 2014. Optical closure for remote-sensing reflectance based on accurate radiative transfer approximations: the case of the Changjiang (Yangtze) River Estuary and its adjacent coastal area, China. *International Journal of Remote Sensing,* 35**,** 4193-4224.

SOSIK, H. M. 1999. Storage of marine particulate samples for light-absorption measurements. *Limnology and Oceanography,* 44**,** 1139-1141.

SPITZER, D. & WERNAND, M. R. 1981. Insitu measurements of absorption-spectra in the sea. *Deep-Sea Research Part a-Oceanographic Research Papers,* 28**,** 165-174.

STAUBER, J. L. & JEFFREY, S. W. 1988. Photosynthetic pigments in 51 species of marine diatoms. *Journal of Phycology,* 24**,** 158-172.

STRAMSKA, M., STRAMSKI, D., HAPTER, R., KACZMAREK, S. & STON, J. 2003. Bio-optical relationships and ocean color algorithms for the north polar region of the Atlantic. *Journal of Geophysical Research-Oceans,* 108.

STRAMSKI, D. 1990. Artifacts in measuring absorption-spectra of phytoplankton collected on a filter. *Limnology and Oceanography,* 35**,** 1804-1809.

STRAMSKI, D., BABIN, M. & WOZNIAK, S. B. 2007. Variations in the optical properties of terrigenous mineral-rich particulate matter suspended in seawater. *Limnology and Oceanography,* 52**,** 2418-2433.

STRAMSKI, D., REYNOLDS, R. A., KACZMAREK, S., UITZ, J. & ZHENG, G. M. 2015. Correction of pathlength amplification in the filter-pad technique for measurements of particulate absorption coefficient in the visible spectral region. *Applied Optics,* 54**,** 6763-6782.

STRAMSKI, D., REYNOLDS, R. A., KAHRU, M. & MITCHELL, B. G. 1999. Estimation of particulate organic carbon in the ocean from satellite remote sensing. *Science,* 285**,** 239-242.

SUGIHARA, S., KISHINO, M. & OKAMI, N. 1984. Contribution of Raman scattering to upward irradiance in the sea. *J. Oceanogr. Soc,* 40**,** 397-404.

SULLIVAN, J. M., TWARDOWSKI, M. S., ZANEVELD, J. R. V., MOORE, C. M., BARNARD, A. H., DONAGHAY, P. L. & RHOADES, B. 2006. Hyperspectral temperature and salt dependencies of absorption by water and heavy water in the 400-750 nm spectral range. *Applied Optics,* 45**,** 5294-5309.

TASSAN, S. & FERRARI, G. M. 1995. An alternative approach to absorption measurements of aquatic particles retained on filters. *Limnology and Oceanography,* 40**,** 1358-1368.

TASSAN, S. & FERRARI, G. M. 1998. Measurement of light absorption by aquatic particles retained on filters: determination of the optical pathlength amplification by the 'transmittance-reflectance' method. *Journal of Plankton Research,* 20**,** 1699-1709.

TASSAN, S. & FERRARI, G. M. 2003. Variability of light absorption by aquatic particles in the near-infrared spectral region. *Applied Optics,* 42**,** 4802-4810.

TRABJERG, I. & HOJERSLEV, N. K. 1996. Temperature influence on light absorption by fresh water and seawater in the visible and near-infrared spectrum. *Applied Optics,* 35**,** 2653-2658.

TRÜPER , H. G. & YENTSCH, C. S. 1967. Use of glass fiber filters for rapid preparation of *in vivo* absorption spectra of photosynthetic bacteria. *Journal of Bacteriology,* 94**,** 1255-1256.

TWARDOWSKI, M. S., SULLIVAN, J. M., DONAGHAY, P. L. & ZANEVELD, J. R. V. 1999. Microscale quantification of the absorption by dissolved and particulate material in coastal waters with an ac-9. *Journal of Atmospheric and Oceanic Technology,* 16**,** 691-707.

TZORTZIOU, M., HERMAN, J. R., GALLEGOS, C. L., NEALE, P. J., SUBRAMANIAM, A., HARDING, L. W. & AHMAD, Z. 2006. Bio-optics of the Chesapeake Bay from measurements and radiative transfer closure. *Estuarine Coastal and Shelf Science,* 68**,** 348-362.

VOSS, K., GORDON, H., LEWIS, M., MCLEAN, S., TWARDOWSKI, M., JOHNSON, C., YARBROUGH, M., FLORA, S., FEINHOLZ, M. & TREES, C. 2008. Radiometry and uncertainties from SORTIE (Spectral Ocean Radiance Transfer Investigation and Experiment). NASA Carbon Cycle & Ecosystem Joint Science Workshop.

VOSS, K. J. 1989. Use of radiance distribution to measure the optical-absorption coefficient in the ocean. *Limnology and Oceanography,* 34**,** 1614-1622.

WANG, L. 2008. *Measuring optical absorption coefficients of pure water in the UV using the integrating cavity absorption meter.* Ph.D., A&M University Texas.

WETLABS INC. 2008. Absorption and attenuation meter, ac-9, User's Guide, Revision Q.

WETLABS INC. 2010. Scattering meter, ECO BB-9, User's Guide, Revision K.

WETLABS INC. 2011. ac Meter, Protocol Document, Revision Q.

WETLABS INC. 2013. ac Meter, Product Drawing.

WORLD PRECISION INSTRUMENTS INC. 2004. 2000 Series Liquid Waveguide Capillary Cell, Instruction Manual.

WOZNIAK, B. & DERA, J. 2007. *Light absorption in Sea Water*, Springer.

WOZNIAK, S. B. & STRAMSKI, D. 2004. Modeling the optical properties of mineral particles suspended in seawater and their influence on ocean reflectance and chlorophyll estimation from remote sensing algorithms. *Applied Optics,* 43**,** 3489-3503.

YENTSCH, C. S. 1957. Non-extractive method for the quantitative estimation of chlorophyll in algal cultures. *Nature,* 179**,** 1302-1304.

YENTSCH, C. S. 1962. Measurement of visible light absorption by particulate matter in the ocean. *Limnology and Oceanography,* 7**,** 207-217.

YENTSCH, C. S. & YENTSCH, C. M. 1979. Fluorescence spectral signatures - characterization of phytoplankton populations by the use of excitation and emission-spectra. *Journal of Marine Research,* 37**,** 471-483.

ZANEVELD, R. V., KITCHEN, J. C. & MOORE, C. The scattering error correction of reflecting-tube absorption meters. Ocean Optics XII, Jun 13-15 1994 Bergen, Norway. SPIE, 44-55.

ZHAI, P. W., HU, Y. X., WINKER, D. M., FRANZ, B. A. & BOSS, E. 2015. Contribution of Raman scattering to polarized radiation field in ocean waters. *Optics Express,* 23**,** 23582-23596.

ZHANG, X. D. & GRAY, D. J. 2015. Backscattering by very small particles in coastal waters. *Journal of Geophysical Research-Oceans,* 120**,** 6914-6926.

ZHANG, X. D. & HU, L. B. 2009. Scattering by pure seawater at high salinity. *Optics Express,* 17**,** 12685-12691.

ZHANG, X. D. & HU, L. B. 2010. Effects of temperature and salinity on light scattering by water. Conference on Ocean Sensing and Monitoring II, Apr 05-06 2010 Orlando, Florida.

ZHANG, X. D., HU, L. B. & HE, M. X. 2009a. Scattering by pure seawater: Effect of salinity. *Optics Express,* 17**,** 5698-5710.

ZHANG, X. D., HU, L. B., TWARDOWSKI, M. S. & SULLIVAN, J. M. 2009b. Scattering by solutions of major sea salts. *Optics Express,* 17**,** 19580-19585.

ZHENG, G. M. & STRAMSKI, D. 2013. A model based on stacked-constraints approach for partitioning the light absorption coefficient of seawater into phytoplankton and non-phytoplankton components. *Journal of Geophysical Research-Oceans,* 118**,** 2155-2174.

ZIBORDI, G., D'ALIMONTE, D. & BERTHON, J. F. 2004. An evaluation of depth resolution requirements for optical profiling in coastal waters. *Journal of Atmospheric and Oceanic Technology,* 21**,** 1059-1073.